ABSTRACT

Title of Dissertation:	DESIGN OF HYBRID POLYMER-INORGANIC NANOASSEMBLIES FOR BIOMEDICAL APPLICATIONS
	Kuikun Yang, Doctor of Philosophy, 2018
Dissertation directed by:	Professor Zhihong Nie, Department of Chemistry and Biochemistry

Assembly of inorganic nanoparticles (NPs) can give rise to novel collective properties due to the coupling between adjacent subunits, which are not accessible from individual nanoparticles. Among them, hybrid polymer-inorganic nanoassemblies (HPINs) are particularly attractive by combining the complementary strengths of inorganic NPs and polymers. This dissertation describes the design of HPINs with elaborately tailored physicochemical properties and the applications of HPINs in tumor diagnosis and therapy.

First, we introduced the design principles and representative morphologies of HPINs. Size, shape, surface charge and coatings are crucial properties to be considered before the design of HPINs. Among various types of HPINs, we focused on the hybrid vesicles assembled from polymer-tethered inorganic NPs due to their synergistic properties that surpass their constituent components. We also summarized recent

advances in the development of HPINs as attractive platforms for cancer imaging and therapy.

Second, we developed an enzyme-free signal amplification technique, based on gold vesicles encapsulated with Pd−Ir NPs as peroxidase mimics, for colorimetric assay of disease biomarkers with significantly enhanced sensitivity.

Third, we introduced a universal approach to attach amphiphilic block copolymers onto oleic acid or/and oleylamine capped NPs to trigger their assembly. Various NPs including Fe_3O_4, Cu_9S_5, MnO and upconversion NPs were assembled into hollow vesicles with novel physicochemical properties for a variety of biomedical applications.

Finally, we described the fabrication of nanosized magneto-vesicles comprising tunable layers of densely packed superparamagnetic iron oxide nanoparticles (SPIONs) in membranes via cooperative assembly of polymer-tethered SPIONs and free poly(styrene)-*b*-poly(acrylic acid). Due to the high packing density of SPIONs, the magneto-vesicles showed enhanced signal in magnetic resonance imaging as well as improved efficiency in magnetic-guided drug delivery both *in vitro* and *in vivo*.

DESIGN OF HYBRID POLYMER-INORGANIC NANOASSEMBLIES FOR BIOMEDICAL APPLICATIONS

By

Kuikun Yang

Dissertation submitted to the Faculty of the Graduate School of the
University of Maryland, College Park, in partial fulfillment
of the requirements for the degree of
Doctor of Philosophy
2018

Advisory Committee:
Professor Zhihong Nie, Chair
Professor Laixi Wang
Professor Lyle Isaacs
Professor Sang Bok Lee
Professor Christopher Jewell, Dean's representative

Dedication

To my parents, Zhaolong Yang and Meiqin Ma

Acknowledgements

It would not be possible to write this doctoral thesis without the help and support from the kind people around me.

I would like to thank my advisor, Zhihong Nie, for his continuous research support and patient guidance. During my graduate study, he is very considerate and always helps me to solve the research problems in patience. I have learnt a lot from Prof. Nie, including but not limited to critical thinking, research design, paper writing and effective presentation. Without his tremendous help and guidance I would never be able to get here. He has set an example of excellence as a researcher, mentor, instructor and scientist. I feel extremely lucky to study under his supervision.

I would also like to thank Prof. Xiaoyuan Chen for helping me on biomedical researches. His guidance and support led me into the field of tumor theranostics which I plan to study further in my future researches.

I also wish to thank all of the members in Prof. Nie's group for their kind help on my research and daily life. I would like to thank Dr. Maria Teresa Perez for organizing the lab activities. I would like to thank Dr. Chenglin Yi for his help on polymer synthesis. I would like to thank Dr. Yijing Liu for his help on *in vivo* experiments. I hope to thank Dr. Yang Yang, Dr. Shaoyi Zhang, Marcus Carter and Hongyu Guo for their help with my writing.

I would like to thank my committee members, Prof. Christopher Jewell, Prof. Laixi Wang, Prof. Sang Bok Lee and Prof. Lyle Isaacs for their time in my defense and valuable comments on my dissertation.

Last but not least, I would like to thank my parents for their unconditional love and substantial support during these years. I am so grateful to my parents Zhaolong Yang and Meiqin Ma for bringing me up to this wonderful would and providing me the best education. Without their wholehearted support and unfailing understanding, the completion of this thesis would have been impossible.

Table of Contents

List of Figures

List of Abbreviations

AMF ..... alternating magnetic field

ATRP..... atom transfer radical polymerization

BCPs.....block copolymers

Dox..... doxorubicin

GNPs..... gold nanoparticles

GNRs.....gold nanorods

GVs.....gold vesicles

HPINs.....hybrid polymer-inorganic nanoassemblies

IONPs..... iron oxide nanoparticles

LbL..... layer-by-layer

MAIE..... multiphoton absorption induced emission

MRI ..... magnetic resonance imaging

MVs ..... magneto-vesicles

NIR .....near infrared

NPs.....nanoparticles

NRs .....nanorods

PA ..... photoacoustic

PAA ..... poly(acrylic acid)

PEG ..... poly(ethyl glycol)

PEO-*b*-PS ..... poly(ethyl oxide)-block-polystyrene

PT ..... photothermal

PTT..... photothermal therapy

QDs ..... quantum dots

RAFT ..... addition-fragmentation transfer polymerization

RES ..... reticuloendothelial system

ROS ..... reactive oxygen species

SPIONs ..... superparamagnetic iron oxide NPs

THF .....tetrahydrofuran

Chapter 1: Introduction

Part of this chapter is adapted from the manuscript "Shaoyi Zhang[†], Kuikun Yang[†], Jie He, Wan-Kyu Oh and Zhihong Nie[#], Polymer/inorganic Nanohybrids for Cancer Imaging and Therapy" to be submitted to Nano Today. ([†] Equal contribution)

Self-assembly refers to the process by which small building blocks such as molecules and colloid particles spontaneously organize into larger or ordered structures without external intervention.[1] Molecular self-assembly is extraordinarily common in nature and in daily life and it plays numerous important roles in the formation of various complex structures. For example, membranes of living cells originate from the self-assembly of phospholipids. Viruses are assembled from protein and nucleic acid. Soap bubbles are self-assemblies of small molecule surfactants. Materials scientists have aspired to replicate assembly principles found in nature to design and fabricate artificial materials with hierarchical structures and tailored properties for a variety of applications. Compared with top-down methods such as photo-lithography, self-assembly is a simple and low-cost bottom-up approach to create complex nano- or micro-sized functional materials from pre-existing building blocks. With the rapid development in colloidal particle synthesis, researchers have become increasingly interested in using colloidal nanoparticles (NPs) as building blocks to fabricate functional assemblies with controlled structures. However, it remains challenging to organize colloidal NPs into desired assemblies as conventional molecular building blocks. It is, therefore, essential to develop novel strategies for the assembly of inorganic NPs in order to meet the rising demand for advanced materials.

1.1 Molecular self-assembly

Understanding the principles of molecular self-assembly is the foundation for studying and designing more complex assembly systems of colloidal NPs. A wide range of molecules such as, lipids, surfactants, dendritic molecules and block copolymers (BCPs), can be used to form supramolecular nanostructures at different conditions. These molecules often consist of one or more hydrophobic tails and a hydrophilic head group to make them amphiphilic. The amphiphilicity enables their self-assembly into various nanostructures, such as spherical micelles (spheres), cylindrical micelles (cylinders), bicontinuous structures, lamellae and vesicles in selective solvents. The morphology of assemblies is primarily determined by the packing parameter, $p = v/a_o l_c$, where v is the volume of the hydrophobic segment, a_o is the cross-sectional area of the head group, and l_c is the length of the hydrophobic segment. Spherical micelles are generally formed when p is less than 1/3; cylinders are assembled when $1/3 < p < 1/2$; flexible lamellae or vesicles when $1/2 < p < 1$; and planar lamellae when $p = 1$. If p is larger than 1, inverted structures could be observed.[2]

1.1.1 Self-assembly of amphiphilic lipids

Amphiphilic lipids are the most important building blocks for self-assembly. They are generally composed of a hydrophilic head and a hydrophobic tail region (Figure 1.1). The amphiphilic structure of lipids induces the aggregation of these molecules into larger structures with well-organized position and orientation in water. In addition, the structural diversity of lipids with different polarities, lengths and charged groups allows the formation of a library of assembly structures in water such as micelles,

lamellar bilayers and vesicles (liposomes), which have already found applications in different fields including biosensing, bioimaging and drug delivery.[3,4]

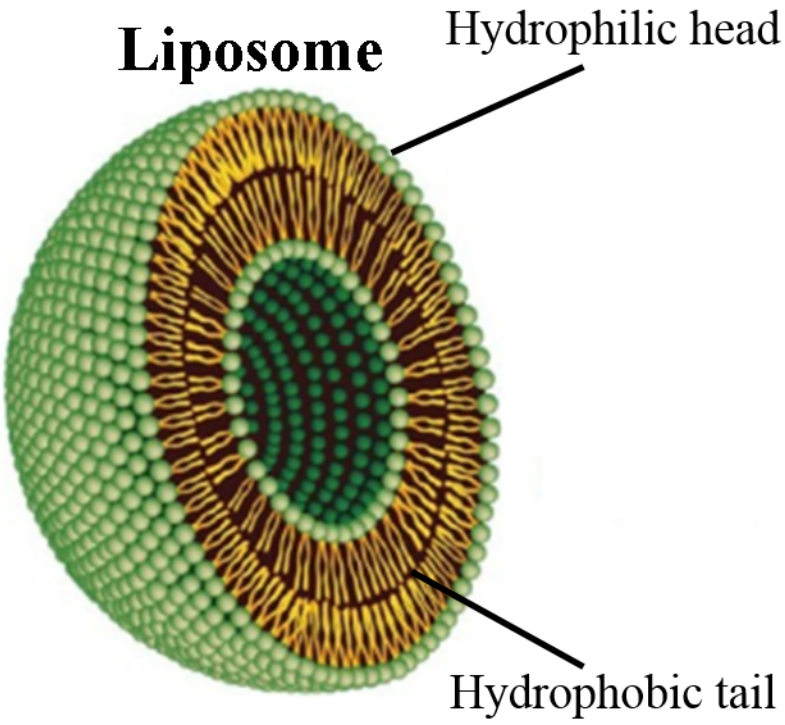

Figure 1.1. Schematic illustration of self-assembling of amphiphilic lipids into liposomes. Reproduced from Ref. [4] with permission of Dovepress.

1.1.2 Self-assembly of amphiphilic block copolymers (BCPs)

Amphiphilic BCPs, in which hydrophobic and hydrophilic polymer blocks are covalently bound to each other, are another commonly used building blocks for self-assembly. The self-assembly of amphiphilic BCPs in selective solvents generates assemblies with a variety of morphologies including spheres, cylinders, lamellae, bicontinuous gyroids and vesicular micelles (Figure 1.2). Current advances in polymer

synthesis have allowed the rationale design of BCPs with high uniformity, purity and significant chemical and structural diversity. Compared with small-molecule assemblies, polymer assemblies exhibit higher stability and durability due to their mechanical properties, as well as higher complexity due to the flexibility and deformability of BCP chains. The assembly structures of BCPs have found broad applications in such as microelectronics, photoelectric materials, catalysts, bioimaging and drug delivery.[5,6]

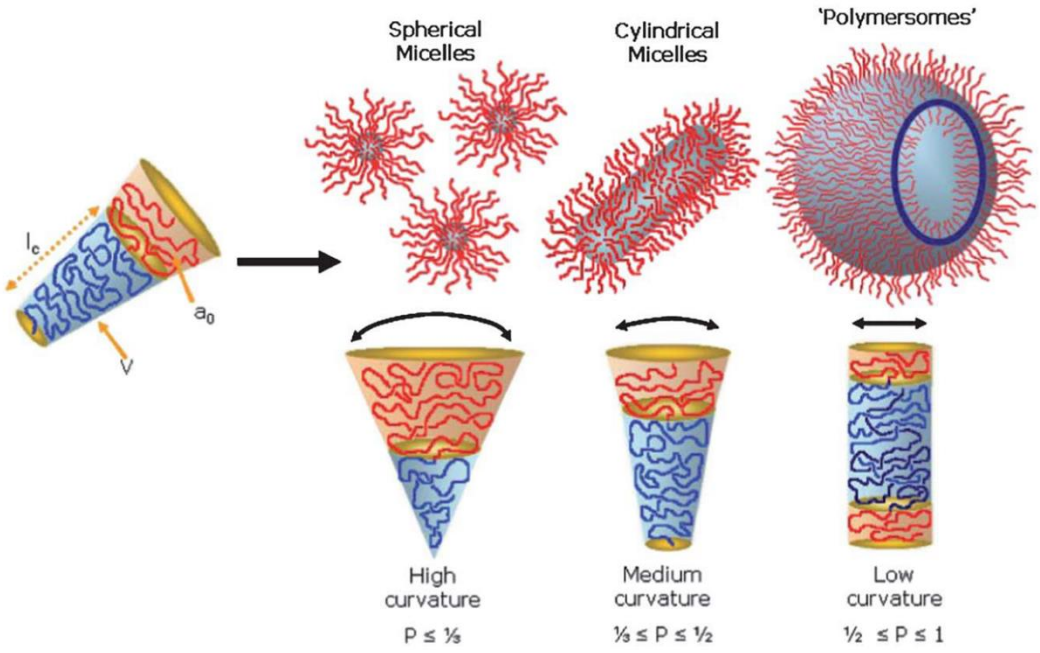

Figure 1.2. Schematic illustration of self-assembling of amphiphilic BCPs into spherical micelles, cylindrical micelles, and vesicles according to their packing parameter. Reproduced from Ref. [6] with permission of Wiley-VCH Verlag GmbH & Co. KGaA.

1.2 Hybrid polymer-inorganic nanoassemblies (HPINs)

Although assemblies of amphiphilic molecules have received considerable attention in both academic researches and practical applications, the rapidly rising demand for new materials drives the design of nanostructures with increasing complexity and new functionalities. Hybrid nanoscale materials comprising two or more components in one system may exhibit advanced or new properties that surpass their constituent components, due to the combination or synergistic effect of the subunits. Among them, hybrid polymer-inorganic nanoassemblies (HPINs) are particularly attractive as they naturally combine the complementary strengths of inorganic NPs (e.g., intrinsic optical and magnetic properties, etc.) and polymers (e.g., biocompatibility, biodegradability, chemical stability, tunable responsiveness to external stimuli such as, heat, light, and sound wave, etc.). As a result, HPINs have emerged as attractive platforms for tumor management by offering early diagnosis, high resolution imaging, real time therapeutic monitoring, selective tumor targeting and efficient tumor growth inhibition.[7]

1.2.1 Design principles of HPINs for biomedical applications

To achieve optimal theranostic performance, it is crucial to deliver sufficient amount of HPINs to the right time and location. The *in vitro* and *in vivo* fate of HPINs is governed by their physicochemical properties such as size, shape, charge and surface coating (Figure 1.3).

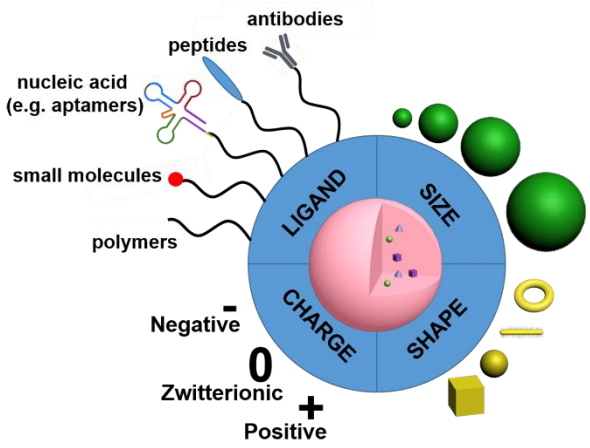

Figure 1.3. Physicochemical properties that determine *in vivo* performance of HPINs.

(i) Size. The effects of size have been studied extensively with spherically shaped particles for their biomedical applications. The ideal size of NPs for *in vivo* applications falls in the range between 5 and 200 nm.[8-10] Particles smaller than 5 nm are rapidly cleared from the circulation through extravasation or renal clearance, while particles larger than 200 nm tend to be trapped by Kupffer cells in reticuloendothelial systems (RES). On the other hand, tumor vessels tend to be more permeable than normal vessels, which allows passive accumulation of NPs in tumor tissues (enhanced permeability and retention effect). However, small particles (<5nm) can be readily secreted from tumor tissues even after they accumulate around tumor. Particles that are larger than 200 nm are believed not able to penetrate through the leaky vessels.

(ii) Shape. Although the shape of particles is known to play an important role in their *in vivo* fate, the exact effects of NP shape on biological actions are still under debate, due to the variation in the sample standards and intrinsic complexity of the biological system. For example, the shape of particles is considered to directly influence their cellular uptake. When the size of NPs exceeds 100 nm, rods show the

highest cellular uptake, followed by spheres, cylinders, and cubes.[11] On the contrary, in studies with sub-100 nm NPs, spheres have higher cellular internalization than rods. Additionally, in this size range, increasing the aspect ratio of nanorods (NRs) decreases the cell uptake of NPs.

(iii) Charge. Surface charge of NPs also determines their cellular uptake, biodistribution and interaction with other biological environments. Generally, positively charged NPs are considered to be more easily internalized than neutral and negatively charged NPs. This can be attributed to the electrostatic attraction between negatively charged membrane and positively charged NPs which favors their adhesion onto the cell membrane, leading to enhanced uptake compared with neutral and negatively charged NPs.[12] This process, in fact, can be complicated when serum or other biological species are presented due to the quick absorption and formation of protein corona on NP surface. As the surface charge determines corona composition, the interaction between NPs and cells also varies from study to study. In this regard, cellular uptake of the NPs by phagocytes or target cells should be tested prior to *in vivo* administration of HPINs.

(iv) Surface coating. The surface coating can influence biological performance of NPs such as circulation time, biodistribution and cellular uptake. PEGylation of NPs has been widely used to prolong their *in vivo* circulation time by the stealthing effect. Functional ligands that can specifically target certain cellular populations can also be introduced to HPINs by surface modification. Various ligands such as antibodies, aptamers, peptides and small molecules have been introduced onto the surface of HPINs to enhance their accumulation in desired tissues.[13] Beyond selective active

targeting, responsiveness to specific microenvironment can be imparted to HPINs by utilizing appropriate surface coating. For instance, HPINs could be programed to respond to light, heat, pH or enzymes for various biomedical applications.

1.2.2 Representative morphologies of HPINs

Depending on the spatial distribution of inorganic NPs and polymers, there are six distinct representative morphologies of HPINs that can be classified into three categories: 1) solid NPs consisting of polymeric shell loaded with one or more inorganic NPs as core(s) (I, II); 2) polymeric micelles loaded with one or more inorganic NPs (III); and 3) NP-loaded hollow vesicles: polymer vesicles internally loaded with inorganic NPs (IV), polymer vesicles embedded with inorganic NPs in the hydrophobic membrane (V), and hybrid vesicles assembled from polymer tethered inorganic NPs (VI) (Figure 1.4).

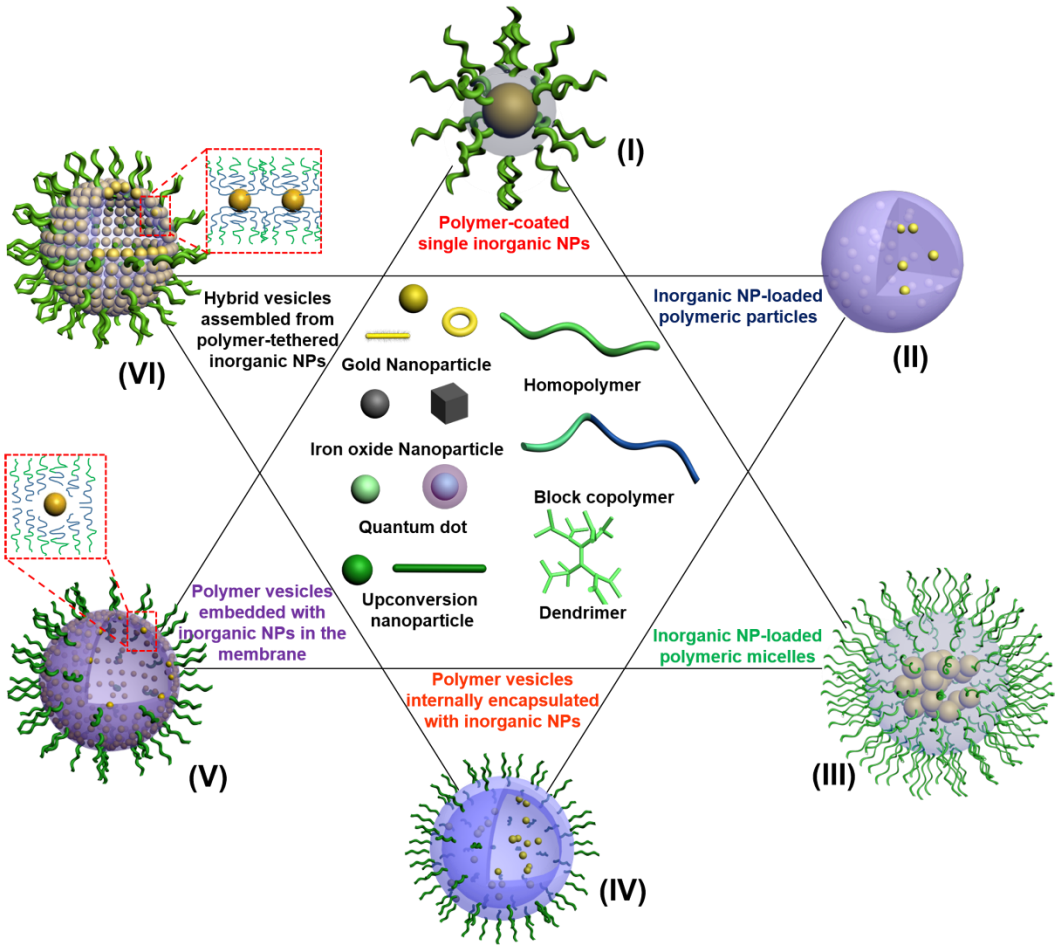

Figure 1.4. Representative morphologies of polymer/inorganic nanohybrids that are summarized into six main categories: polymer-coated single inorganic NPs (I), inorganic NP-loaded polymer particles (II), inorganic NP-loaded polymeric micelles (III), polymer vesicles internally encapsulated with inorganic NPs (IV), polymer vesicles embedded with inorganic NPs in the membrane (V), and hybrid vesicles assembled from polymer-tethered inorganic NPs (VI). The major difference between (V) and (VI) is the density and ordering of NPs in the vesicular membranes.

Polymer-coated inorganic NPs

The simplest HPINs are polymer-coated inorganic NPs, in which inorganic NPs are enclosed in polymer shells. Constructing a layer of polymers on the surface of inorganic NPs has multiple benefits for biomedical applications. The polymer coatings can improve the stable dispersion and biocompatibility of inorganic NPs in intracellular microenvironments and prevent possible dissociation of toxic inorganic ions. Efficient targeting and internalization of NPs can be achieved by designing polymers with functional groups for specific targeting capability or for the further conjugation of targeting moieties. Most importantly, the polymers can be also used to absorb or conjugate cargos within the nanostructures through noncovalent interactions or covalent bonds.

As an efficient method to coat polymeric thin films with desired properties on various NP surfaces, electrostatic layer-by-layer (LbL) self-assembly has been developed and widely used to design functional nanocarriers for bioimaging and drug delivery.[14] The coating of inorganic NPs with polymer layers relies on the alternate adsorbing of oppositely charged polyelectrolytes on the surface of inorganic NPs.[15] The thickness of each layer can be adjusted by tuning the ionic strength of the polyelectrolyte solution. A thicker layer can be obtained by using a solution of higher ionic strength, due to the induced loops or tails formation of polymers. A solution of low ionic strength facilitates the flat conformation of polymers on NP surfaces to form a thinner layer.

In LbL assembly, the positive charge of polymers is usually contributed by the ionization of amino- and imino-containing groups, such as poly(allylamine) (PAL), poly(ethylenimine) (PEI), etc., while the negative charge of polyanions often comes

from pendant sulfonate groups or carbonate groups, such as poly(styrenesulfonate), poly(acrylic acid) (PAA), etc. The composition of the polymer layers is not limited to two components, as long as the polymers possess opposite charges of appropriate strength. With the appropriate choice of polymers and functional ligands, the resulting customized solid polymer coated single NPs can meet various requirements from surface chemistry, biocompatibility, controlled permeability, loading of therapeutic agents to optical or magnetic properties.[16]

Different from noncovalent coating of polymer layers via LbL technique, polymeric shells can be grown directly on the surface of NPs to form HPINs. Initially, inorganic NPs are attached with initiators or chain transfer agents, followed by the growth of polymer chains extending out from the NPs surface. For effective attachment, the initiator or chain transfer agent should bear functional groups with strong affinity to the surface of NPs, such as thiol for noble metal NPs (e.g., Ag, Au) and quantum dots (QDs), silane for silica NPs, carboxylate or phosphonate for iron oxide NPs (IONPs), etc.[17] Various surface initiated polymerization techniques have been used to grow polymer chains, such as nitroxide-mediated polymerization (NMP), reversible addition-fragmentation transfer polymerization (RAFT), and atom transfer radical polymerization (ATRP).[18,19]

Coating polymer shells on the surface of inorganic NPs presents as a facile and efficient way to prepare HPINs from diverse combinations of polymers and inorganic NPs. Polymer-coated inorganic NPs show advantages on flexible size tuning of NPs in the 10-100 nm size range which benefits their accessibility to and within disseminated tumors for enhanced efficiency in bioimaging and drug delivery. However, it remains

challenging to improve the loading capacity and control the intrinsic properties of individual polymer-coated inorganic NP. Thus, more elaborately designed HPINs are required for enhanced efficacy in biomedical applications.

Inorganic NP-loaded polymer particles

Another type of HPINs is inorganic NP-loaded solid polymeric particles in which multiple inorganic NPs are homogeneously or spatially arranged in a polymer matrix. There are two major approaches for encapsulating NPs in polymer matrix: (i) polymerization in the presence of inorganic NPs and (ii) emulsification of polymers in a solution of inorganic NPs. The former one usually involves solution-phase polymerization (e.g., emulsion polymerization) in the presence of inorganic NPs. In a typical emulsion polymerization-based synthesis, inorganic NPs are first treated with hydrophobic coupling agents, in order to tailor the suitable affinity between the monomer and the surface of NPs, followed by the initiation of polymerization to achieve NP-loaded polymer particles. HPINs are also fabricated by emulsification of a mixture of polymers and NPs followed by solvent removal. In this approach, a solution of mixed polymer and inorganic NPs are emulsified into nano- or micro-sized droplets in an immiscible solvent (e.g., water). The solvent in droplets is subsequently removed to generate final products by evaporation, salting out, emulsification diffusion, dialysis, or supercritical fluid technology.[20-22] Emulsifying agents such as ordinary phospholipids, PEGylated lipids and poly vinyl alcohol (PVA) are usually used to stabilize the emulsion droplets and prevent the coalescence of droplets during the process.[23-25] The size of nanohybrids made by this method can be tuned in the range of

tens to hundreds of nm (mostly below 200 nm), which is dependent on a series of parameters, including the temperature, chemical composition and concentration of surfactant.[26] Using this method, a variety of inorganic NPs with different sizes, shapes, and compositions (e.g., iron oxide, QDs, noble metal NPs) have been loaded in polymeric matrix of homopolymers or BCPs.[7,22] To achieve the homogenous dispersion of inorganic NPs in the matrix, inorganic NPs are usually treated by hydrophobic coupling agents so that the surface ligand of inorganic NPs should be compatible with (one block of) the polymer matrix. Since all NPs are embedded within the polymeric particle, the biodistribution and pharmacokinetic properties of the inorganic NP-loaded polymeric particles could be well controlled by polymer ligand on the particle surface. However, it is challenging to control the specific encapsulation efficiency of NPs per polymer particle which significantly restricts their clinical translation.

Inorganic NP-loaded Polymeric micelles

The micellization of polymers provides an efficient strategy for the encapsulation of inorganic NPs to form HPINs. Conventional polymeric micelles are obtained from the self-assembly of amphiphilic BCPs.[27] The hydrophilic shell maintains the aqueous stability of polymeric micelles and protects the hydrophobic domains which act as a reservoir for loading inorganic NPs and therapeutic cargos. There are a variety of ways to encapsulate inorganic NPs into polymeric micelles, including co-precipitation, emulsification, heating-cooling and film rehydration.[28]

As the distribution of inorganic NPs in the polymeric micelles plays an important role in determining their properties, principles are developed to tune the spatial distribution of NPs basing on the interactions between NPs and polymer microstructures. By tuning the surface properties of NPs with capping agents, the interactions between ligand-polymer and ligand-surface could be well tailored to form various assembly structures. For instance, modifying NPs with polymer brushes favors the interaction of NPs with polymer host and reduces the attraction between NPs, which benefits for the uniform dispersion of NPs in polymer micelles. Similarly, parameters like the size of inorganic NPs (compared with the radius of gyration of the host polymer), the relative concentration of NPs and polymers, and the choice of solvent could also significantly influence the spatial distribution of NPs and the number of NPs encapsulated within each micelle.[29-32] Park et al obtained three distinct structures by tuning the hydrophiphilic/hydrophobic balance of BCPs for assembly: (i) magneto-polymersomes with densely packed magnetic NPs in the membrane; (ii) magneto-core-shell assemblies with NPs radially arranged at the interface of the core and shell region; (iii) magneto-micelles with homogeneously incorporated NPs (Figure 1.5). The varied structure of assemblies was also realized by using different solvent conditions, which determines the interactions of NP/solvent and NP/polymer.[32]

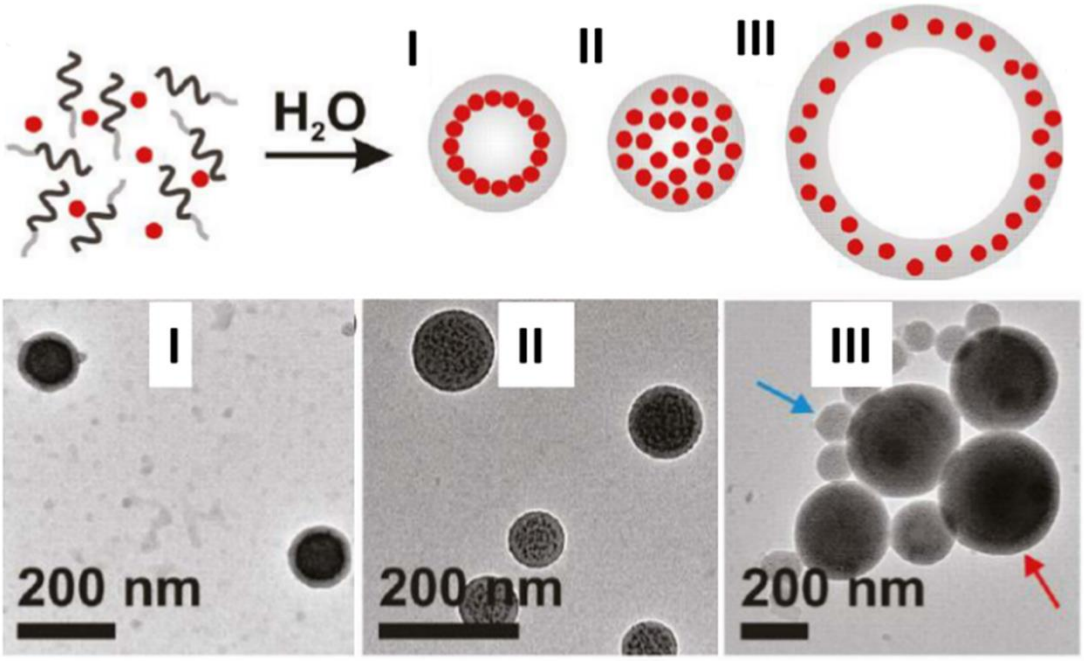

Figure 1.5. Fabrication of polymeric micelles loaded with inorganic NPs. Self-assembly of NPs and BCPs into (I) magneto-core shell assemblies, (II) magneto-micelles, and (III) magneto-polymersomes. Reproduced with permission from Ref. [30]. Copyright 2011 American Chemical Society.

Inorganic NPs can also be loaded into polymeric micelles by *in situ* synthesis. This approach usually involves loading precursors into the micelle assembled from BCPs, followed by the reaction of the precursor to form NPs in the center.[33] In this case, the size of NPs can be tuned by the length of the polymer brush. Moreover, *in situ* synthesis using polymeric micelles of conventional linear BCPs as nanoreactors can provide NPs with well controlled polymer layers. However, the stability of micellar aggregates is sensitive to temperature and solvent condition, which limits the types of inorganic NPs that can be synthesized.

Polymer vesicles internally encapsulated with inorganic NPs

Depending on the inherent curvature of the amphiphilic BCPs, their self-assembly in selective solvents also renders the formation of polymersomes, in which the hydrophobic block forms a vesicular shell, leaving the hydrophilic brush extends to both the interior and exterior sides of the vesicles. Typical strategies for assembly include emulsion-solvent evaporation, nanoprecipitation, dialysis, microfluidic fabrication, and thin film rehydration.[1] In a thin film rehydration process, a film of BCPs is formed on the substrate and water is added to rehydrate the film with or without the assistance of sonication or heating. The polymer layers swell and form protrusions that detach from the surface of substrate and enclose to form water-soluble vesicles. A broad size distribution of vesicles is commonly observed due to the nonequilibrium nature of the vesicle formation process.[34] When hydrophilic inorganic NPs are dispersed in water for film rehydration, this procedure generates polymeric vesicles with inorganic NPs trapped in the inner aqueous cavity. A relatively large amount of inorganic NPs could be loaded in an individual vesicle when concentrated NPs solution is used for rehydration.[35]

Polymer vesicles embedded with inorganic NPs in the membrane

Hydrophobic inorganic NPs can be encapsulated within the membranes of polymer vesicles to produce vesicular nanohybrids. The incorporation of NPs in the vesicular membrane originates from the co-assembly of a mixture of inorganic NPs and amphiphilic BCPs. IONPs and noble metal NPs with hydrophobic capping agents are the most common candidates for producing hybrid polymeric vesicles.[36] The NPs are

embedded in the membrane via hydrophobic interactions, rather than covalent bonding with polymers. Generally, the thickness of polymersome membrane can be adjusted in the range of 10-50 nm, which largely defines the size of inorganic NPs that can be integrated in the membrane (usually less than 10 nm).[37] When inorganic NPs with sizes comparable to the membrane thickness are used, the NPs would rather distribute at the periphery of the bilayer to decorate the hydrophobic/hydrophilic interface and form bilayer structures. As a result, oligo- or multiamellar vesicles or even onion-type vesicles are formed with NP bridging the adjacent bilayers.[38]

The relationship between the NP-incorporation and the vesicle morphology has been broadly investigated. Park et al showed that the increase in size of inorganic NPs led to the increase in the yield of vesicles and the decrease in the vesicular size, as well as more ordered organization of NPs in the membrane. This NP size dependent morphology transition can be attributed to the entropic cost arises from incorporating large NPs into the polymer domain.[39] By carefully tuning the NP size, inorganic NP-bearing polymer vesicles could be fabricated with tailored size and properties for a variety of biomedical applications.

Hybrid vesicles assembled from polymer-tethered inorganic NPs

As mentioned above, the size and content of inorganic NPs that can be loaded in the hydrophobic domain of polymeric vesicles are often limited due to the possible NP integration-induced instability and morphological transition of vesicles. Unlike those structures, hybrid vesicles assembled from polymer-tethered inorganic NPs contain densely-packed NPs chemically grafted with polymer brushes in the membrane, which

significantly enhances the stability and loading of inorganic components. Inspired by the assembly of amphiphilic molecules, colloidal amphiphiles was constructed for the fabrication of hybrid vesicles comprising closely packed inorganic NPs in the membrane of vesicles. Amphiphilic BCPs or a mixture of hydrophilic and hydrophobic homopolymer brushes are grafted on the surface of NPs to achieve amphiphilic nature, followed by self-assembly of the colloidal amphiphiles into vesicular structures (Figure 1.6a).

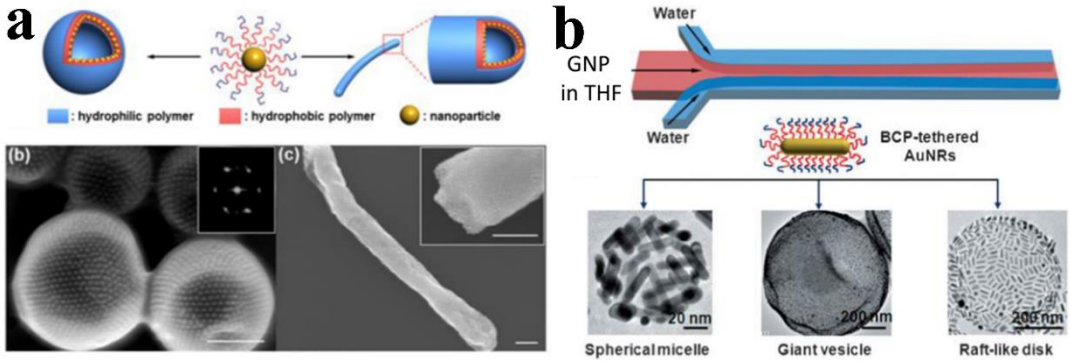

Figure 1.6. Assembly of polymer-tethered inorganic NPs into hybrid vesicles. (a) Scheme and SEM images of spherical and tubular vesicles assembled from PEO-*b*-PS tethered GNPs. Reproduced with permission from Ref. 42. Copyright 2012 American Chemical Society. (b) Scheme and SEM images of different structures via microfluidic self-assembly of amphiphilic PEO-*b*-PS tethered Au NRs in microfluidic flow-focusing devices. Reproduced with permission from Ref. 41. Copyright 2013 WILEY-VCH Verlag GmbH & Co. KGaA, Weinheim.

Assembly of amphiphilic NPs in selective solvents can be realized by dialysis, film rehydration and microfluidic strategies.[40,41] Take the microfluidic approach as an

example, a solution of polymer tethered inorganic NPs (in THF) together with two water streams are introduced in a microfluidic flow-focusing device (Figure 1.6b). The streams of two miscible fluids form a laminar flow and the diffusion of molecules along the transverse direction gradually changes the solvent quality for the hydrophobic blocks of BCP tethered on NPs, thus driving the association of colloidal amphiphiles to form different structures.[42,43] The formation of assemblies with different morphologies (e.g., micelles, sheets, and giant vesicles) is determined by the hydrodynamics of flow and the characteristics (e.g., hydrophobic/hydrophilic balance) of colloidal building blocks. In recent years, this method is applicable for assembling NPs with a broad range of sizes (5-60 nm) and shapes (spherical NPs, NRs, nanoflowers, nanochains) into hybrid vesicles.[44-47] Various factors (e.g., size and shape of inorganic NPs, the length of polymers, and the grafting density of polymers) are found to influence the vesicle formation and the morphology of vesicles significantly. For instance, the assembly of poly(ethyl oxide)-block-polystyrene (PEO-*b*-PS) grafted gold nanoparticles (GNPs) was found to depend on the hydrophobic/hydrophilic balance for various structures (e.g., hybrid vesicles, clusters, unimolecular micelles). The balance is determined by the ratio between the length of hydrophobic block in BCPs (R) and the relative size of GNPs (d).[44] Spherical vesicles are formed when $R/d<0.5$. When R/d is close to 0.5, formation of one dimensional tubular structures is preferred.

The co-assembly of polymer-tethered inorganic NPs with free polymer and/or other types of NPs leads to NPs-bearing vesicles with various morphologies and chemical compositions.[48-50] For example, the co-assembly of GNPs tethered with PEO-

b-PS and free PEO-*b*-PS in selective solvent generated a series of hybrid vesicles with various shapes, including patchy vesicles with islands of NP membranes, shaped Janus vesicles with spherical/hemispherical/disk-like shapes, and heterogeneous vesicles with uniform distribution of NPs in the membranes.[48] The formation of various patterned vesicles was attributed to the complex interaction between the dimension mismatch of building blocks, the entanglement of BCP chains, and the mobility of the NP amphiphiles. The co-assembly of GNPs tethered with PEO-b-PS, free PS-b-PAA and hydrophobic IONPs in selective solvents led to the formation of Janus vesicles where GNPs and IONPs are distributed in two distinct halves. Tuning the size and mass fraction of NPs could produce spherical and hemispherical Janus vesicles with distinct transverse relaxivity value and absorption in near infrared (NIR) range for further biomedical applications.[50]

1.2.3 Applications of HPINs in biological imaging

The incorporation of inorganic NPs into hybrid assemblies facilitates the imaging capability of the platform, as a result of their intrinsic properties and the coupling between adjacent subunits. The imaging capability provides HPINs with at least the following important functions. First, imaging of HPINs offers spatial and temporal information regarding the tumor angiogenesis and tumor microenvironment both in the primary tumor and in metastatic sites. This information is crucial for early diagnosis of tumor and/or for the selection and optimization of therapeutic strategies. Second, the imaging capability of HPINs can be used to characterize the biodistribution of NPs and quantify the dose and duration of NPs delivered to the target sites. This will help to

guarantee the accumulation of sufficient NPs at tumor tissues. Third, imaging of HPINs makes possible to monitor the delivery dynamics of therapeutic agents, and predict the possible outcomes of therapy. Based on this information, therapy can be potentially optimized and personalized to achieve maximum antitumor efficiency. (Figure 1.7)

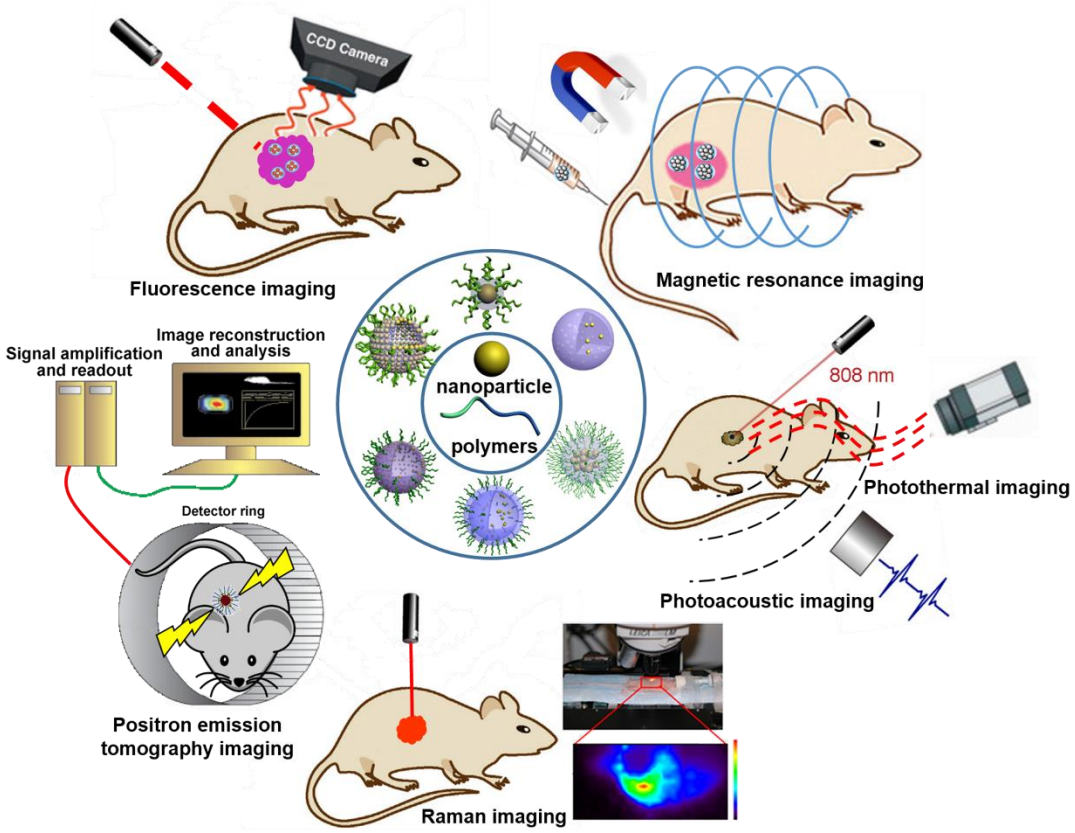

Figure 1.7. Schematic illustration of the applications of HPINs in cancer imaging and diagnostics.

Fluorescence imaging

As one of the most commonly used fluorescence imaging agents, quantum dots could provide direct information of their surroundings. QDs are semiconducting NPs

with size on the same order of or smaller than their exciton Bohr radius where the energy is quantized. The absorption of a photon with energy higher than the semiconductor band gap energy generates excitons and results in a broadband absorption spectrum of QDs for photons with short wavelengths. The subsequent recombination of an exciton leads to the emission of a photon in a narrow energy band. Due to the quantum confinement effect, QDs exhibit luminescence emission that is strongly dependent on their size. The emission of QDs shows unique features such as super-brightness, relatively narrow emission band (v.s. organic fluorophore), tunable emission wavelength and low photobleaching, which makes them appealing for non-destructive bioimaging.[51-53]

Despite their extraordinary optical properties, QDs are prone to surface oxidation and hence release toxic heavy metal ions to surrounding biological medium. Recent *in vitro* and *in vivo* studies showed that QDs are cytotoxic to various cell lines and tissues.[54] The cytotoxicity of QDs is dependent on the dose and duration of exposure, as well as their physicochemical properties. Therefore, long-term safety concerns severely limit the *in vitro* and particularly *in vivo* applications of QDs. Insufficient fluorescence is another defect of conventional QDs-based bioimaging. Due to the surface defects in the crystal structure acting as temporary "traps" to prevent their radiative recombination, QDs may experience intermittent fluorescence and/or reduced overall quantum yield (QE) which is denoted as the ratio of emitted to absorbed photons. Coating the surface of QDs with an organic or inorganic shell can improve the fluorescence QE and stability against photobleaching, prevent the release of metal ions, as well as enhance the stability of QDs during the circulation in animal body.[55,56]

However, the optical properties of QDs are highly sensitive to their local surroundings (i.e., the property of protective shell). The quantum efficiency of QDs is often drastically reduced when they are coated with inorganic layers such as silica.[57] In order to solve these issues, assemblies of QDs in BCPs were prepared and demonstrated to improve the stability, while preserving the optical property of QDs.[58,59] Nie et al. studied the application of CdSe-loaded polymer micelles for *in vivo* cancer targeting and imaging.[55] Single tri-n-octylphosphine oxide (TOPO)-covered hydrophobic CdSe QDs were encapsulated in polymer micelles of ABC triblock copolymer of poly(butylacrylate)-b-poly(ethylacrylate)-b-poly(methacrylic acid) (PBA-b-PEA-b-PMAA) and stabilized by poly(ethylene glycol) (PEG) corona. The tight wrapping of QDs by the hydrophobic segments of BCPs prevents the fluorescence loss of QDs. Meanwhile, the optical properties of QDs were preserved in a broad range of pH (1 to 14) and salt conditions (0.01 to 1 M), which significantly facilitates their applications in biological imaging and diagnosis.

Multiphoton absorption induced emission (MAIE) imaging

Multiphoton absorption induced emission (MAIE) imaging is an attractive optical imaging techniques for biological applications.[60-63] The absorption of multiple photons occurs when the sum energy of a few photons (normally two or three low energy photons) matches the band gap and hence excites electrons at the ground state. As the probability of simultaneous absorption of two or more photons is extremely low, the MAIE only takes place at a high photon density of flux (e.g. the focus plane of pulsed laser). The MAIE shows several advantages over conventional single-photon emission

technique, including: i) deeper penetration of living tissues and organs because of the excitation light in NIR range; ii) easier acquisition of 3D imaging with high spatial resolution; and iii) lower background noise. Metal and semiconducting NPs have been reported for their significantly higher multiphoton absorption cross-section (i.e. high brightness) than that of organic fluorophores, making them more promising agents for deep *in vivo* multiphoton imaging.[63]

Ensembles of noble metal NPs show promising collective optical properties arising from the coupling between neighboring NPs. The plasmonic-enhanced multiphoton absorption results in a more intense MAIE signal than individual NPs, thus facilitating their application in bioimaging.[64,65] Recently, Nie et al. demonstrated the utilization of HPINs for enhanced MAIE imaging of 4T1 cancer cells with the excitation of a NIR laser.[66] It was found that *in vitro* MAIE signal gradually increased with increases in the aggregation number of NPs within cluster or vesicular assemblies of 20 nm GNPs, which significantly improved the imaging contrast after the assembly of GNPs.

Dark Field Imaging

Dark field imaging collects the light scattered by the sample to create an image in which the sample appears bright against a dark background. Metallic NPs can be used as non-bleaching labels for dark field imaging of biological samples because they can effectively scatter light over a narrow band of wavelengths. The scattering cross-section of metallic NPs drops rapidly with a decrease in size and so does the imaging signal. Although large metallic NPs provide strong imaging signal, there are concerns about their long-term safety in terms of toxicity and clearance before their clinical

translation.[8] Assembling small metallic NPs into nanoscale hybrids that can be degraded to original small building blocks offers a strategy to potentially address this problem.[67] As an example, Tam et al. assembled sub-5 nm GNPs into biodegradable polymer/NP clusters with controlled diameter in the range of ~50-100 nm with strong NIR absorption for imaging and therapeutic applications.[68] The assemblies exhibited dark-field reflectance and hyperspectral imaging in a murine macrophage cell line. After remaining in the cells for 1 week, the large nanoclusters (~100 nm in diameter) dissociated into original GNPs (smaller than 5 nm in diameter), thus demonstrating the efficient body clearance of the NPs.

Photothermal (PT) and Photoacoustic (PA) Imaging

PT imaging is based on temperature–induced variation in the refractive index of tissues and organs to transform invisible NPs into visible thermal field image upon laser irradiation. In contrast to PT imaging, PA imaging detects and transforms the propagation of wideband ultrasound waves induced by PT heating in tissue into an image. In PA imaging, the tissue absorbs light irradiated by a laser beam and partially or completely converts the absorbed photon energy to heat. This non-invasive imaging technique seamlessly combines the merits of both ultrasonic technique and optical imaging. Compared with conventional optical imaging, this technique shows stronger optical absorption contrast of biological tissue, higher ultrasonic spatial resolution, and deeper penetration in biological tissues beyond the optical diffusion limit.

To achieve enhanced and precise visualization, exogenous contrast agents are usually required for PT and PA imaging. A wide range of inorganic NPs (e.g., CuS

NPs)[69-71] and polymeric NPs (e.g, polypyrrole NPs)[72,73] have been utilized as PT conversion agents. Among the different PT conversion agents, gold nanostructures are particularly attractive due to their absorption of light, high thermal conductivity, and superior stability and biocompatibility.[74,75] However, the absorption peak of spherical GNPs is in the wavelength range of 520-580 nm, which is not ideal for *in vivo* PT and/or PA imaging. Compared with visible light, NIR laser exhibits a minimal absorption of light by tissues and the resultant deeper tissue penetration. The assembly of GNPs can tune the plasmon coupling between NPs and shift the absorption peak of a collection of GNPs to the NIR region, which could significantly enhance the biological performance of NPs than their individuals without strong NIR absorption.

Among various assembly structures of GNPs, vesicles have attracted considerable interest due to their effective loading of both hydrophilic and hydrophobic agents for tumor imaging and therapy. To modulate the optical property and therapeutics loading of the HPINs, Nie et al. designed vesicular assemblies with a single layer of GNPs tethered with amphiphilic PS-*b*-PEO in the membrane.[44,66,76,77] The strong plasmonic coupling between closely-packed GNPs within membranes led to a strong absorption of the assemblies in the NIR window. The hybrid vesicles were demonstrated for effective *in vivo* multi-modality imaging (i.e., PT imaging, PA imaging, and fluorescence imaging) of subcutaneous MDA-MB-435 breast cancer xenografts in athymic nude mice.[76] The organization of GNPs in vesicular membranes was found to be crucial to their performance in PT and/or PA imaging, as a result of the optimization of light absorption in the NIR window. More recently, Nie's group further reported the stepwise assembly of GNPs into linear NP "strings" that subsequently folded up to

form vesicular containers (Figure 1.8).[47] The linear ordering of NPs within vesicular membranes resulted in a strong absorption of assemblies at NIR wavelengths (ca.760 nm). This subtle change in the organization of NPs led to a nearly ten-fold enhancement in the PA signal for *in vivo* imaging, compared with vesicles with regular spacing of GNPs.

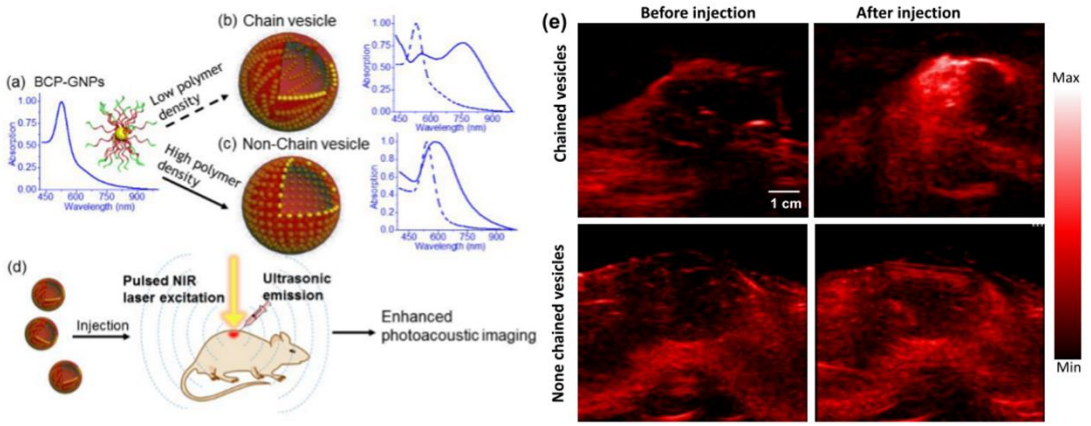

Figure 1.8. (a-c) Schematic illustration of the self-assembly of BCP tethered GNPs (BCP-GNPs) into chain vesicles and non-chain vesicles and (d) the enhanced PA imaging with chain vesicles. *In vivo* 2D PA imaging of mouse tissue before and after the injection of chain vesicles (a, b) and none chain vesicle (c, d). Two types of vesicles containing the same amount of gold materials (50 μg) were subcutaneously injected into the flank of nude mice and was irradiated with a pulsed NIR laser (780 nm, 60 mW/cm^2) for equal amount of time. Reproduced with permission from Ref. 45. Copyright 2013 WILEY-VCH Verlag GmbH & Co. KGaA, Weinheim.

Magnetic Resonance Imaging (MRI)

Magnetic Resonance imaging (MRI) is a non-invasive imaging technique with a spatial resolution on the order of tens of micrometers. This technique has been widely used in cancer imaging and diagnosis, as it offers anatomic and functional information, such as tumor volume and angiogenetic status. Typically, hydrogen protons will align and process around an applied magnetic field, when a transverse radio-frequency pulse is applied, these protons are disturbed from the magnetic field and return to their original state, which is referred as relaxation phenomenon. The MRI is generated by monitoring two independent processes, i.e. longitudinal relaxation (T_1-recovery) and transverse relaxation (T_2-decay). The proton density, chemical and physical nature of the tissues result in the image contrast. Contrast agents are usually required to provide high resolution and accuracy for effective cancer diagnosis and assessment in MRI. The shortening of both the longitudinal and transverse relaxation of surrounding protons can be achieved by magnetic NPs (MNPs). The T_1 shortening process is based on the close interaction between protons and T_1 agents while the T_2 shortening arises from the large susceptibility difference between MNPs and surrounding medium. MNPs such as superparamagnetic iron oxide NPs (SPIONs) are generally used as negative T_2 contrast agents in MRI as a result of more significant T_2 effect.[78,79] MNPs synthesized by high temperature decomposition of organic precursors often show superior magnetic properties for efficient MRI. However, the hydrophobic nature of their surfaces makes them not suitable for direct use in biological conditions. Polymers are frequently assembled with MNPs to increase the stability and biocompatibility of the MNPs.[80] In addition, compared with single NP-based contrast agent systems, polymer/MNP assemblies can be more efficient in shortening T_2 relaxation rate in MRI,

largely due to more uniform magnetization and numerous MNP/water molecule interactions.[81,82]

The clustering of MNPs and accessibility of water molecules to MNPs are crucial factors in determining the relaxivity rates of MRI contrast agents. Therefore, the size, morphology and NP arrangement of polymer/MNP assemblies can significantly influence the magnetic relaxation of the assemblies and hence their performance in MRI. The enhancement in the relaxivity of HPINs assemblies has been observed in MNP-loaded micelles and solid NPs, as well as polymersomes embedded (or loaded) with MNPs in the membranes (or within the hollow cavity).[83,84] However, a lack of specific control of the MNPs density in the assemblies hinders further applications of the HPINs in biological imaging.

1.2.4 Applications of HPINs in tumor therapy

The utilization of hybrid assemblies for cancer therapy originates from at least the following merits of the platform. First, the superior imaging capability enabled by inorganic NPs offers an attractive way to monitor microenvironment changes associated with cancer at molecular level.[85] Second, the integration of imaging and therapy in one system (so-called "theranostics") allows one to simultaneously track the delivery of both nanocarriers and therapeutic agents to tumor sites, to determine the angiogenic activity of tumor, as well as to evaluate the outcome of cancer therapies. Third, the activation of payload release from hybrid assemblies by light or magnetic field can reduce non-specificity and improve the efficacy of systematic drug delivery.[36] Last but not least, the combination therapy (e.g., photothermal-chemotherapy,

photodynamic-chemotherapy, etc.) can further maximize the therapeutic outcomes by reducing drug resistance or promoting possible synergetic effect between multiple therapies (Figure 1.9).[86]

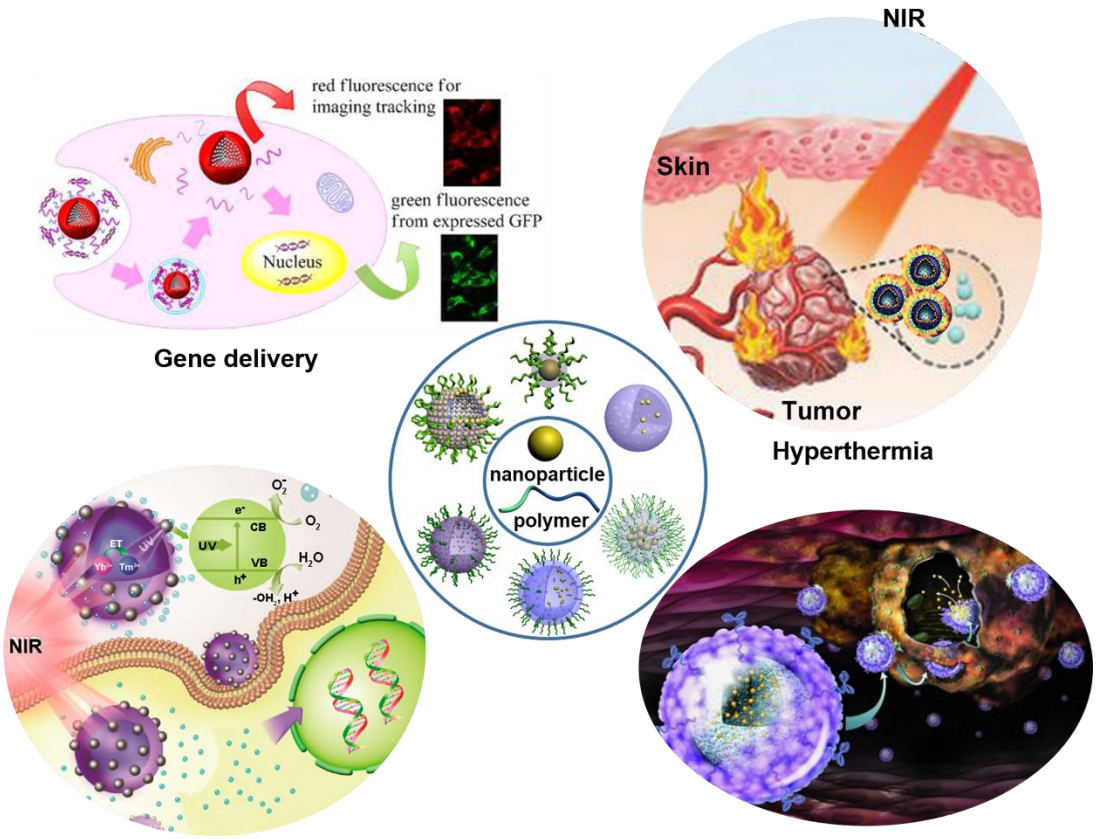

Figure 1.9. Schematic illustration of the applications of HPINs in cancer therapy via different modalities

Hypothermia Therapy

Hyperthermia therapy utilizes localized heating to damage tumor cells or make tumor cells more sensitive to therapeutic agents, while minimizing damage on healthy tissues. Tumor tissues are more sensitive to hyperthermia than healthy tissues, as a

result of sparse vascular structures of tumor. While conventional methods (e.g., ultrasound and microwaves) can efficiently deliver heat to tumors, a major concern for these approaches is the exposure of a large volume of normal tissues to hyperthermic temperature. HPINs can provide the specificity required for thermal ablation of tumors. In this case, heating can be confined in the vicinity of hybrid assemblies which are preferentially accumulated in the tumor tissue, if the volume of treatment and exposure time of light are carefully controlled. Various magnetic, metallic and semiconductor NPs capable of generating heat have been integrated in the hybrid assemblies as hyperthermia agents for this purpose.[87,88] The unique imaging capability of these NPs can guide the tumor-targeted delivery of the NPs, thus further improving the likelihood of successful treatment of cancer.

MNPs can generate heat efficiently when exposed to an external alternating magnetic field (AMF).[89] The efficiency of heating is proportional to the magnetization of NPs, as well as the amplitude and frequency of applied AMF. Therefore, MNPs have been widely explored as efficient hyperthermia agents in HPINs for simultaneous cancer imaging and therapy.[90-93] Magnetic hyperthermia is capable of eliminating tumors that are resided deeply inside the biological system, as the penetrating depth of magnetic field is not limited. This technique is non-invasive and does not cause any adverse effect on biological tissues. Moreover, the magnetization and movement of MNPs under magnetic field can be used to locally concentrate NPs at a desired site of tissues to achieve specific targeting.

The assembly of many MNPs within polymers can effectively maintain or increase magnetic moment of the assemblies for hyperthermia therapy and magnetic

manipulation. Hyeon et al. reported the assembly of multiple ferrimagnetic Fe_3O_4 nanocubes in polymeric shell of chitosan oligosaccharide for magnetically modulated cancer hyperthermia.[94] In this work, L-3,4-dihydroxyphenylalanine (DOPA)-conjugated chitosan was used to assemble 30-nm-sized nanocubes through the strong interaction between catechol groups of DOPA and iron oxide surfaces. The hybrid assemblies locally accumulated in human lung carcinoma A549 cells under a magnetic field, thanks to the increased magnetic moments of multiple nanocubes. The assembly platform exhibited significantly higher hyperthermal efficiency than commercial superparamagnetic Feridex NPs, demonstrating the promising prospect of HPINs in hyperthermia tumor therapy.

Photothermal therapy (PTT) is another minimally invasive therapeutic technique that utilizes light and PT agents to produce localized heating for the thermal ablation of cancer cells.[95] In this method, localized heating of tumor tissues can be achieved by controlling the regional delivery of PT agents as well as the direction and focus of incident radiation, thus greatly improving the efficiency and specificity of hyperthermia therapy. An ideal PT agent should have the following features: 1) strong absorption in the NIR region ideally between 700 and 1300 nm; 2) high PT conversion efficiency and good thermal conductivity; 3) biocompatibility and no severe toxicity; and 4) potential of being eliminated from the body.

The assembly of NIR-absorbing GNPs with polymers can improve the biocompatibility, PT stability and reduce the possible cytotoxicity of the individual NPs.[96-100] As one of the most commonly used photothermal agents, gold nanorods (GNRs) synthesized by seed-mediated growth method are surface-covered with CTAB

which is known to be toxic to cells and tissues. However, removal of CTAB causes the aggregation of GNRs in buffer or body fluids. In addition, CTAB-stabilized GNRs were rapidly excreted or accumulated in the liver, resulting in reduced PT efficiency at the tumor site. In contrast, polyelectrolyte-coated GNRs were fabricated and showed excellent long-term optical stability in various biological media, thus facilitating their PT ablation of PC3-PSMA human prostate cancer cells.[98]

Most NIR-absorbing GNPs such as Au nanoshells usually have a diameter over 40 nm (sometimes above 100 nm). These NPs with relatively large size often preferentially accumulate in organs such as liver, spleen, and kidneys.[101] It poses a great challenge to eliminate these NPs from the body. In contrast, small NPs (e.g., NPs with diameter below ~8 nm) are more compatible with renal clearance, but at the expense of insufficient absorption in the NIR region, which is required to achieve desired penetration depth in tissue, and to avoid unnecessary damage to healthy tissue.

The assembly of NPs offers an elegant strategy to turn GNPs into strong NIR photoabsorbers for effective imaging and therapy of cancer.[44,66,102,103] Nie et al. demonstrated the assembly of BCP-tethered GNPs into hollow nanovesicles with strong NIR absorbance for multimodality imaging–guided PTT of tumors.[76,77] The absorption peak of the hybrid vesicles can be turned to the NIR range by controlling the size of spherical GNPs, the length and type of BCP tethers. When a BCP of PS-*b*-PCL was used, the strong NIR absorption of vesicular assemblies (~650-800 nm) enables the use of NIR irradiation to excite the hybrid structures to produce heat for PT ablation of human breast cancer cells (MDA-MB-435) in mice (Figure 1.10).[77] After

the irradiation the hybrid vesicles dissociate into individual GNPs which facilitates their rapid clearance from the body.

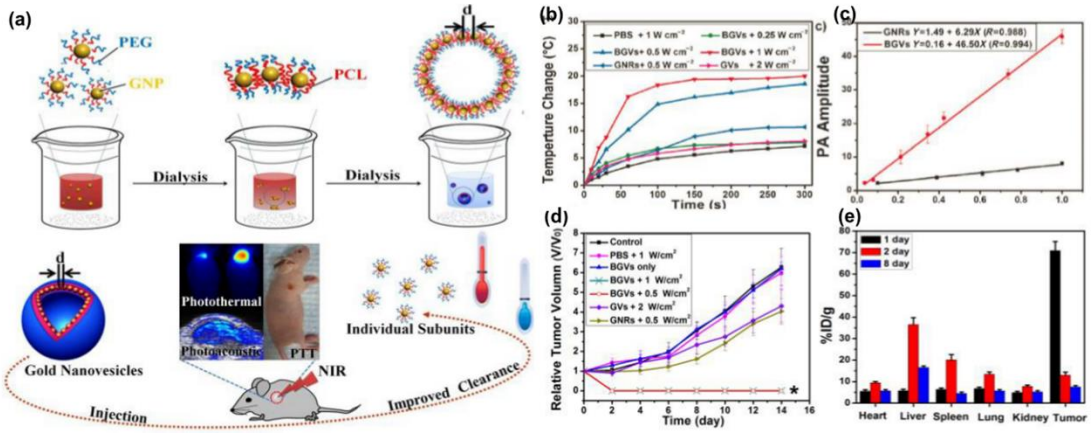

Figure 1.10. (a) Schematic illustration of the self-assembly of biodegradable gold vesicles (BGVs) composed of PEG-b-PCL-tethered GNPs for superior PA imaging and PTT with improved clearance. (b) Heat curves of tumors upon laser irradiation (808 nm laser) as a function of irradiation time. (c) PA signals of BGVs and Au NRs as a function of optical density. (d) Tumor growth curves of different groups of MDA-MB-435 tumor-bearing mice after treatment. (d) Pharmacokinetics of BGVs in different organs at 1, 2, and 8 days after the intratumoral injection of BGVs. Reproduced with permission from Ref. 75. Copyright 2013 WILEY-VCH Verlag GmbH & Co. KGaA, Weinheim.

Nanomaterials-based hypothermia therapy is quite straightforward and easy to implement. The efficacy of the treatment is largely dependent on the accumulation of these NPs at tumor sites and the accessibility of light to those areas. The confinement of heat in the vicinity of NPs makes the treatment very specific. However, this may

cause incomplete ablation of tumor, due to the non-uniform distribution of NPs in tumor areas. Therefore, hypothermia therapy is often used in combination with other therapeutic strategies (e.g., chemotherapy or photodynamic therapy).

Drug Delivery and Combination Therapy

Systemic drug delivery often fails to deliver exact dosage of therapeutic agents specifically to tumor sites at the desired time to suppress cancer metastases.[104,105] Severe side effects may arise from the non-specificity and toxicity of drugs, which can make patients extremely weak and even result in death. Moreover, due to the poor efficacy of non-specific chemotherapy, nearly 50% of all cancer patients will develop drug resistance over times for most of anticancer drugs. For this reason, chemotherapy combined with other strategies (e.g., radiation and PT ablation, photodynamic therapy) is considered as the standard of care for cancer patients particularly at the later stages. HPINs may provide a unique platform for safer and more efficient delivery of therapeutic agents for combination therapy.

Image-guided drug delivery

HPINs have been widely explored for image-guided drug delivery. The imaging capability of inorganic NPs can help identify tumor sites and optimize the pharmacokinetics and biodistribution of drug nanocarriers by tracking their location in cells or tissues. It also makes it possible to trace the *in vivo* release kinetics of therapeutic agents in real time. Duan et al. developed SERS-active hybrid vesicles for simultaneous cancer imaging and targeted drug delivery (Figure 1.11).[106] The hybrid

vesicles with hollow cavity were assembled from GNPs tethered with a mixture of hydrophilic PEG and hydrophobic copolymer (PMMAVP) of MMA and 4-vinylpyridine (4VP) and subsequently conjugated with a monoclonal antibody of HER_2 protein as a cancer biomarker. Raman dye BGLA was also immobilized on the surface of GNP building blocks before assembly. The bioconjugated doxorubicin (Dox) loaded vesicles can specifically target HER_2-positive SKBR-3 breast cancer cells, dissociate and release the payloads in acidic intracellular compartments, due to hydrophobic-to-hydrophilic transition of the hydrophobic PMMAVP in acidic environment. The disassembly of vesicles was associated with dramatic decrease in scattering properties and SERS signals of Raman reporters due to the variation in the plasmonic coupling between GNPs. Upon dissociation of Au vesicles, the SERS intensity of Au vesicles dropped by 34-fold at 1615 cm^{-1} and became very weak, which makes the vesicles traceable by Raman spectroscopy. Thus, the cargo release from the vesicles can be uniquely monitored by dark-field imaging and Raman spectroscopy, which can be used as a direct feedback of the therapy.

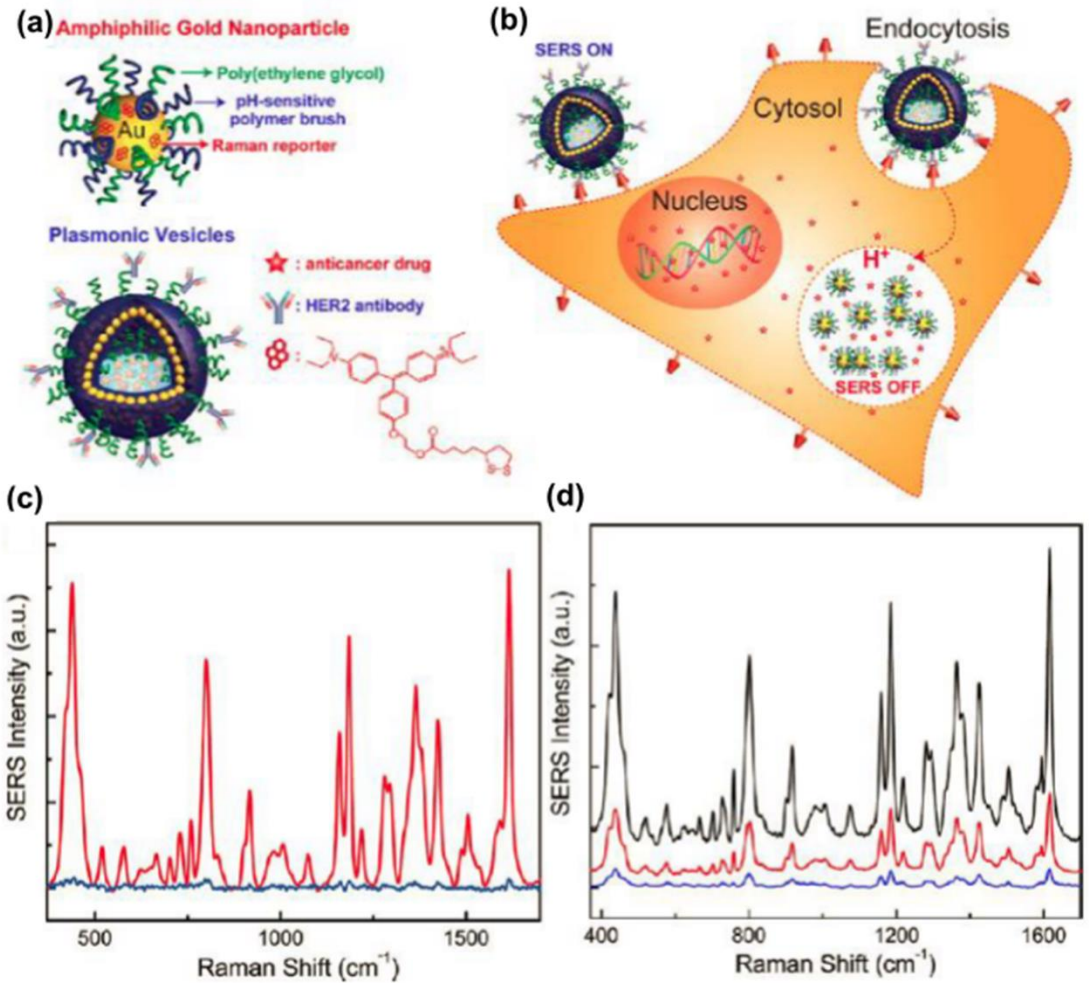

Figure 1.11. (a) Schematic illustration of a GNP coated with Raman reporter BGLA and a mixture of hydrophilic PEG and pH-sensitive hydrophobic PMMAVP polymers and a pH-sensitive drug-loaded plasmonic vesicle surface-immobilized with HER2 antibody for cancer cell targeting. (b) The cellular binding, uptake, and intraorganelle disruption of the SERS-encoded plasmonic vesicles. (c) Raman spectra of the vesicle at pH 7.4 (red) and pH 5.0 (blue). (d) Representative Raman spectra of SKBR-3 cells labeled with targeted vesicles after 30 min incubation (black line) and the post-incubation spectra of the cells at 60 min (red line) and 90 min (blue line). Reproduced with permission from Ref.104. Copyright 2012 American Chemical Society.

Internal Stimuli-triggered Release of Therapeutic Agents

Conventional drug delivery nanocarriers have a limited ability to maintain an effective drug concentration at a desired location and specific time window, due to passive release of payloads. On-demand drug release using stimuli-responsive systems has the potential to achieve spatiotemporal control over an acute level of drug concentration. The microenvironment at tumor sites is slightly different from that at normal tissue, such as lower pH value, different reduction potential, and overexpression of some enzymes. These abnormal changes can be used as internal stimuli for controlled cancer recognition and drug delivery.[106,107]

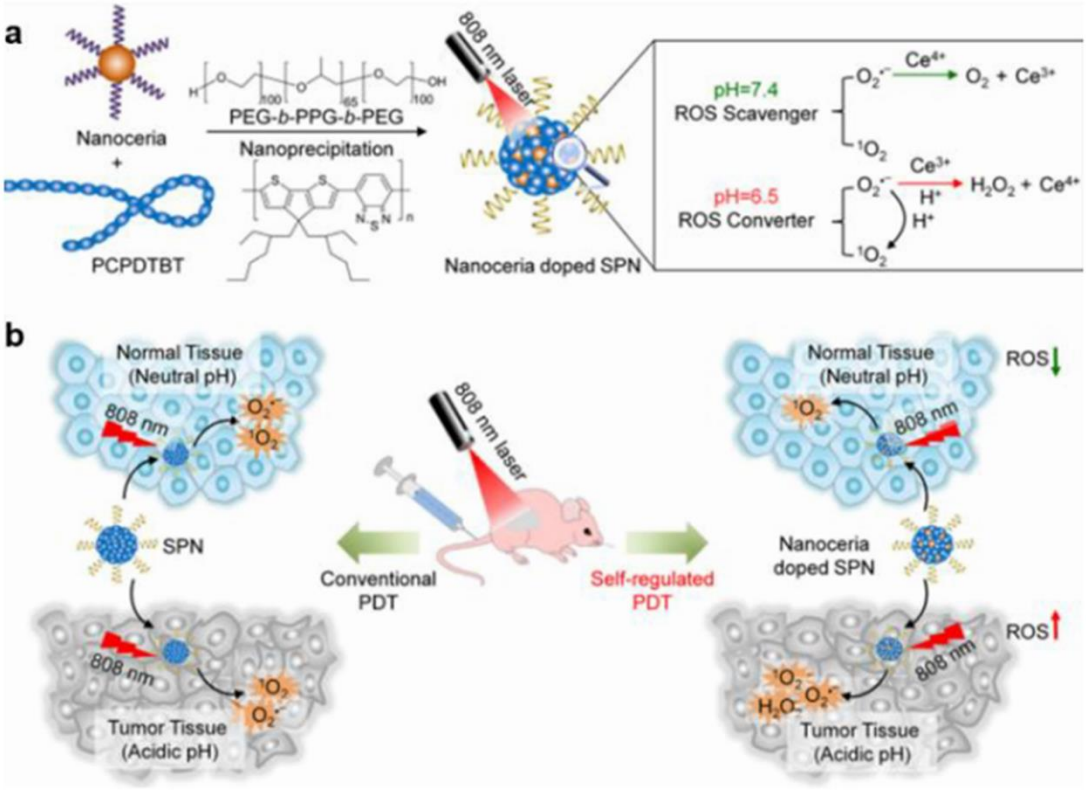

Figure 1.12. Schematic Illustrations of (a) the synthesis of nanoceria-doped SPNs and the self-regulated photodynamic properties of SPNs at physiologically neutral and pathologically acidic conditions and (b) the comparison between self-regulated and conventional PDT-mediated by nanoceria-doped SPNs and nondoped SPNs, respectively. Reproduced with permission from Ref. 106 Copyright 2017 American Chemical Society.

By combining the properties of both polymers and inorganic NPs, HPINs have shown great potential in the design and fabrication of stimuli-responsive delivery vehicles. Pu et al. developed a nanoceria-doped semiconducting polymer NPs (SPNs) to regulate photodynamic cancer therapy in various pH values (Figure 1.12).[108] The SPNs showed strong absorption in the NIR region and served as both fluorescence agents and photosensitizers while nanoceria can act as reactive oxygen species (ROS) scavenger in tumor acidic environment and transfer to converter at neutral pH. In neutral environment, nanoceria can convert ROS into oxygen in a recyclable way due to the presence of the Ce^{3+} (reduced) and Ce^{4+} (oxidized) states on their surface; however, they become the ROS converter to transform $O_2^{\bullet -}$ to H_2O_2 under acidic conditions. The pH-dependent switch of photodynamic properties of SPNs not only amplifies phototherapy in the acidic microenvironment of tumor but also potentially reduces the side effect in normal tissues.

Light-triggered Release of Therapeutic Agents

External stimuli such as light, ultrasound, and magnetic field can be used to activate the release of drug payload from nanocarriers for on-demand therapy. The use of external stimuli offers good flexibility in switching on and off the drug release and superior precision in the control over time, space, and dose of drug release. Compared with others, light is the most frequently used stimulus, largely due to the portability of light sources and ease in application. The light responsiveness of hybrid assemblies can be originated from the responsiveness of polymers, or the PT effect of inorganic components, or the combination of both.

PT heating of loaded inorganic NPs can be used to achieve NIR-responsiveness of hybrid assemblies for deep tissue PTT and controlled drug release. In this case, the design of hybrid assemblies requires either the phase-transition of the polymer matrix, or relatively weak association of polymers (and NPs), or the possession of vesicular membranes which tend to break upon interference. Thin polymer (or composite) membranes tend to break up in response to mechanical force or variation in osmotic pressure or temperature. When NPs are loaded in the hollow cavities, immobilized on the surface, or embedded within the membranes of vesicles or capsules, the localized heating induced by light can break up the thin membrane and trigger the delivery of payload on demand.[50,76,77]

One typical example of NIR-responsive HPINs is the recently emerged new class of plasmonic vesicles comprising a single layer of closely-packed GNPs (or GNRs) in the membrane.[43,50,76,109] Upon laser irradiation, the localized heating of NPs within assemblies dissociated the assembled hybrids to release loaded active compounds, as a result of the conformation change, chemical bonding dissociation of polymers or even

the shape change of NPs. Vesicular assemblies of GNRs tethered with amphiphilic BCPs of PS-*b*-PEO could be fabricated by microfluidic method, and the NIR-light triggered release of payloads was evaluated for drug release.[43] Upon the irradiation of NIR pulsed laser beam (60 mW, 808 nm), the membrane of vesicular hybrids was disturbed to release encapsulated model drug, rhodamine B. A close inspection indicated that GNRs within membranes were melted and deformed to spherical GNPs, as a result of intensive localized heating. A comparison between systems with laser on and off clearly demonstrated light controlled release of payload from the vesicles (Figure 1.13).

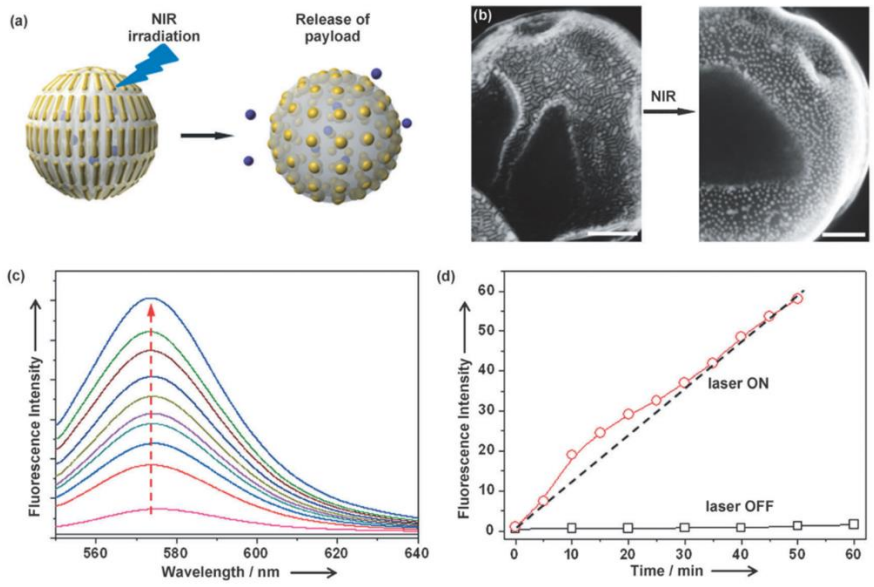

Figure 1.13. a) NIR-triggered release using giant vesicles. The photothermally induced shape deformation of GNRs to spherical GNPs creates extra spacing between GNPs for the release of encapsulated molecules. b) SEM images of giant vesicles before and after exposed to NIR laser. The GNRs in the vesicles deformed to spherical GNPs upon irradiation. Scale bars are 200 nm. c) The fluorescence emission spectra of the released

Rhodamine B (excitation at 540 nm) with a 5 min interval under the irradiation of 800 nm laser. d) The release profiles of Rhodamin B giant vesicles with laser on (○) and off (□). Reproduced with permission from Ref. 41. Copyright 2013 WILEY-VCH Verlag GmbH & Co. KGaA, Weinheim.

1.3 Scope of the dissertation

As discussed in previous sections, the assembly of inorganic NPs into HPINs offers a variety of desired properties for biological imaging and therapy. I have chosen colloidal amphiphiles as building blocks for fabricating functional HPINs, because of *i) their intrinsic and collective physiochemical properties arising after the assembly and ii) their capacity to mimic molecular self-assembly to form various assembly structures.* The objective of this dissertation is *to study the self-assembly of inorganic NPs into HPINs, to tailor the properties of the assemblies and to improve the performance of assembled materials in biomedical applications.*

Chapter 2: Plasmonic vesicles-based signal amplification for ultrasensitive colorimetric assay of disease biomarkers

Overview. In this work, we demonstrate an enzyme-free signal amplification technique, based on gold vesicles encapsulated with Pd−Ir nanoparticles as peroxidase mimics, for colorimetric assay of disease biomarkers with significantly enhanced sensitivity. This technique overcomes the intrinsic limitations of enzymes, thanks to the superior catalytic efficiency of peroxidase mimics and the efficient loading and release of these mimics. Using human prostate surface antigen as a model biomarker, we demonstrated that the enzyme-free assay could reach a limit of detection at the femtogram/mL level, which is over 103-fold lower than that of conventional enzyme-based assay when the same antibodies and similar procedures were used.

This chapter is adapted from the manuscript published in the following article: Ye, H.[†], Yang, K.[†], Tao, J., Liu, Y., Zhang, Q., Habibi, S., Nie, Z.[#] and Xia X.[#], An Enzyme-Free Signal Amplification Technique for Ultrasensitive Colorimetric Assay of Disease Biomarkers, *ACS Nano*, **2017**, 11 (2), 2052–2059. My works include the design of nanoassemblies, encapsulation and release of Pd−Ir nanoparticles and their catalytic efficiency after the release. ([†] Equal contribution)

2.1 Introduction

Simple and affordable technologies for detection of disease biomarkers are essential to the improvement of standard of living, especially for resource-constrained areas or countries. Enzyme-based colorimetric assays (e.g., enzyme-linked immunosorbent assay (ELISA), immunohistochemistry, and Western blot) are broadly

recognized as such kind of technology because they can be performed by less-trained personnel with an inexpensive spectrophotometer, ordinary light microscope, or even naked eyes.[110-112] Nevertheless, the major drawback for these colorimetric assays is the relatively low detection sensitivity compared to other technologies such as those based on fluorescence and plasmonics.[113-115]

In conventional colorimetric assays, the detectable color signal is generated from enzymes (in many cases, horseradish peroxidase, HRP) which are conjugated to antibodies and specifically convert substrates to colored molecules. Therefore, their detection sensitivity is largely determined by the performance of enzymes. Accordingly, a general strategy for enhancing the sensitivity is to amplify color signal by assembling as many enzyme molecules as possible on certain carriers (e.g., avidin, polymers, and nanoparticles).[116-122] For example, Merkoci et al. conjugated HRPs to gold nanoparticles (GNPs) as carriers and applied these conjugates as labels to ELISA of breast cancer biomarker, of which detection sensitivity was several times higher than conventional ELISA using HRP as label.[120] Qian et al. further increased HRP loading amount by employing a combination of GNPs and grapheme oxide sheets as carriers, achieving a 64-fold improvement of sensitivity.[121] Despite these demonstrations, the detection sensitivity is ultimately limited by the catalytic efficiency of enzymes and the loading amount of enzymes on a carrier.

This chapter describes an enzyme-free signal amplification technique to break the intrinsic limitations of enzymes, achieving substantially enhanced detection sensitivity. In this technique, sub-10 nm Pd-Ir nanoparticles (NPs) encapsulated gold vesicles (referred to as "Pd-Ir NPs@GVs") are employed as alternatives to enzymes. In this

study, we used ELISA as a model platform to demonstrate the enzyme-free technique, because ELISA has been the gold standard for detection and quantification of protein biomarkers for decades. As shown in Figure 2.1, at elevated temperature, gold vesicles (GVs) captured by analytes liberate thousands of individual Pd-Ir NPs because of the heat-induced breakup of the GV membrane.[44,76,77] The released Pd-Ir NPs act as peroxidase mimics and generate intense color signal by catalyzing the oxidation of 3,3',5,5'-tetramethylbenzidine (TMB, a classic HRP substrate) by H_2O_2.[123] It should be pointed out that we have recently demonstrated the peroxidase-like property of Pd-Ir NPs and controlled release of GVs, respectively. However, to date, there has been no report yet on the development of a signal amplification platform based on the combination of these two systems. The ultralow detection limit of this enzyme-free ELISA arises from the following distinctive features of the amplification technique: (i) Pd-Ir NPs as enzyme mimics possess much higher catalytic efficiency than natural enzymes, providing enhanced color signal; (ii) the loading capacity of enzyme mimics is maximized by taking advantage of the large interior 3D space of the GVs as carriers;[124,125] in contrast, the loading of enzymes on carriers in current designs of ELISA is limited by the surface area that allows for the conjugation of enzymes; (iii) the loading of label-free enzyme mimics of Pd-Ir NPs in the pocket of GVs avoids the loss of catalytic efficiency caused by chemical conjugation; (iv) Pd-Ir NPs could disperse in catalytic reaction solution upon release, making them more active than immobilized catalysts on solid surfaces, which is the case for conventional ELISAs.

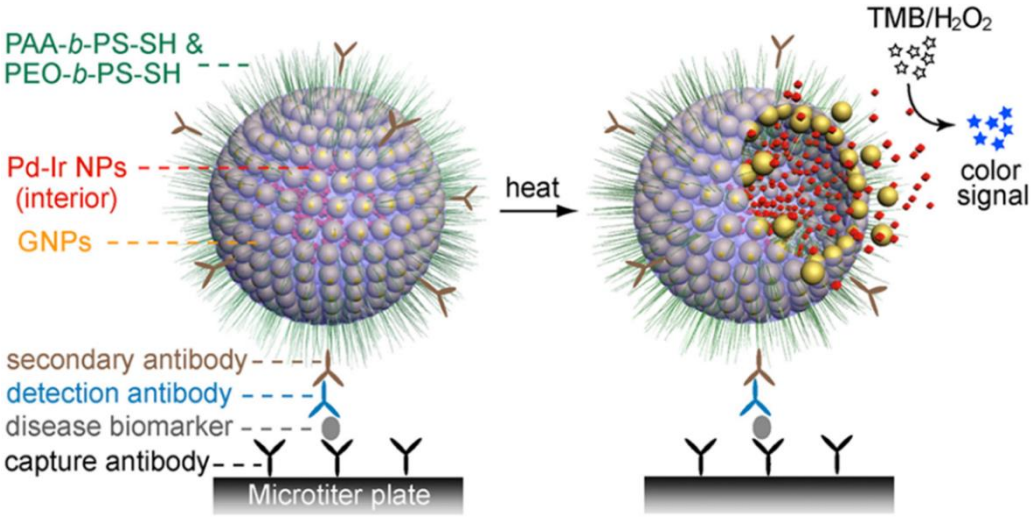

Figure 2.1. Schematic illustration of utilizing Pd-Ir NPs@GVs based ELISA for detection of disease biomarkers. The Pd-Ir NPs released from captured GVs act as effective peroxidase mimics to catalyze chromogenic substrates.

2.2 Experiments

2.2.1 Materials

Sodium hexachloroiridate(III) hydrate ($Na_3IrCl_6 \cdot xH_2O$, MW=473.9), sodium tetrachloropalladate(II) (Na_2PdCl_4, 98%), gold(III) chloride trihydrate ($HAuCl_4 \cdot 3H_2O$, ≥ 99.9%), potassium bromide (KBr, ≥ 99%), L-ascorbic acid (AA, ≥ 99%), poly(vinylpyrrolidone) (PVP, MW ≈ 55 000), 3,3',5,5'-tetramethylbenzidine (TMB, > 99%), hydrogen peroxide solution (30 wt % in H_2O), acetic acid (HOAc, ≥ 99.7%), sodium acetate (NaOAc, ≥ 99%), human prostate surface antigen (PSA, ≥ 99%), Tween 20, bovine serum albumin (BSA, ≥ 98%), sodium chloride (NaCl, ≥ 99.5%), potassium chloride (KCl, ≥ 99%), N-hydroxysulfosuccinimide sodium salt (NHS, ≥ 98%), N-

Ethyl-N'-(3-(dimethylamino)-propyl)carbodiimide hydrochloride (EDC, ≥ 99%), sodium phosphate dibasic (Na_2HPO_4, ≥ 99%), potassium phosphate monobasic (KH_2PO_4, ≥ 99%), tris base (≥ 99.9%), sodium citrate, dimethylformamide (DMF), tetrahydrofuran (THF), sodium azide (NaN_3, ≥ 99.5%), and sulfuric acid (H_2SO_4, 95-98%) were all obtained from Sigma-Aldrich. Ethylene glycol (EG) was obtained from J. T. Baker. Mouse anti-PSA monoclonal antibody (mouse anti-PSA mAb) and rabbit anti-PSA polyclonal antibody (rabbit anti-PSA pAb) were obtained from Abcam plc. Goat antimouse IgG and HRP-goat antimouse IgG conjugate were obtained from Thermo Fisher Scientific, Inc. 96-well microtiter plates (polystyrene, clear, flat bottom) was obtained from Corning Inc. All aqueous solutions were prepared using deionized (DI) water with a resistivity of 18.0 M Ω·cm.

2.2.2 Preparation of 5.6 nm Pd truncated octahedra as seeds

In a typical synthesis, 30 mL of an EG solution containing 600 mg of PVP was hosted in a glass vial and preheated to 160 ° C in an oil bath under magnetic stirring for 10 min. Then, 15 mL of an EG solution containing 240 mg of Na_2PdCl_4 was quickly injected into the reaction solution using a pipet. The reaction was allowed to continue for 3 h. After being washed with acetone once and ethanol twice via centrifugation, the final product was redispersed in 10 mL of EG for future use. The concentration of Pd element in the final product was determined to be 7.5 mg/mL by ICP-OES, which could be converted to a particle concentration of ~ 5×10^{15} particles/mL (assuming that the particles were perfect octahedra).

2.2.3 Preparation of Pd-Ir core-shell nanoparticles (Pd-Ir NPs)

Pd-Ir NPs were prepared by coating a monolayer of Ir on Pd seeds according to our previously published procedure with some modifications.20 In a standard procedure, 100 mg of PVP and 60 mg of AA were mixed with the 10 mL Pd seeds in EG and were hosted in a 50 mL three-neck fl ask. The mixture was preheated to 200 ° C in an oil bath under magnetic stirring for 10 min. Then, 8.0 mL of $Na_3IrCl_6 \cdot xH_2O$ solution (7.0 mg/mL, in EG) was injected to the fl ask at a rate of 1.5 mL/h using a syringe pump. The reaction was allowed to proceed for an additional 10 min after the $Na_3IrCl_6 \cdot xH_2O$ precursor had been completed injected. The products (i.e., Pd-Ir NPs) were collected by centrifugation, washed once with acetone, two times with water, and finally redispersed in 1 mL of DI water for future use. Particle concentration for the suspension of Pd-Ir NPs was estimated to be 4.5×10^{16} by ICP-OES.

2.2.4 Evaluation of peroxidase-like activity

Peroxidase-like activity was measured by the steady-state kinetic assays.[126] All assays were carried out at room temperature in 1.0-mL cuvettes (path length, l = 1.0 cm), with 0.2 M NaOAc/HOAc solution, pH 4.0 being used as the reaction buffer. After addition of TMB and H_2O_2 in the buffer system containing nanoparticles as peroxidase mimics, the absorbance of the reaction solution at 653 nm of each sample was immediately measured as a function of time with interval of 6s using a spectrophotometer for 3 min. These "Absorbance vs Time" plots were then used to obtain the slope at the initial point (Slope Initial) of each reaction by conducting the first derivation of each curve using OriginPro 9.0 software. The initial reaction velocity

(ν) was calculated by $Slope_{Initial}$ /($\varepsilon_{TMB\text{-}653nm}$ × l), where $\varepsilon_{TMB\text{-}653nm}$ is the molar extinction coefficient of TMB at 653 nm that equals $3.9 \times 10^4 M^{-1} \cdot cm^{-1}$. The plots of ν against TMB concentrations ([S]) were fitted using nonlinear regression of the Michaelis − Menten equation. The apparent kinetic parameters K m and V max were obtained from the double reciprocal plot (or Lineweaver − Burk plot) that was generated from the Michaelis − Menten equation $\nu = V_{max} \times [S]/(K_m + [S])$,47 where V_{max} is the maximal reaction velocity and K_m is the Michaelis constant. K_{cat} was derived from $K_{cat} = V_{max} / [E]$, where [E] represents the particle concentration of peroxidase mimics.

2.2.5 Synthesis of amphiphilic block copolymers and gold nanoparticles

Amphiphilic BCPs of poly(ethylene oxide)-*b*-polystyrene and poly(acrylic acid)-*b*-polystyrene terminated with a thiol group at polystyrene end (PEO-*b*-PS-SH and PAA-*b*-PS-SH) were synthesized following the reversible addition fragmentation chain transfer (RAFT) polymerization procedures reported previously.[66] The BCPs samples were designed with similar polystyrene (PS) lengths (PEO_{45}-*b*-PS_{260}-SH and PAA_{23}-*b*-PS_{250}-SH) as verified by proton nuclear magnetic resonance (^{1}H NMR).

GNPs with diameters of 33.0 ± 4.7 nm were prepared by sodium citrate reduction method.[127] Briefly, a 10 mg of $HAuCl_4$ was dissolved in 500 mL H_2O and heated to boiling under stirring. A 3 mL of sodium citrate (1 wt %) solution was then quickly injected. The reaction mixture was refluxed for 30 min and then used as seeds for further growth of GNPs in the presence of sodium citrate at 80 ° C. The resultant 33.0 nm GNPs were collected by centrifugation.

2.2.6 Preparation of gold vesicles (GVs) and Pd-Ir NPs@GVs

GVs and Pd-Ir NPs@GVs were prepared by assembling BCP-tethered GNPs in the presence of DI water or aqueous suspension of Pd-Ir NPs, respectively, according to our previously reported procedure with minor modifications.[44]

The surface of GNPs was modified with BCPs using the ligand exchange method. A 5 mg BCPs of PEO45-b-PS260-SH and PAA23-b-PS250-SH with a molar ratio of 20:1 were dissolved in 10 mL DMF. Then, a concentrated solution of GNPs (~2 mg/mL) was slowly added into the BCP solution under vigorous shaking. The mixture was subsequently sonicated for 1 h to avoid the aggregation of GNPs and was then kept static without stirring overnight. The BCP-tethered GNPs were purified by removing free polymers through centrifugation (6-8 times) and were finally redispersed in THF at a concentration of ~ 0.05 mg/mL.

Self-assembly of BCP-tethered GNPs was conducted by the film rehydration method as reported previously.[37] Briefly, a solution of BCP-modified GNPs in THF was first dried under nitrogen flow to form a thin film on a glass substrate, followed by rehydration in DI water (for pristine GVs) or an aqueous suspension of Pd-Ir NPs at 4.5×10^{16} particles/mL (for Pd-Ir NPs@GVs) with sonication for 1 min. The resultant GVs and Pd-Ir NPs@GVs were collected by centrifugation (5000 rpm, 5 min), washed 8 times with DI water, and finally redispersed in water for future use.

2.2.7 Preparation of Pd-Ir NPs@GVs-goat antimouse IgG conjugates

Antimouse IgG was conjugated to Pd-Ir NPs@GVs using EDC and NHS as coupling agents (Figure 2.2).[128] In brief, 50 μL of Pd-Ir NPs@GVs (~ 0.5 mg/mL in terms of Au element, in DI water) was added to a 450 μL of 10 mM phosphate buffered saline (PBS, pH 7.4) buffer at room temperature under stirring. Then, 5 μL of EDC (25 mM, in DI water) and 5 μL of NHS (50 mM, in DI water) were added. After 15 min, the particles were washed with DI water twice and redispersed in 50 μL PBS. Subsequently, 50 μL of goat antimouse IgG (2 mg/mL, in PBS) was added to the particle suspension. After incubation at room temperature for 30 min, the reaction solution was put in a refrigerator overnight at 4 ° C. Then, 100 μL of blocking solution (5% BSA in PBS) was added to the reaction solution. After 2 h, the final products were collected by centrifugation, washed twice with PBS, and redispersed in 50 μL of PBS containing 1% BSA and 0.05% NaN_3 for future use.

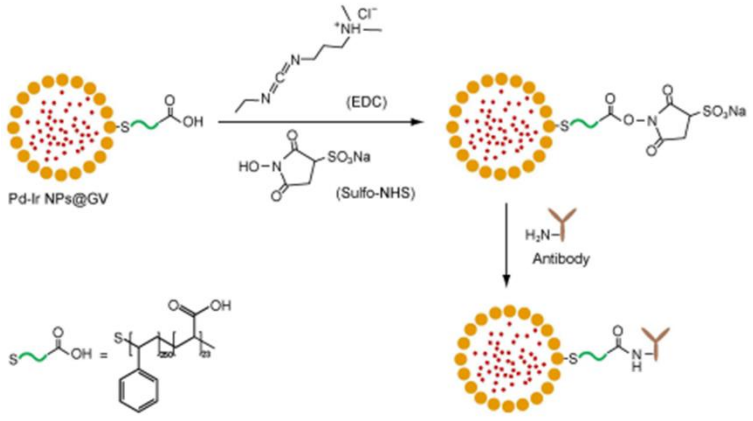

Figure 2.2 Schematic illustration showing the procedure for conjugation of antibodies (e.g., goat anti-mouse IgG) onto Pd-Ir NPs@GVs.

2.2.8 Pd-Ir NPs@GVs-Based ELISA of PSA

First, 96-well microtiter plates were coated with rabbit anti-PSA pAb (100 μL per well, 5 μg/mL in carbonate/bicarbonate buffer pH9.6) at 4 ° C overnight. After washing the plates three times with washing buffer (10 mM PBS pH 7.4 containing 0.5% tween 20, PBST), the plates were blocked with 200 μL blocking buffer (3% BSA in PBST) for 2 h at room temperature. The plates were then washed three times with washing buffer, followed by the addition of 100 μL PSA standards or human plasma sample in dilution buffer (1% BSA in PBST). Note that plasma was prediluted 2 folds by dilution buffer prior to spiking of PSA and detection. After shaking at room temperature for 2 h, the plates were washed three times with washing buffer, and 100 μL mouse anti-PSA mAb (2 μg/mL, in dilution buffer) was added. After 1 h shake at room temperature, the plates were washed three times, and 100 μL Pd-Ir NPs@GVs-goat antimouse IgG conjugates (1:2000, in dilution buffer) was added, followed by 30 min shake at room temperature. After washing four times, 60 μL DI water was added. After being sealed with a plastic film, the plate was put to an oven set to 90 ° C for 1 h. After the plate had been cooled down to room temperature, 50 μL freshly prepared substrate solution (1.6 mM TMB and 4.0 M H_2O_2 in 0.4 M HOAc/NaOAc buffer, pH 4.0) was added to each well. After 30 min incubation at room temperature, 50 μL of 2 M H_2SO_4 as a stopping solution was added. The absorbance of each well at 450 nm was read using a microplate reader. The procedure of HRP based ELISA was the same as the Pd-Ir NPs@GVs-based ELISA except for the substitutions of Pd-Ir NPs@GVs-goat antimouse IgG conjugates with 100 μL HRP-goat antimouse IgG conjugates (1 μg/mL, in dilution buffer), the difference in the components of substrate solution (0.8 mM TMB and 5

mM H_2O_2 in citric acid-Na_2HPO_4 buffer, pH 5.0), and the exclusion of heat treatment step.

2.2.9 Characterizations

The UV-vis spectra were recorded using an Agilent Cary 60 UV-vis spectrophotometer. TEM images were taken using a JEOL JEM-2010 microscope operated at 200 kV. High resolution TEM (HRTEM) images, high-angle annular dark-field scanning TEM (HAADF-STEM) images and energy dispersive X-ray (EDX) mapping were acquired using a double Cs-corrected JEOL ARM200F TEM at Brookhaven National Laboratory. The concentration of Pd, Ir, and Au ions were determined using an inductively coupled plasma-optical emission spectroscopy (ICP-OES, PerkinElmer Optima 7000DV), which could be converted to the particle concentration of Pd seeds, Pd − Ir NPs, and Au NPs once the particle sizes and shapes had been resolved by TEM imaging. The X-ray photoelectron spectroscopy (XPS) measurements were performed on an SSX-100 system (Surface Science Laboratories, Inc.) equipped with a monochromated Al K_α X-ray source, a hemispherical sector analyzer (HSA) and a resistive anode detector. X-ray diffraction (XRD) pattern was taken using a Scintag XDS2000 powder diffractometer. Dynamic light scattering (DLS) analysis was conducted using a Photocor-FC light scattering instrument. ^{1}H NMR spectra were recorded with a Bruker AV-400 MHz high-resolution NMR spectrometer in $CDCl_3$. The absorbance of samples in microtiter plates was read using a PerkinElmer Victor 3 1420 Multilabel Plate Reader. Microtiter plates were shaken using a Corning LSE Digital Microplate Shaker. pH values of buffer solutions were measured using an

Oakton pH 700 Benchtop Meter. Photographs of samples in tubes and microplates were taken using a Canon EOS Rebel T5 digital camera.

2.3 Results and discussion

2.3.1 Synthesis and Characterization of Pd-Ir NPs

Pd-Ir NPs were synthesized by coating an ultrathin layer of Ir on preformed sub-10 nm Pd seeds. The Pd-Ir NPs exhibit a high purity (>95%) and good uniformity (Figures 2.3a). A close inspection of the NPs shows that the Pd seeds retained their truncated octahedral shape after the deposition of Ir, indicating a conformal coating of Ir (Figure 2.3b). The average size of the Pd-Ir NPs was measured to be 6.1 nm, which was 0.5 nm greater than that of the initial Pd seeds. Therefore, the average thickness of the deposited Ir shells was about 0.25 nm, indicating an approximate monolayer coating of Ir on Pd(111) surfaces.[129]

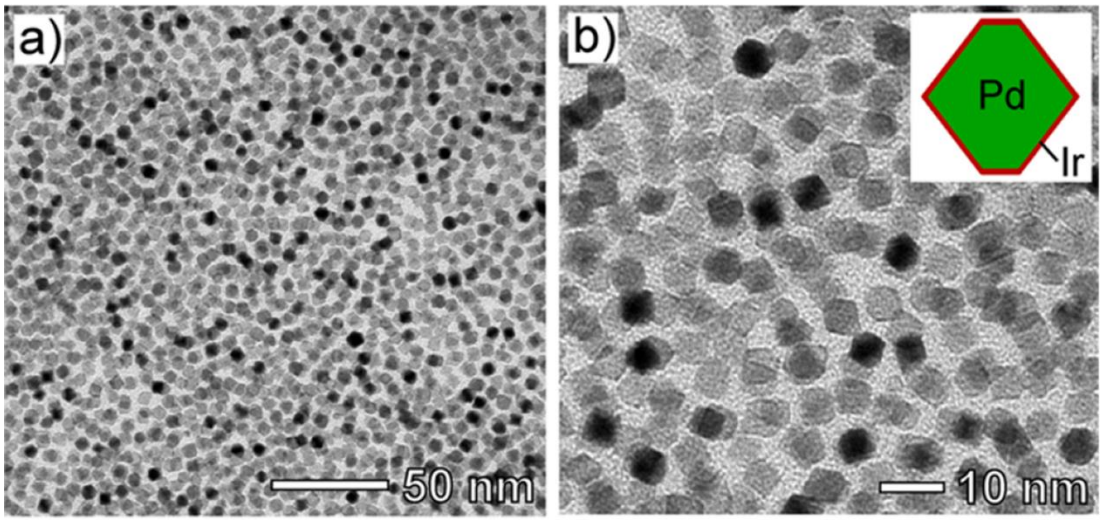

Figure 2.3 Structural and compositional analyses of Pd-Ir NPs prepared by depositing Ir atoms on 5.6 nm Pd truncated octahedral seeds. (a,b) low (a) and high (b) magnification TEM image of Pd-Ir NPs. The inset is a 2D schematic model.

2.3.2 Peroxidase-like Activity of Pd-Ir NPs

We quantitatively evaluated the peroxidase-like activity of as-synthesized Pd-Ir NPs by apparent steady-state kinetic assay (Figure 2.4). Oxidation of TMB by H_2O_2 was chosen as a model catalytic reaction. The catalytic efficiency, in terms of catalytic constant (K_{cat}, which measures the maximum number of colored products generated per enzyme/mimic per second), for the Pd-Ir NPs was measured to be 1.1×10^5 s^{-1}. In comparison, the values of K_{cat} for initial Pd seeds and HRP were 4.8×10^3 and 4.0×10^3 s^{-1}, respectively.[130] This data suggests that (i) The Pd-Ir NPs are ~ 28 times more efficient than HRP in generating color products (i.e., oxidized TMB with maximum absorbance at 653 nm)[131,132]; and (ii) the enhanced catalytic efficiency for Pd-Ir NPs was ascribed to the coating of Ir monolayer on Pd seeds.

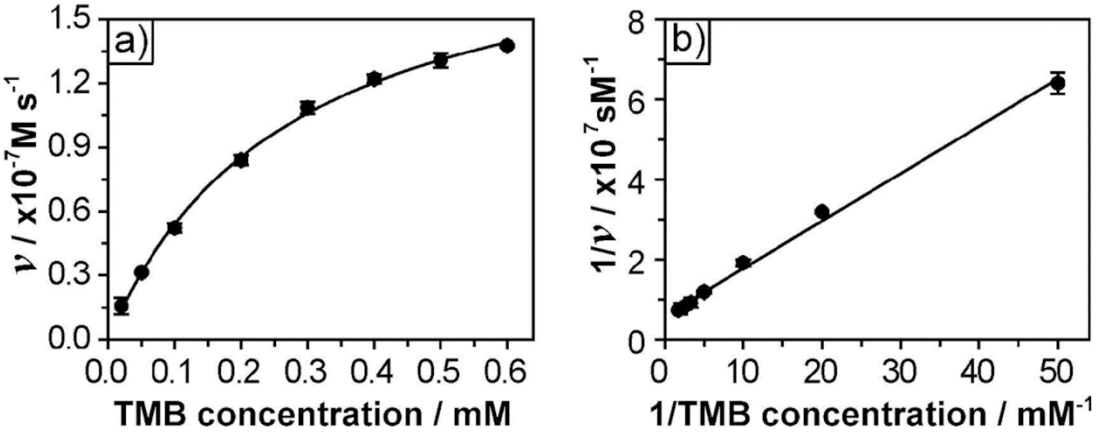

Figure 2.4 Kinetic assays of using Pd-Ir NPs as peroxidase mimics for the oxidation of TMB by H_2O_2. (a) Plot of initial reaction velocity (*v*) as a function of TMB concentration. (b) Double-reciprocal plot generated from (a), from which the kinetics parameters were derived. Error bars in the plots indicate standard deviations of three independent measurements.

2.3.3 Encapsulation of Pd-Ir NPs to GVs

We then encapsulated the Pd-Ir NPs into GVs that were achieved by assembling block copolymers (BCPs)-tethered GNPs in an aqueous suspension of Pd-Ir NPs. GNPs with a diameter of 33.0 ± 4.7 nm were first modified with thiol-terminated BCPs of poly(ethylene oxide)-*b*-polystyrene (PEO_{45}-*b*-PS_{260}-SH) and poly(acrylic acid)-*b*-polystyrene (PAA_{23}-*b*-PS_{250}-SH) at a molar ratio of 20:1. It should be mentioned that we chose these GNPs of ~ 33 nm for the assemble of vesicles mainly because (i) the ease in the functionalization of GNPs with polymers via Au-S bond, in order to trigger the formation of GVs and to conjugate biological moieties for sensing; (ii) the good stability of resultant GVs and their capability in retaining molecules (or nanoparticles) without noticeable leakage for a long time; our previous studies showed that GVs remain stable for months and minimal leakage of small organic molecules (or drugs) was observed from GVs after weeks, presumably owing to the jamming of particles in the vesicular membranes; in contrast, small molecules tend to leak out from liposomes or polymersomes within a few hours, which makes them less attractive for the present application;[133] (iii) these GNPs are relatively uniform and monodisperse; (iv) the GNP size of 33 nm is significantly larger than that of Pd-Ir NPs (i.e., 6.1 nm), making it

convenient to distinguish Pd-Ir NPs from GNPs under electron microscope that is critical for monitoring the heat-induced NP release process.

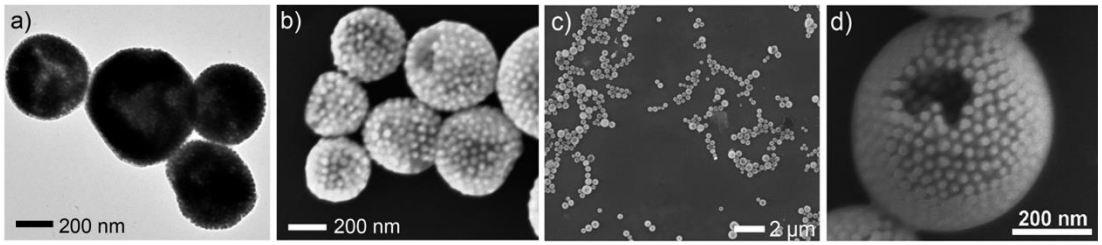

Figure 2.5 Electron microscopy characterizations of as-prepared Pd-Ir NPs@GVs. (a,b) magnified TEM and SEM images, respectively, showing the overall spherical shape of the products. (c) low-magnification SETM image showing the yield and size distribution of the products. (d) SEM image of an individual particle with a cavity on the GV surface, showing that the GVs were composed of a monolayer of GNPs.

A film rehydration method, which is widely used for scalable fabrication of liposomes in pharmaceutic industry, was used to fabricate the GVs. Specifically, pristine GVs were prepared by rehydrating a film of BCP-tethered GNPs in water under sonication, according to our previously published procedures.[44] To encapsulate Pd-Ir NPs into GVs, an aqueous suspension of Pd-Ir NPs at a high concentration (~4.5×10^{16} particles/mL) was used for the rehydration process. As indicated by the TEM and scanning electron microscopy (SEM) images shown in Figure 2.5, the Pd-Ir NPs@GVs showed an overall spherical shape. The low-magnification SEM image demonstrated that the Pd-Ir NPs@GVs could be obtained with a high purity and a good uniformity. Our analyses on 100 random particles indicated that the products had an average diameter of ~400 nm with a standard deviation of 48 nm. The vesicular membranes of

the GVs were composed of a monolayer of densely packed GNPs, which is consistent with our previous studies.[44] On the basis of the packing density and size of GV, the average number of GNPs in an individual GV was roughly estimated to be 339. The loading amount of Pd-Ir NPs in individual GVs was estimated to be 1232 by quantifying elemental Pd and Au in GVs using ICP-OES.

2.3.4 Heat-Triggered Release of Pd-Ir NPs

To demonstrate the heat-triggered release of Pd-Ir NPs from GVs, we incubated aqueous suspensions of Pd-Ir NPs@GVs (~0.5 mg/mL in terms of Au element) at different temperatures for 1 h. The morphological change of samples caused by heat treatment was monitored by TEM and SEM. We found that the assembled GVs gradually collapsed as the temperature increased (Figure 2.6). Compared to the initial Pd-Ir NPs@GVs (Figure 2.6a,e), small holes started to appear in the membranes of GVs when the temperature was set to 70 ° C (Figure 2.6b, f). At 80 ° C, the holes in GVs became more evident and fragments began to fall off from the vesicles (Figure 2.6c, g). Finally, most of the GVs completely collapsed after 90 ° C treatment (Figure 2.6d, h). We presume that the dissociation of GNPs is attributed to the breakup of Au-S bonds due to the thermal instability of the bonds at a temperature above 70° C.[134,135] The disassembly of GVs is associated with the release of encapsulated Pd-Ir NPs (Figure 2.6b-d). A number of Pd-Ir NPs can be observed outside the GVs.

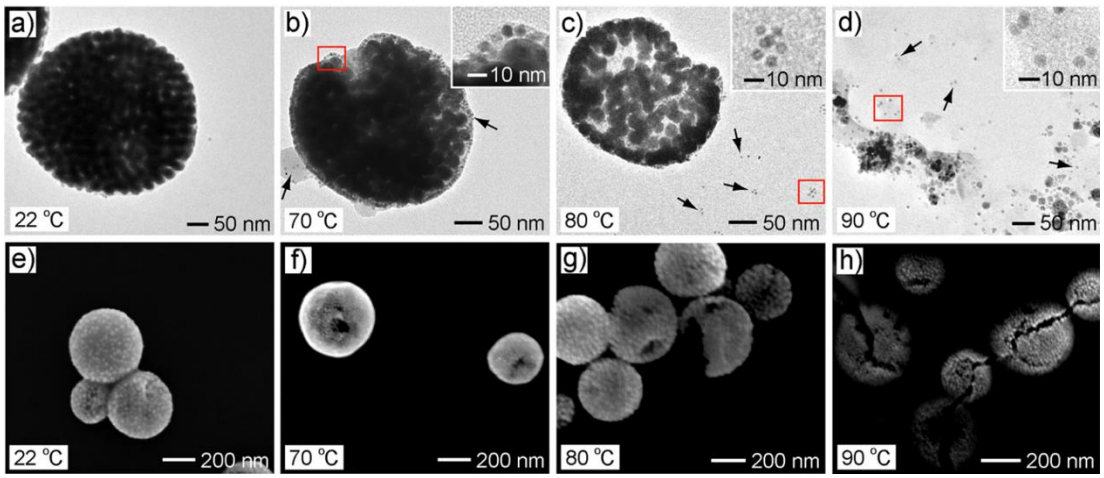

Figure 2.6 Heat-triggered release of Pd-Ir NPs from GVs. Representative (a-d) TEM and (e-h) SEM images of the Pd-Ir NPs@GVs treated at different temperatures (marked in each image) for 1 h. In (b-d), insets show magnified TEM images of corresponding regions marked by red boxes. Some of the released Pd-Ir NPs are indicated by black arrows.

The heat-triggered release of Pd-Ir NPs is further confirmed by dynamic light scattering (DLS) analysis. Pristine GVs and Pd-Ir NPs were used as control groups. As shown in Figure 2.7, after heating at 90 ° C for 1 h, the major size distribution peak of Pd-Ir NPs@GVs suspension shifted from 380 nm (solid, blue) to 260 nm (dashed, blue). In addition, two shoulder peaks at ~ 8.5 nm and ~ 32 nm were observed. The 8.5 nm peak matched well with the peak of pristine Pd-Ir NPs (solid, red), indicating the successful release of Pd − Ir NPs from GVs. The 32 nm peak could be assigned to the dissociated GNPs from GVs since this peak was also observed for pristine GVs after they had been heated (dashed, black). Thermal treatment at 90 ° C for 1 h was adopted for subsequent ELISA experiments. We are aware that heating for 1 h may limit the

practical application of the platform for assays. The operation time of assays can be drastically reduced by speeding up the release of payload from GVs via the irradiation of near-infrared light or the use of thermoresponsive polymer tethers.

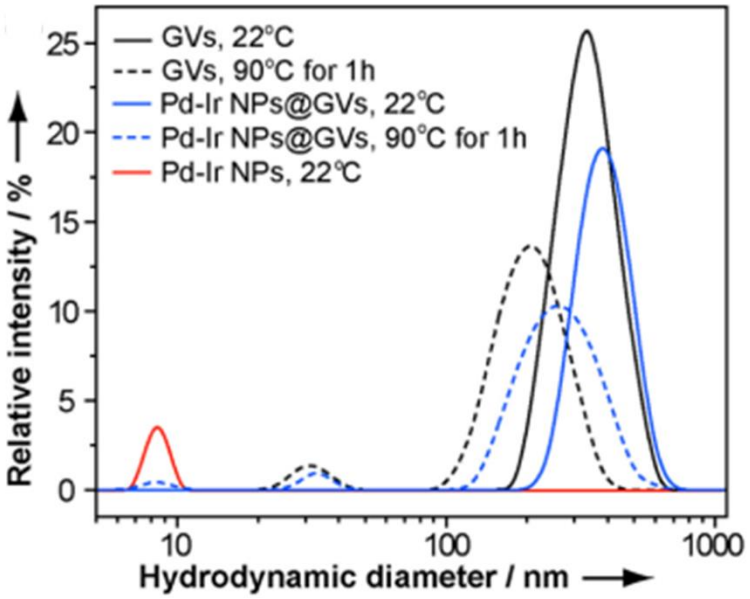

Figure 2.7 DLS analysis of different samples: GVs (black), Pd-Ir NPs@GVs (blue), and Pd-Ir NPs (red) before and after heat treatment (90 °C, 1 h)

2.3.5 Demonstration of signal amplification

We also designed a set of experiments to demonstrate the color signal amplification mechanism shown in Figure 2.1. Briefly, aliquots were taken from an aqueous suspension of Pd-Ir NPs@GVs before and after it had been heated at 90 °C for 1 h and were employed as catalysts for the oxidation of TMB by H_2O_2. Colored products were quantified by measuring the absorbance at 653 nm, t = 2 min. For comparison, aqueous suspensions of pristine GVs and Pd-Ir NPs with the same amounts of GVs and Pd-Ir

NPs (determined by ICP-OES), respectively, as those in Pd-Ir NPs@GVs were also tested. As shown in Figure 2.8, before heat treatment, the reaction solution with the presence of Pd-Ir NPs@GVs was nearly colorless with $A_{653nm} \approx 0.04$. After heat treatment, the catalytic activity of Pd-Ir NPs@GVs was dramatically enhanced, generating an intense blue color ($A_{653nm} = 1.6$, see the inset of Figure 2.8). Since almost no absorbance at 653 nm was observed for GVs catalyzed reaction solutions, the enhanced catalytic activity for heat treated Pd-Ir NPs@GVs could be ascribed to the free Pd-Ir NPs released from GVs. It should be mentioned that, before heat treatment, the absorbance of Pd-Ir NPs@GVs catalyzed reaction solution was similar to that of GVs catalyzed reaction solution. This observation demonstrated that the GVs could effectively prevent the leakage of encapsulated Pd-Ir NPs when there is no heating. On the basis of the values of A_{653nm}, heat treated Pd-Ir NPs@GVs was as active as pristine Pd-Ir NPs, indicating that most of the Pd-Ir NPs had been released from GVs and their catalytic efficiency was well retained. Taken together, these results clearly demonstrated the signal amplification mechanism described in Figure 2.1.

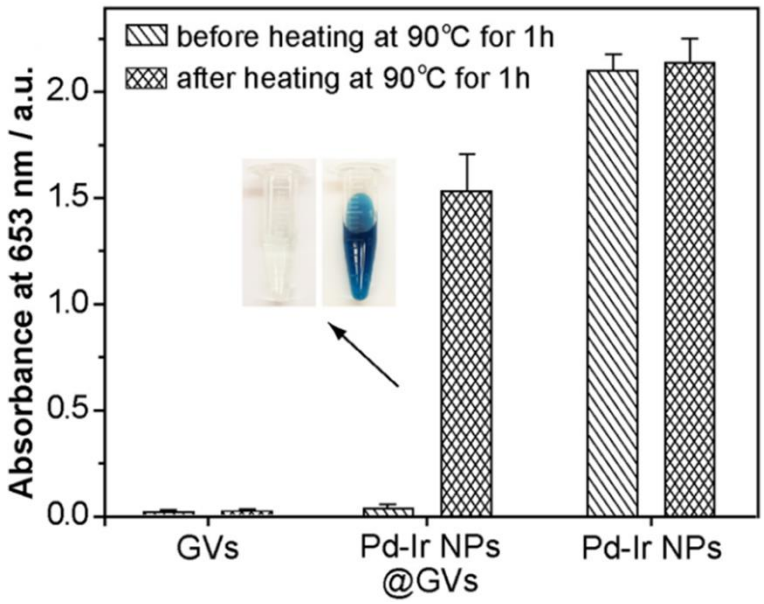

Figure 2.8 Absorbance at 653 nm measured from catalytic reaction solutions containing different particles (marked under the bars) at t = 2 min before and after heat treatment (90 °C, 1 h). Concentrations of GVs were kept the same for suspensions of GVs and Pd-Ir NPs@GVs, while the concentrations of Pd-Ir NPs were kept the same for suspensions of Pd-Ir NPs@GVs and Pd-Ir NPs. Inset shows photographs of reaction solutions corresponding to Pd-Ir NPs@GVs.

2.3.6 Immunoassay of disease biomarker

Finally, we applied the Pd-Ir NPs@GVs to ELISA of human prostate surface antigen (PSA), according to the principle shown in Figure 2.1. PSA was chosen because it has been recognized as the key biomarker responsible for prostate cancer recurrence in patients who have undergone radical prostatectomy.[136] It is vital to detect minute concentrations of PSA at the earliest stage possible to improve the survival rates of those patients.[137,138] Herein, antibodies were conjugated to Pd-Ir NPs@GVs through

the EDC/NHS-mediated coupling reaction between the –COOH groups of PAA_{23}-b-PS_{250}-SH on GVs and the $-NH_2$ groups on antibodies (Figure 2.2).[128] PSA standards with a series of concentrations in dilution buffer were monitored in a 96-well microtiter plate and quantified using a PerkinElmer Victor 3 1420 multilabel plate reader. The yellow color of the wells arose from the two-electron oxidation products of TMB (i.e., diimine with $\lambda_{max} \approx 450$ nm) that were formed when the catalytic reaction was quenched by H_2SO_4 (Figure 2.9a).[139] As shown in Figure 2.9b, a sigmoid curve regression between the logarithms of absorbance and PSA concentration was obtained. The linear range of detection was found to be 0.2-200 pg/mL with a linear regression value of $r^2 = 0.997$. The coefficient of variations (n = 8) across the entire concentration range were 2.15 − 12.24%, indicating a good reproducibility of the assay. The limit of detection (defined as the PSA concentration corresponding to a signal that is 3 times the standard deviation above zero calibrator)[140,141] was calculated to be 31 fg/mL. To evaluate the nonspecific binding between antibodies conjugated Pd-Ir NPs@GVs and the 96-well microtiter plate/capture antibodies, we have performed a control experiment by excluding antibodies conjugated Pd-Ir NPs@GVs from the blank well (i.e., 0 pg/mL PSA) while keeping all other conditions unchanged. The absorbance at 450 nm for the control group was measured to be 0.024, whereas the absorbance for the blank was 0.036 (both values of absorbance represent the averages from 8 independent measurements). Therefore, on average, the absorbance at 450 nm of each well caused by nonspecific binding of antibodies conjugated Pd—Ir NPs@GVs was approximately 0.012. This value is relatively low compared to the absorbance measured from the wells

of PSA standards, suggesting a good specificity of the antibodies conjugated Pd-Ir NPs@GVs.

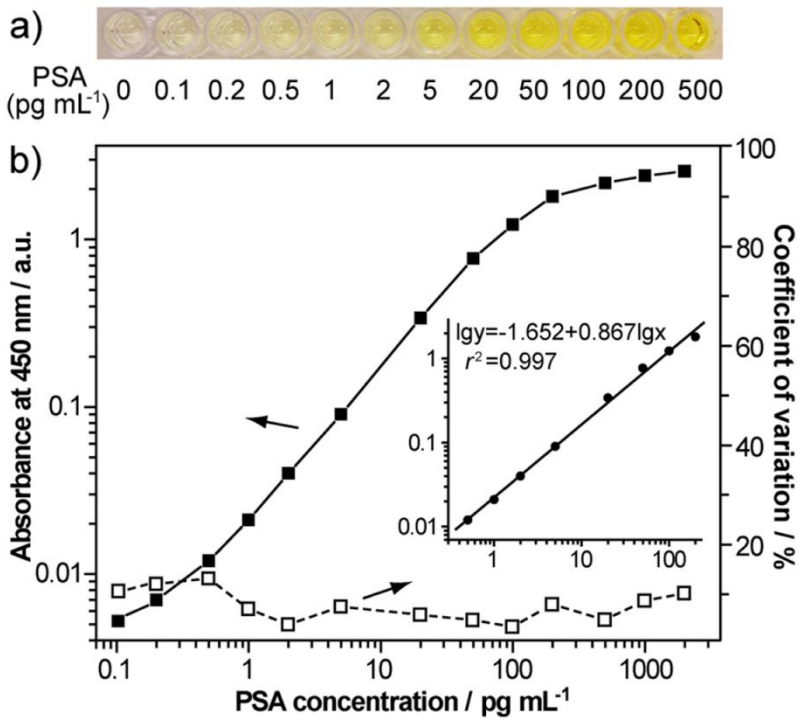

Figure 2.9 Pd-Ir NPs@GVs based ELISA of PSA. (a) Representative photographs taken from the ELISA of PSA standards; (b) Corresponding calibration curve (■) and imprecision profile (□) of the detection results shown in (a). Note that absorbance of the blank (i.e., 0 pg/mL PSA) was subtracted from those of PSA standards. Inset shows the linear range region of the calibration curve. All the data points represent the averages from 8 independent measurements.

We benchmarked the Pd-Ir NPs@GVs based ELISA against the conventional HRP based ELISA by using the same set of antibodies and procedures except for the exclusion of heat treatment. On the basis of the calibration curve shown in Figure 2.10,

the linear detection range and overall coefficient of variations for the HRP based ELISA were found to be 0.2-100 ng/mL and 4.21-14.31%, respectively. The limit of detection was determined to be 48 pg/mL, which was ~ 1500-fold higher than our enzyme-free ELISA. This significantly enhanced detection sensitivity for the enzyme-free ELISA could be attributed to the signal amplification by Pd-Ir NPs@GVs, because other conditions of both ELISAs were kept identical. We also evaluated the correlation between the enzyme-free ELISA with conventional HRP based ELISA by quantifying the same 12 PSA standards of concentrations in 0.5-50 ng/mL using the two ELISAs. For the quantification with enzyme-free ELISA, the standards were diluted with dilution buffer to ensure that the concentrations of PSA were located in the linear range. The final quantitative data was obtained based on the detected PSA concentrations and the dilution factors. As shown in Figure 2.11, a good correlation between the two ELISAs was found with a correlation coefficient $r = 0.998$ ($n = 12$). Taken together, these results demonstrate that our enzyme-free ELISA is three-orders-of-magnitude more sensitive than conventional ELISA, while its reliability and quantitativity are as good as those of conventional ELISA.

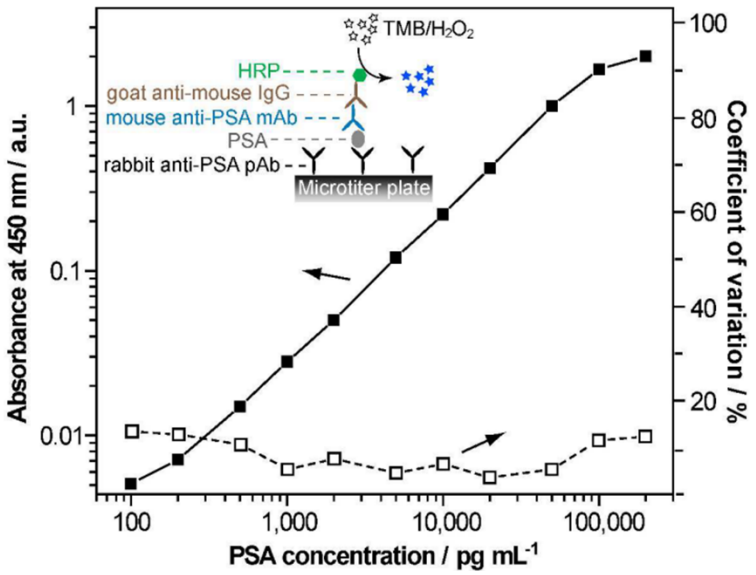

Figure 2.10 Calibration curve (■) and imprecision profile (□) of conventional HRP based colorimetric ELISA of PSA, in which PSA standards and antibodies were kept the same as what had been used for the Pd-Ir NPs@GVs based ELISA (Figure 2.14). Note that absorbance of the blank (i.e., 0 pg/mL PSA) was subtracted from those of PSA standards. Inset shows the detection principle.

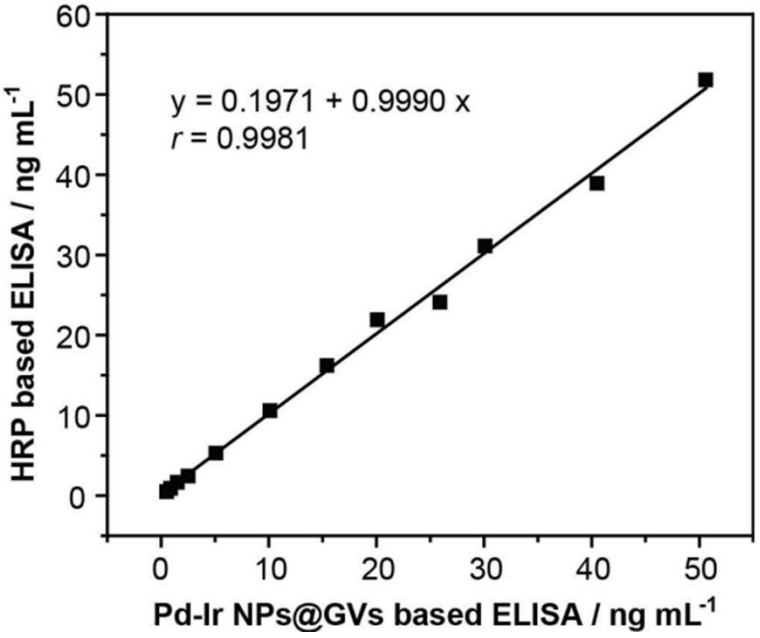

Figure 2.11 Correlation analysis between the Pd-Ir NPs@GVs based ELISA and HRP based ELISA in quantification of PSA from 12 standards. Each data point in the plot represents the average from three independent measurements.

2.4 Conclusions

We have demonstrated an enzyme-free signal amplification technique based on Pd-Ir NPs@GVs for colorimetric assay with substantially enhanced detection sensitivity. The enzyme-free technique we developed can be potentially extended to a variety of other enzymes-based diagnostic technologies beyond ELISA such as immunohis-tochemistry, Western blot, and point-of-care tests. Importantly, this technique is compatible with equipment and procedures of existing sensing technologies, making it practically useful for clinical diagnostics. Further optimization of the Pd-Ir NPs@GVs system (e.g., size of GV, loading amount of Pd-Ir NPs, particle release time, and catalytic efficiency) and detection of clinical samples are the subjects of our future research.

Chapter 3: A universal approach to assemble inorganic nanoparticles into hollow vesicles

Overview. In this work, a universal approach was developed to trigger the assembly of nanoparticles (NPs) by attaching amphiphilic block copolymers (BCPs) onto oleic acid or/and oleylamine capped NPs. Thiol-terminated BCPs were attached onto NPs via a one-step ultraviolet-induced thiol–ene reaction, where the double bond in OA (or OAm) and thiols in BCPs are coupled into thioether linkage through radical addition. We demonstrated that IONPs with various sizes (9.9 nm, 19.5 nm and 30.8 nm) and shapes (nanospheres and nanocubes) could be assembled into magnetic vesicles after the attachment of amphiphilic BCPs. Furthermore, inorganic nanoparticles with different compositions (Cu_9S_5, MnO and upconversion NPs) were used to fabricate hollow vesicles with potential biomedical applications by using this method.

A manuscript based on this chapter is in preparation and to be submitted to *Advanced Materials*

3.1 Introduction

Hollow, inorganic nanoscale vesicles (NVs) have emerged as a remarkable class of materials with potential applications in catalysis[142], biosensing[143], drug delivery[77] and energy storage[144], owing to their high surface area, large hollow volume and diverse hierarchical architectures and morphologies. Nowadays, one of the most common strategies for the generation of inorganic capsules is the templating synthesis

which involves multiple steps including the preparation of sacrificial templates, the deposition of desired materials onto the templates, and finally the removal of the templates by harsh chemical procedures.[145-148] Despite its wide application in fabrication, it has limitations such as tedious and costly procedures and inevitable collapse of the hollow structures during template removal.

Recently, amphiphilicity-driven self-assembly of "colloidal NPs" was proposed and explored as a simple and moderate route to achieve well-defined NVs. Inorganic nanoparticles tethered with BCPs are developed as a new class of building blocks for the fabrication of vesicular assemblies, in analogy to liposomes or polymersomes.[43,44,66,149] Thanks to the synergetic coupling between adjacent NPs in the assemblies, these hollow NVs exhibit enhanced physical/chemical properties while inheriting merits of the primary subunits. However, most of these assembly strategies are highly materials-specific and elaborately designed. The attachment of BCPs on NP surfaces strongly relies on the interactions between inorganic NPs and functional groups of BCPs. For instance, the grafting of BCPs on GNPs is based on the formation of Au-S bond, while IONPs are functionalized with BCPs via binding affinity between IONPs and dopamine-terminated BCPs.[44,50,66,149,150] Therefore, it is highly essential to explore novel and universal approaches for simple functionalization of NPs with BCPs and preparation of hollow vesicles with nanometer dimensions.

Herein, we report a simple and generalized approach for the attachment of BCPs onto inorganic NPs with various sizes, shapes or compositions, followed by the self-assembly of the BCP-tethered NPs into NVs. Hydrophobic inorganic NPs capped with oleic acid (OA) or oleylamine (OAm) could be attached with thiol-terminated BCPs

via a one-step ultraviolet-induced thiol–ene chemistry, where the double bond in OA (or OAm) and thiols in BCPs are coupled into thioether linkage through radical addition (Figure 3.1).[151,152] Driven by the colloidal amphiphilicity originated from the conformational rearrangement of grafted BCPs, BCP-NPs could self-assemble into well-defined NVs by elaborately tuning the relative sizes of NPs and BCPs. We demonstrated successful assembly of IONPs into NVs with potentially enhanced magnetization due to the coupling between adjacent subunits. Other inorganic nanoparticles such as Cu_9S_5, MnO and upconversion NPs could be also assembled into NVs by using this approach. This work provides a universal strategy for assembling OA or OAm-capped inorganic NPs into hollow NVs and opens up an avenue to extend the fabrication and applications of NVs with different subunits.

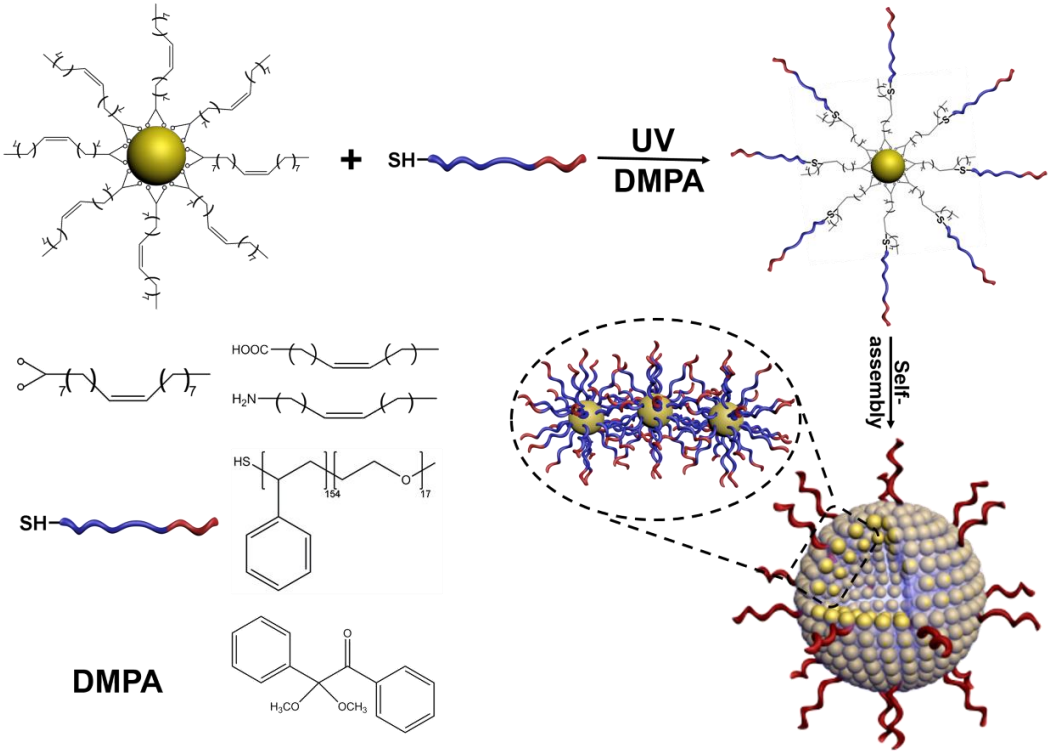

Figure 3.1 Schematic illustrating the attachment of BCPs onto OA or/and OAm capped NPs via an ultraviolet-induced thiol–ene reaction and assembly of the resultant BCP-tethered NPs into hollow vesicles

3.2 Experiments

3.2.1 Materials

Styrene, 4-cyano-4-(phenylcarbono-thioylthio) pentanoic acid (CPPA), ethanol (99.5%), dioxane (99.8%), tetrahydrofuran (THF, 99.9%), methanol (99.9%), n-butylamine, N-(3-(dimethylamino)propyl)-N'-ethyl-carbodiimide hydrochloride (98%, EDC), N-hydroxysuccinimide (98%, NHS), oleic acid (99%), oleylamine (98%), hexane (95%), 1-octadecene (90%), 1-hexadecene (98.5%), trioctylamine (98%), copper (II) chloride dehydrate, sodium diethyldithiocarbamate trihydrate, manganese chloride tetrahydrate, sodium hydroxide (98%), ammonium fluoride, yttrium (III) chloride hexahydrate, ytterbium (III) chloride hexahydrate and erbium (III) chloride hexahydrate were purchased from Sigma-Aldrich. Azobis(isobutyronitrile) (AIBN) was recrystallized from ethanol. Deionized water (Millipore Milli-Q grade) with resistivity of 18.0 MΩ was used in all the self-assembly experiments.

3.2.2 Synthesis of Thiol-Terminated BCPs

Thiol-terminated BCPs of HS-PS-*b*-PEO were synthesized by the reversible addition−fragmentation chain transfer (RAFT) polymerization as reported previously.[66] Using HS-PS_{98}-*b*-PEO_{17} as an example, styrene, chain transfer agent

(PEO-CTA), and AIBN were dissolved in dioxane with a molar ratio of 150:1:0.2. The solution was filled with nitrogen and then put into a preheated oil bath at 85 °C for 20 h. The product was precipitated in hexane and dissolved in THF to remove unreacted monomers and impurities. Molecular weight of the BCPs characterized by ^{1}H NMR was 11.0 kg/mol, by comparing the integrals of the resonance peaks of aromatic ring of PS block (6.4 − 7.3 ppm) and the methylene groups of PEO-CTA (3.65 ppm) (Figure 3.2b).The CTA-PS_{98}-*b*-PEO_{17} was dissolved in THF with excess of n-butylamine under nitrogen for 4 h to convert CPPA into thiol groups. The resulting HS-PS_{98}-*b*-PEO_{17} was obtained by precipitation in hexane twice and dried under vacuum for 24 h.

3.2.3 Synthesis of Oleic Acid and/or Oleylamine-capped Nanocrystals

Hydrophobic IONPs with various sizes were prepared via thermal decomposition of iron oleate complex by using oleic acid as the stabilizing agent.[153] Briefly, iron oleate complex (3.6 g, 4 mmol) and oleic acid (0.57 g, 2 mmol) were dissolved in 1-octadecene (20 g) at room temperature. The mixture was heated to 300 °C with a constant heating rate and then kept at this temperature for 30 min. The resulting solution containing IONPs (19.45±0.73 nm) was then cooled to room temperature and washed with ethanol three times. The precipitated IONPs were dispersed in THF to form a stable colloidal solution with a concentration of 5 mg mL^{-1}. By switching 1-octadecene into 1-hexadecene and trioctylamine, OA-capped IONPs of 9.85±0.48 nm and 30.81±2.03 nm were prepared respectively, due to the change of solvent boiling point. For the synthesis of iron oxide nanocubes, identical procedures were applied except

that a mixture of oleic acid (0.28g, 1mmol) and sodium oleate (0.30g, 1mmol) were added before thermal decomposition of iron oleate complex.

OAm-capped Cu_9S_5 NPs were prepared by a modified thermal decomposition process.[154] Copper diethyldithiocarbamate [$Cu(DEDTC)_2$] precursor was prepared by reacting $CuCl_2 \cdot 2H_2O$ with sodium diethyldithiocarbamate (SDEDTC) as follows: A solution of SDEDTC (10 mmol) in distilled water (5 mL) was added into another solution containing $CuCl_2$ (10 mmol) and distilled water (10 mL) under magnetic stirring for 1h, forming a dark brown turbid solution. Subsequently, the dark brown $Cu(DEDTC)_2$ precursor was obtained by filtration and dried at room temperature under vacuum before use. For the synthesis of OAm-capped Cu_9S_5 NPs, 15 mL of OAm was slowly heated to 300 °C in a flask under magnetic stirring and N_2 for 30 min to remove residual water and oxygen, followed by the injection of 5 mL OAm containing 1 mmol $Cu(DEDTC)_2$. The resulting solution became dark green immediately and the reaction was kept at 300 °C for 10 min and then cooled to 60 °C naturally. The resulting solution was washed with ethanol three times and the precipitated Cu_9S_5 NPs were collected by centrifugation and dispersed in THF to form a stable colloidal solution with a concentration of 5 mg mL^{-1}.

OA-capped MnO NPs were prepared via thermal decomposition of manganese oleate precursor.[155] Manganese oleate complex was prepared according to a reported procedure: 7.94 g (40 mmol) of manganese chloride tetrahydrate and 22.60 g (80 mmol) oleic acid were dissolved in 200 mL of methanol. A solution of 3.2 g (80 mmol) of sodium hydroxide in 200 mL of methanol was added dropwise into the Mn-/oleic acid solution under stirring for 1 h. The initially clear colorless mixture turned pink,

followed by the precipitation of a deep red oily substance. After stirred for another hour, the solvent was discarded and the precipitates were washed with water, ethanol, and acetone. The oily residue was dissolved in hexane and dried over $MgSO_4$. After evaporating the solvent, the product was dried in vacuum at 150 °C for 2 h to produce a deep red waxy manganese oleate complex. For the synthesis of OA-capped MnO NPs, 1.24 g (2 mmol) of the manganese oleate precursor was dissolved in 10 g 1-octadecene and degassed at 70 °C in vacuum for 2 h. The solution was intermittently backfilled with argon to remove any moisture and oxygen. The reaction mixture was subsequently rapidly heated to 200 °C with approximately 5 °C/min, followed by another heating process of 1.5 °C/min until boiling. The temperature was held at reflux (315 °C) for 1 h and the as-prepared nanocrystals were washed with ethanol three times by centrifugation. MnO NPs were collected and dispersed in THF to form a stable colloidal solution with a concentration of 5 mg mL^{-1}.

OA-capped $NaYF_4$:Yb,Er nanoparticles were synthesized following a reported approach.[156] Typically, 0.78 mmol $YCl_3 \cdot 6H_2O$, 0.2 mmol $YbCl_3 \cdot 6H_2O$ and 0.02 mmol $ErCl_3 \cdot 6H_2O$ were added into a mixture of 6 mL OA and 15 mL 1-octadecene in a three-necked flask. The solution was heated to 160 °C for 20 min under argon atmosphere to form a transparent solution and then cooled down to room temperature. Subsequently, 10 mL methanol solution containing 100 mg NaOH and 148 mg NH_4F was added dropwise into the solution and the mixture was heated slowly to 70 °C under stirring for 30 minutes to remove the methanol solvent completely. After the evaporation of methanol, the solution was slowly heated to 300 °C and maintained for 1.5 hours under argon atmosphere. After cooled down to room temperature, the resultant mixture was

washed with ethanol three times and purified by centrifugation. The as-synthesized product of $NaYF_4$: 20%Yb, 2%Er UCNPs were dispersed in THF with a concentration of 5 mg mL^{-1}.

3.2.4 Synthesis of BCP-tethered NPs

Thiol-terminated BCPs were attached onto OA and/or OAm capped NPs via an ultraviolet-induced thiol–ene reaction. Using IONPs as a model system, 50mg HS-PS_{98}-*b*-PEO_{17} was added into 2 mL of OA-capped IONPs dispersion in THF (30.8 ± 2.0 nm 5mg mL^{-1}), followed by the addition of 100 µL THF solution of DMPA (10 mg/mL). The mixture solution was transferred into a sealed quartz beaker and irradiated with UV-light (1000 W, 365 nm wavelength) for 60 min in an ice bath under magnetic stirring. After completion of UV irradiation, the BCP-tethered IONPs were washed with THF for 6 times, collected by centrifugation (12000 rpm/min, 15min) and re-dispersed in THF with a concentration of 0.2 mg mL^{-1}. To verify successful attachment of BCPs onto various inorganic NPs, the hydrodynamic diameter of NPs in THF before and after BCPs attachment was measured using a PHOTOCOR-FC light scattering instrument with a 5 mW laser of 633 nm at a scattering angle 90°. ^{1}H NMR spectra of the NPs and BCP-NPs were also analyzed and compared to confirm the conjugation of BCPs onto corresponding NPs. TGA was performed to estimate grafting density of BCPs on various NPs. Briefly, the sample (5 mg) was dried and loaded into a platinum pan which was heated to 700 ° C at a constant heating rate of 25 °C min^{-1} under argon. The BCPs grafting density (σ) was calculated using the formula:[157]

$$\sigma = \frac{f * N_A * \rho * d}{6 * M_n * (1 - f)}$$

Here *f* refers to the weight fraction of the organic ligands determined by TGA analysis; N_A is the Avogadro constant; ρ is the bulk density of the corresponding NPs; d is the average diameter of BCP-NPs, and M_n is the number-average molecular weight of the PEO-*b*-PS. It is assumed that the density of the BCP-NPs is identical to the density of the bulk material and no free polymer is present.

3.2.5 Self-Assembly of BCP-tethered NPs into NVs

BCP-tethered inorganic NPs were assembled into NVs by film rehydration method. As a prototype system, 500 μL THF solution of BCP-IONPs (0.2 mg mL^{-1}) was dried on a glass substrate under N_2 stream to form a thin film, followed by rehydration in water under sonication for 30 s. The as-prepared NVs were collected by centrifugation (3000 rpm/min, 15min) and re-dispersed in ultrapure water for further utilization.

3.2.6 Characterizations of NVs

The assembled NVs were imaged using a Hitachi SU-70 Schottky field emission gun Scanning Electron Microscope (FEG-SEM) and a JEOL FEG Transmission Electron Microscope (FEG-TEM). Energy dispersive X-ray (EDS) mapping and corresponding spectra of the NVs were acquired using a JEOL JEM-2100 LaB6 Transmission Electron Microscope. Samples for SEM observations were prepared by dropping 5-10 μL of sample solution onto silicon wafers and dried at room temperature.

TEM samples were prepared by dropping 5-10 μL of sample solution on 300 mesh copper grids covered with carbon film and dried at room temperature.

3.3 Results and discussion

3.3.1 Synthesis and Characterization of BCP-tethered IONPs

OA-capped hydrophobic IONPs with a diameter of 30.8 ± 2.0 nm were synthesized by a thermal decomposition method reported previously and used as a prototype NP for surface modification and self-assembly (Figure 3.2a).[153] Thiol terminated PS_{98}-*b*-PEO_{17} (11.0 kg/mol) was synthesized using reversible addition-fragmentation chain-transfer (RAFT) polymerization and grafted onto the surface of IONPs via ultraviolet-induced thiol–ene chemistry to obtain amphiphilic building blocks (Figure 3.2b). The BCPs-tethered IONPs (BCP-IONPs) remained well dispersed in THF, as confirmed by the slightly increased hydrodynamic diameter from 36.4±12.4 nm to 85.9±22.8 nm after treatment, owing to the BCPs layer grafting on the surface of IONPs (Figure 3.3a). The average grafting density (σ) of BCPs is estimated to be 0.08 chains/nm^2 based on thermogravimetric analysis, corresponding to ~226 chains per 30 nm IONP (Figure 3.3b).

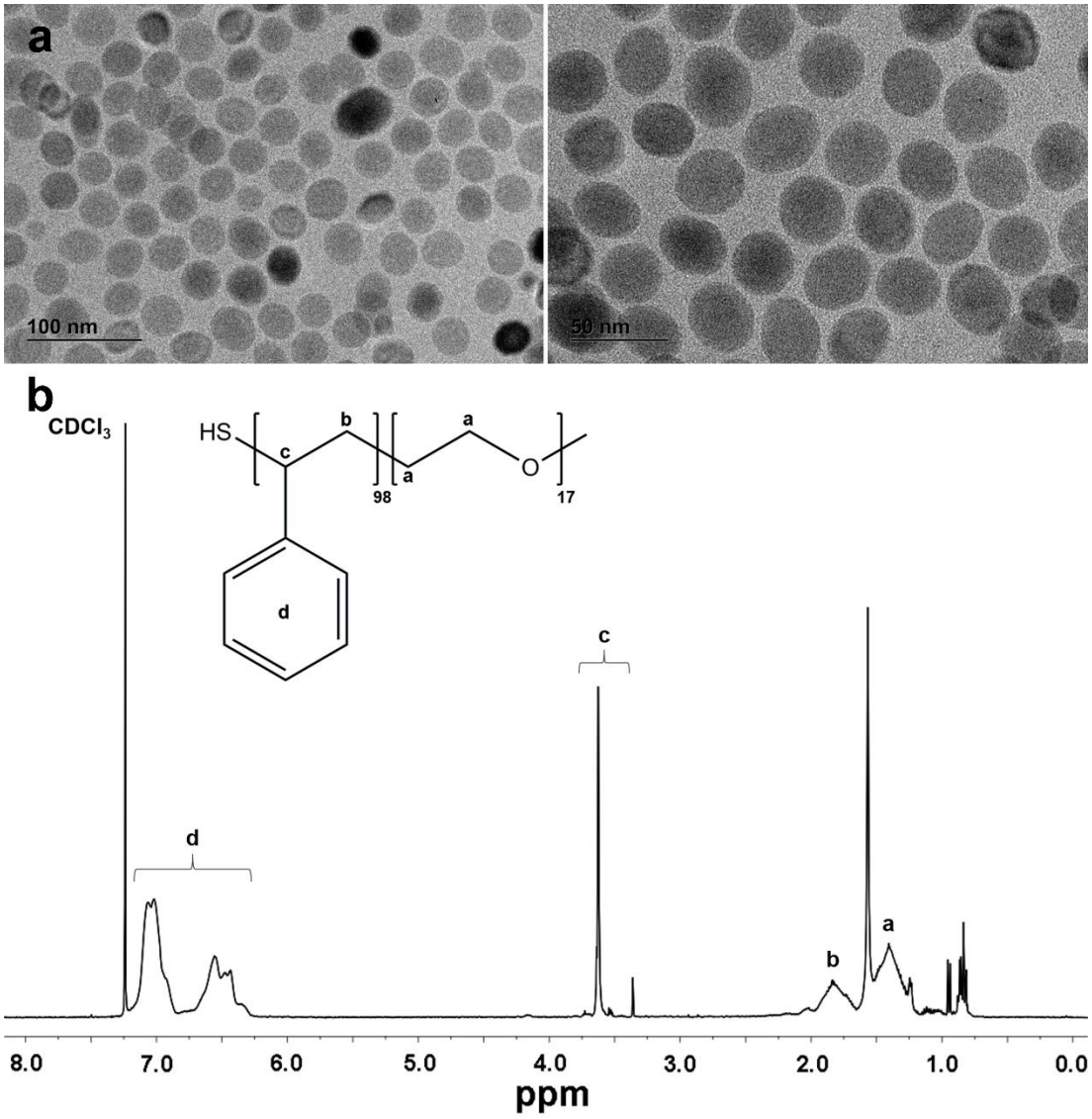

Figure 3.2 (a) TEM images of OA-capped 30 nm SPIONs and (b) ^{1}H NMR spectrum of PEO_{17}-*b*-PS_{98}

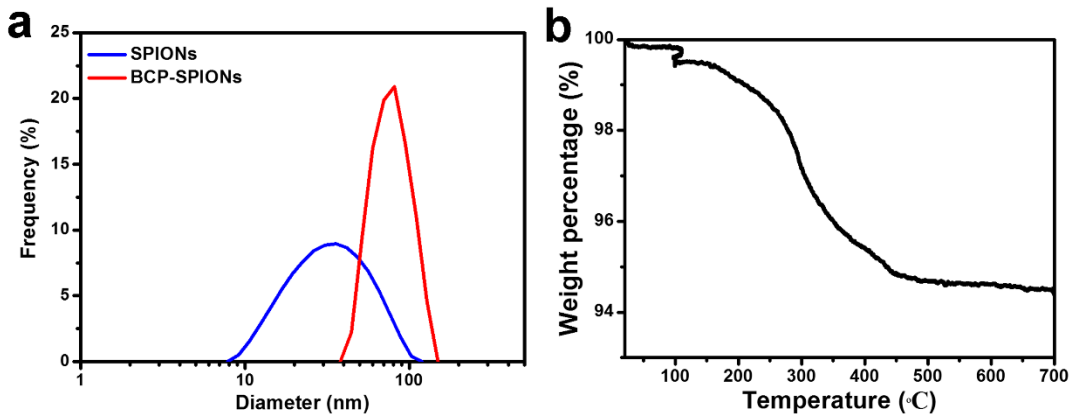

Figure 3.3 (a) DLS diameter of IONPs before and after the attachment of BCPs and (b) TGA analysis of BCP-IONPs.

3.3.2 Synthesis and Characterization of NVs assembled from BCP-tethered IONPs

Assemblies of IONPs were fabricated by rehydrating a film of BCP-IONPs in ultrapure water and the formation of vesicular structures can be attributed to the conformation change of BCP tethers on NP surface, as we reported previously.[44] Scanning and transmission electron microscope (SEM/TEM) images in Figure 3.4a, b show that the resulting NVs were composed of multilayers of densely packed IONPs in the vesicular membranes. The hollow interior and multilayers of IONPs in the membrane can be clearly seen from NVs with occasionally broken membrane (inset in Figure 3.4a). The average diameter of the MuMVs was estimated to be 679.2 ± 53.8 nm by TEM analysis (Figure 3.4c). The composition of NVs was further confirmed by EDS element mapping, where strong Fe and O signals were observed, indicating that the NVs were assembled from BCP-IONPs (Figure 3.4d).

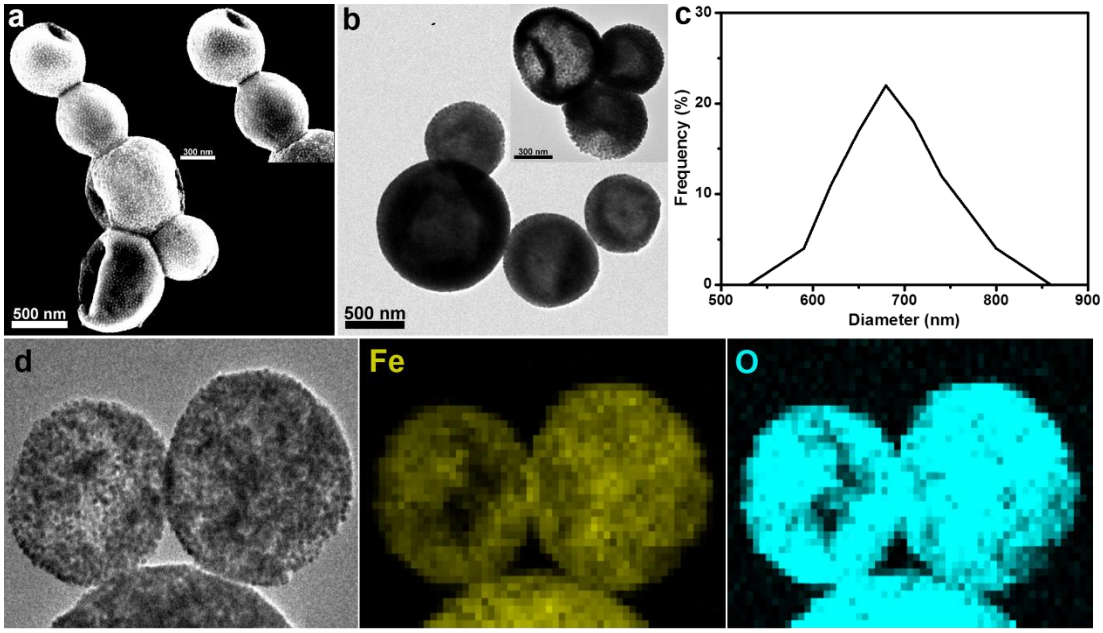

Figure 3.4 (a) SEM and (b) TEM images of magnetic vesicles assembled from PEO-PS-OA-SPIONs; (c) Size distribution of magnetic vesicles from TEM analysis; (d) EDS mapping of magnetic vesicles showing the element of Fe and O

3.3.3 Influence of BCPs length and NPs size on the vesicle formation

Similar to the assembly of BCP-GNPs, the self-assembly of BCP-IONPs is strongly dependent on the hydrophilic/hydrophobic balance of the building blocks. To investigate the factors influencing the assembly morphologies, IONPs of various sizes and BCPs with different length of PS (at fixed length of PEO_{17}) were synthesized and used to produce building blocks of NVs (Figure 3.5). With the increase of MW of BCP tethers from 6.2 k to 14.5 k, the assembly morphologies transited from clusters to vesicles and eventually to random aggregates for BCP-IONPs of all sizes due to an increase in overall hydrophobicity (Figure 3.6). Meanwhile, at fixed MW of BCP (e.g., 9.6K), morphological transition of self-assemblies from vesicles to clusters was

observed when the size of IONPs increased. This is mainly attributed to the decreased graft density of BCPs associated with a decreased curvature for larger IONPs. NVs composed of BCP-tethered iron oxide nanocubes were also fabricated using the same strategy, indicating this assembly-based approach is applicable to IONPs with various sizes and shapes (Figure 3.7).

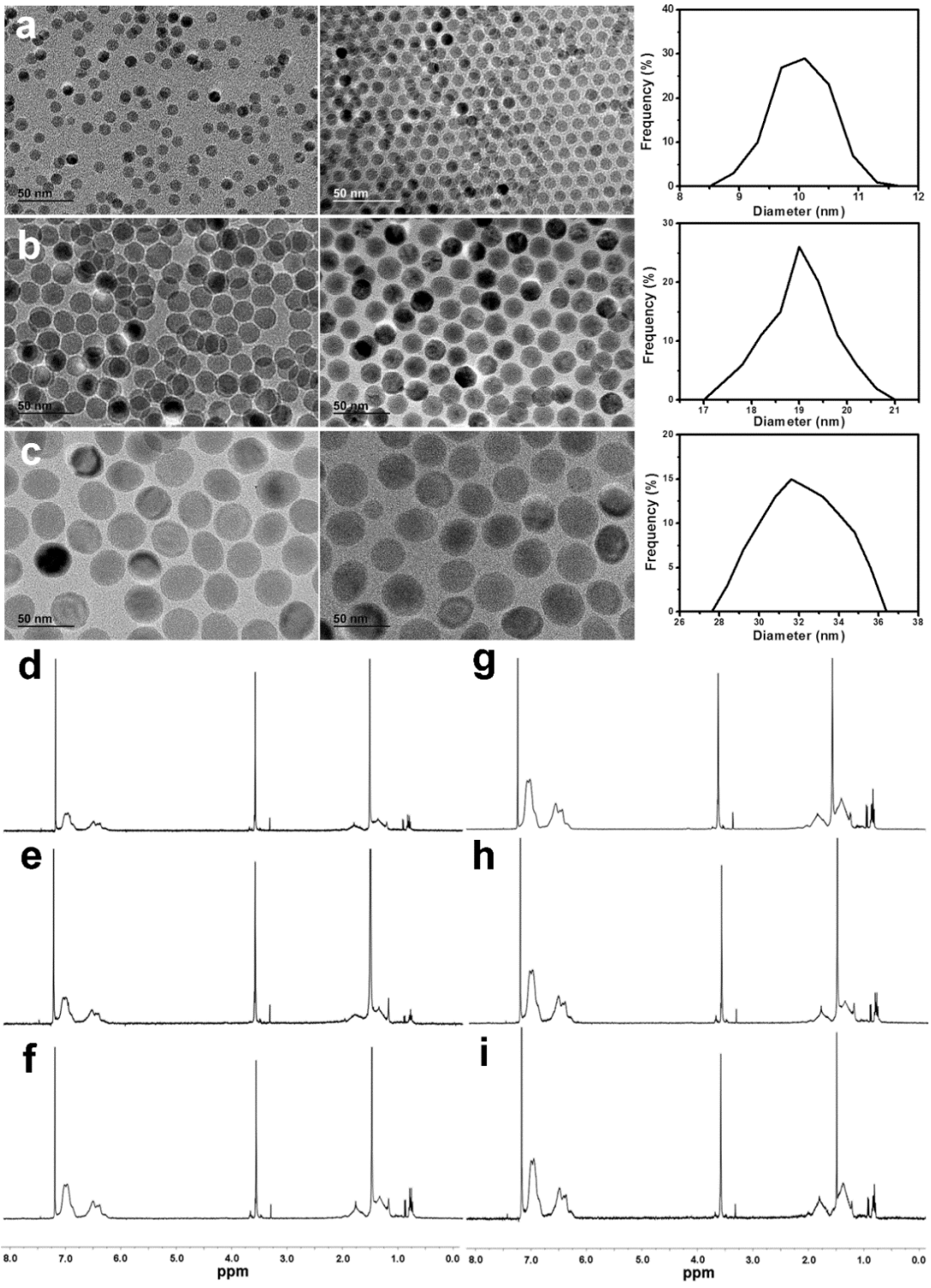

Figure 3.5 (a-c) TEM and size analysis of IONPs with various diameter of (a) 9.85±0.48 nm, (b) 19.45±0.73 nm and (c) 30.81±2.03 nm. (d-i) ^{1}H NMR spectrum of

BCPs: (d) PEO_{17}-*b*-PS_{52}, (e) PEO_{17}-*b*-PS_{70}, (f) PEO_{17}-*b*-PS_{85}, (g) PEO_{17}-*b*-PS_{98},(h) PEO_{17}-*b*-PS_{111} and (i) PEO_{17}-*b*-PS_{132}

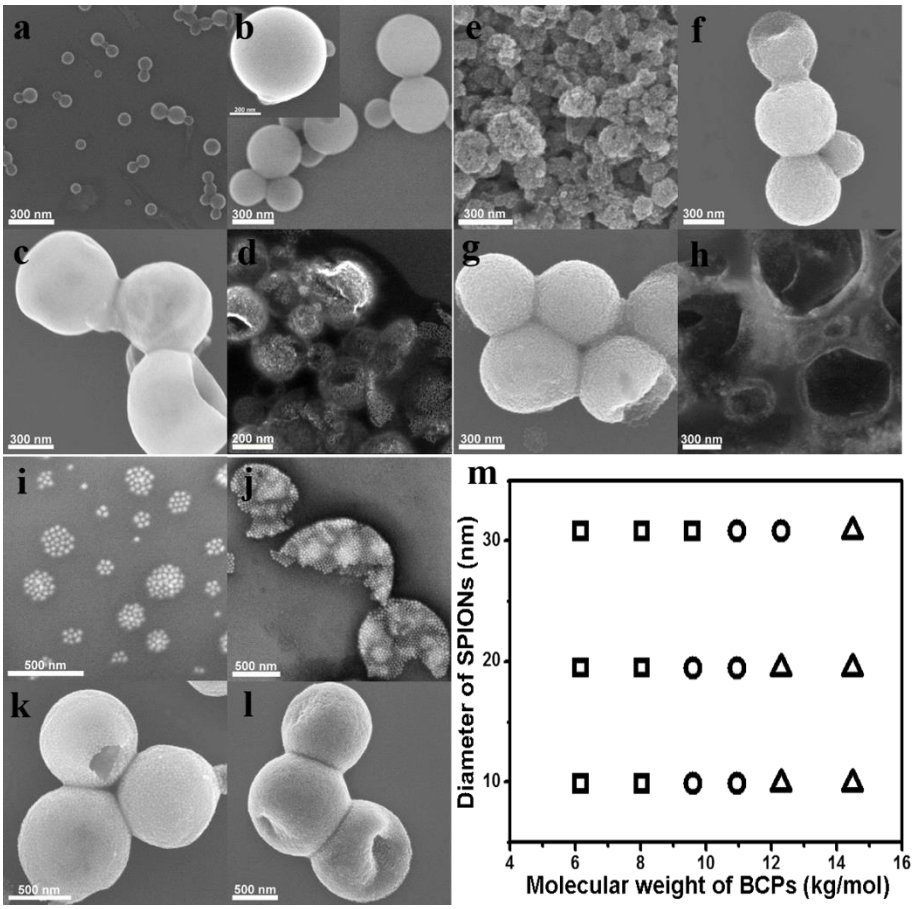

Figure 3.6 SEM images of vesicular assemblies from BCP-tethered IONPs with different diameters: (a-d) 10 nm, (e-h) 19 nm, and (i-l) 31 nm. BCPs with different lengths used here are: (a,e,i) PEO_{17}-*b*-PS_{70}, (b,f,j) PEO_{17}-*b*-PS_{85}, (c,g,k) PEO_{17}-*b*-PS_{98} and (d,h,l) PEO_{17}-*b*-PS_{111}. (m) The product diagram for the self-assembly of BCP-IONPs with varying diameter of IONPs and molecular weight of PEO_{17}-*b*-PS_x. (□) clusters, (○) vesicles, (Δ) random aggregates.

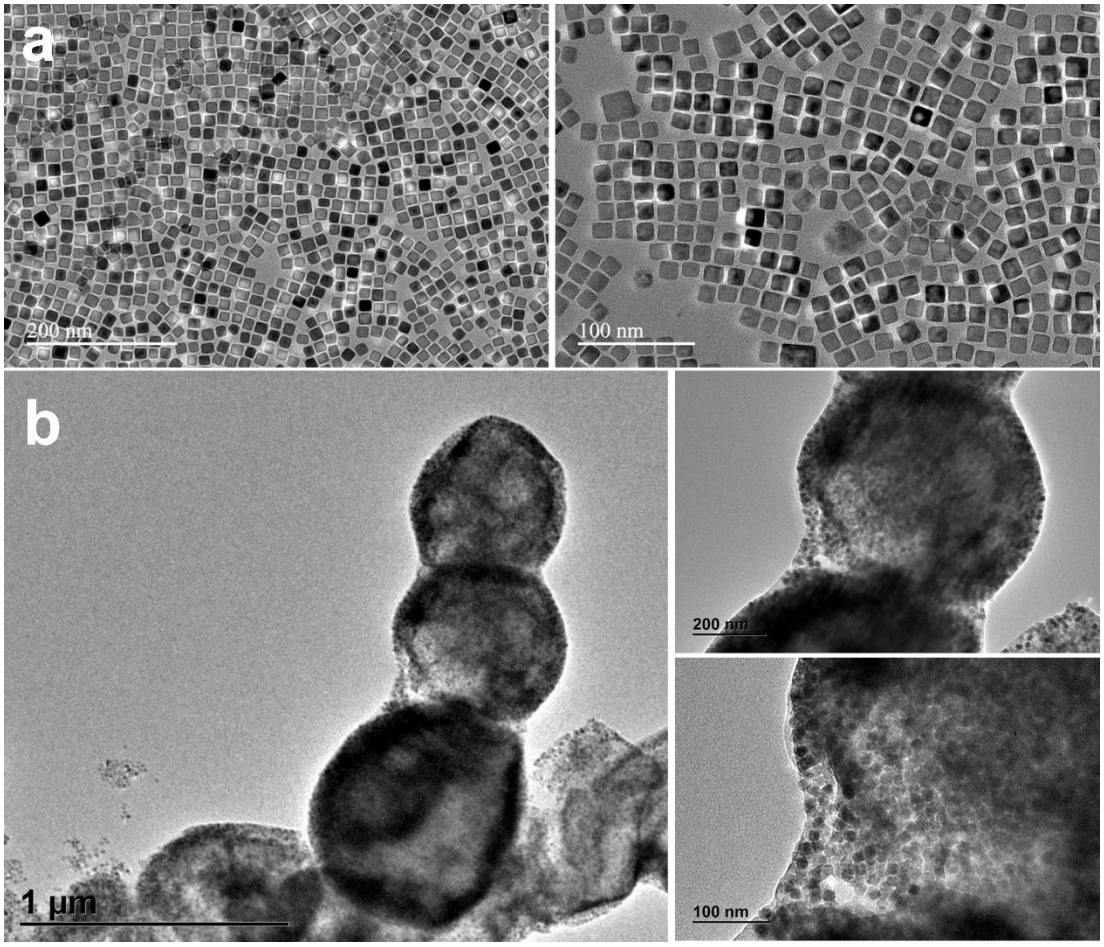

Figure 3.7 TEM images of (a) Fe_3O_4 nanocubes and (b) vesicles assembled from PEO-PS-OA-capped Fe_3O_4 nanocubes.

3.3.4 Self-assembly of BCP-tethered NPs with various compositions

We demonstrated that this assembly-based approach is applicable to colloidal NPs with different compositions, surface ligands and morphologies. Three other hydrophobic NPs including OAm-capped Cu_9S_5 (Figure 3.8a 19.7 ± 4.4 nm), OA-capped MnO (Figure 3.8b 27.2 ± 8.7 nm) and OA-capped upconversion NPs (NaYF4:Yb^{3+}, Er^{3+} Figure 3.8c 44.0 ± 6.5 nm) were prepared and used for assembly.[154-156] Successful attachment of BCPs was confirmed by DLS analysis with analog

characteristics as BCP-IONPs (Figure 3.9a). The average grafting density (σ) of BCPs is estimated to be 0.10 (MnO NPs), 0.09 (CuS NPs) and 0.08 (UCNPs) chains/nm^2 according to the thermogravimetric analysis (Figure 3.9b). NVs composed of the corresponding NPs were observed by both SEM and TEM which clearly revealed the hollow interior of the assemblies with the occasionally broken membrane (Figure 3.10a-l). The composition of NVs was verified by EDS element mapping, which confirmed that the NVs were assembled from the corresponding BCP-tethered NPs (Figure 3.10m-o).

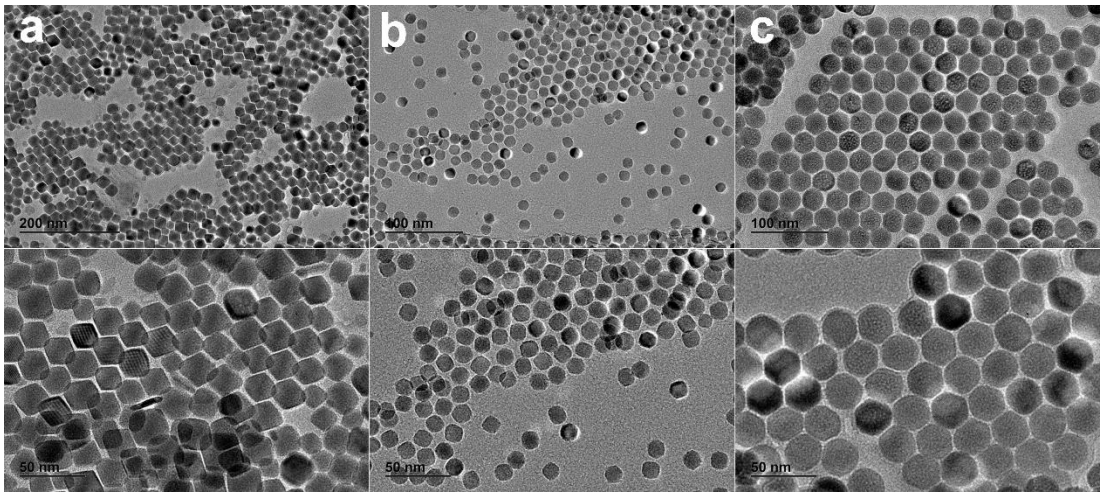

Figure 3.8 TEM images of (a) OAm-capped Cu_9S_5 NPs, (b) OA-capped MnO NPs and (c) OA-capped upconversion NPs

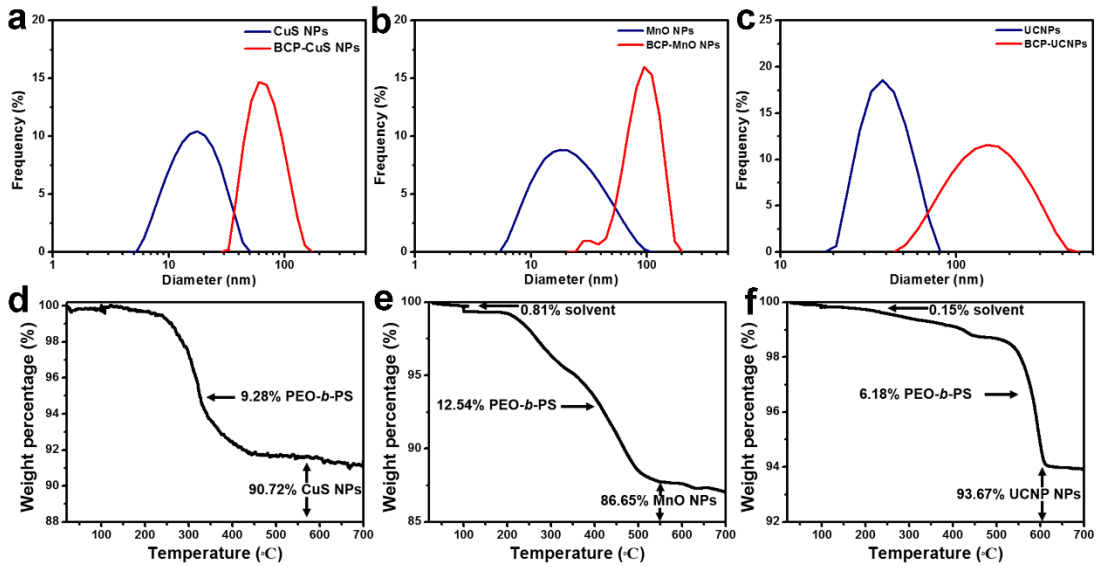

Figure 3.9 (a-c) DLS diameter of (a) Cu_9S_5 NPs, (b) MnO NPs and (c) UCNPs before and after the attachment of BCPs. (d-f) TGA analysis of (d) BCP-Cu_9S_5 NPs (e) BCP-MnO NPs and (f) BCP-UCNPs.

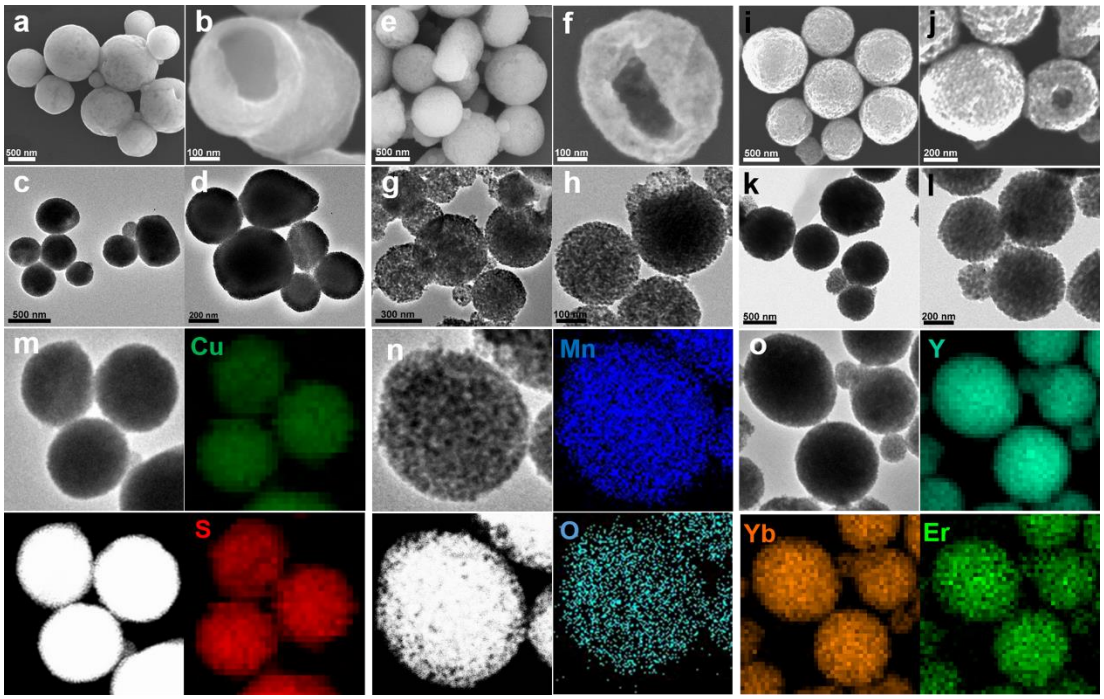

Figure 3.10 (a,b) SEM and (c,d) TEM images of vesicles assembled from PEO-PS-OAm-Cu_9S_5 NPs; (e,f) SEM and (g,h) TEM images of vesicles assembled from PEO-PS-OA-MnO NPs; (i,j) SEM and (k,l) TEM images of vesicles assembled from PEO-PS-OA-UCNPs; (m-o) EDS mapping of (m) Cu_9S_5 vesicles showing the element of Cu and S; (n) MnO vesicles showing the element of Mn and O and (o) UCNP vesicles showing the element of Y, Yb and Er.

3.4 Conclusions

In summary, we have developed a universal strategy to attach BCPs onto inorganic NPs to produce colloidal amphiphiles for self-assembly. Thiol-terminated BCPs were conjugated with OA or/and OAm on NP surface via an ultraviolet-induced thiol–ene reaction, followed by the self-assembly of BCP-NPs into well-defined hollow vesicles. By using this approach, NPs of various sizes, shapes and compositions were assembled into vesicles respectively, which may find a range of applications in such as bioimaging, drug delivery and energy storage.

Chapter 4: Cooperative Assembly of Magneto-nanovesicles with Tunable Wall Thickness and Permeability for MRI-guided Drug Delivery

Overview. Although various approaches have been developed for the fabrication of vesicles with inorganic NPs as building blocks, a lack of control over assembly structures and properties significantly limits their further applications. Here we describes the fabrication of nanosized magneto-vesicles (MVs) comprising tunable layers of densely packed superparamagnetic iron oxide nanoparticles (SPIONs) in membranes via cooperative assembly of polymer-tethered SPIONs and free poly(styrene)-*b*-poly(acrylic acid) (PS-*b*-PAA). The membrane thickness of MVs could be well controlled from 9.8 to 93.2 nm by varying the weight ratio of PS-*b*-PAA to SPIONs. The increase in membrane thickness was accompanied by the transition from monolayer MVs, to double-layered MVs and to multilayered MVs (MuMVs). This can be attributed to the variation in the hydrophobic/hydrophilic balance of polymer-grafted SPIONs upon the insertion and binding of PS-b-PAA onto the surface of nanoparticles. Therapeutic agents can be efficiently encapsulated in the hollow cavity of MVs and the release of payload can be tuned by varying the membrane thickness of nanovesicles. Due to the high packing density of SPIONs, the MuMVs showed the highest magnetization and transverse relaxivity rate (r_2) in magnetic resonance imaging (MRI) among these MVs and individual SPIONs. Upon intravenous injection, doxorubicin-loaded MuMVs conjugated with RGD peptides could be

effectively enriched at tumor sites due to synergetic effect of magnetic and active targeting. As a result, they exhibited drastically enhanced signal in MRI, improved tumor delivery efficiency of drugs as well as enhanced antitumor efficacy, compared with groups with only magnetic or active targeting strategy. The unique nanoplatform may find applications in effective disease control by delivering imaging and therapy to organs/tissues that are not readily accessible by conventional delivery vehicles.

This chapter is adapted from the manuscript published in the following article: Yang, K., Liu, Y., Liu, Y., Zhang, Q., Kong, C., Yi, C., Zhou, Z., Wang, Z., Zhang, G., Zhang, Y., Khashab, N., Chen, X. and Nie, Z., Cooperative Assembly of Magneto-Nanovesicles with Tunable Wall Thickness and Permeability for MRI-Guided Drug Delivery, *J. Am. Chem. Soc.*, **2018**, 140, 4666−4677

4.1 Introduction

Superparamagnetic iron oxide nanoparticles (SPIONs) have been widely explored for biomedical applications, such as biosensing,[158] immunoassay,[159] cell separation,[160] and cancer imaging and therapy,[161-165] due to their unique size, biocompatibility, biostability, and responsiveness to magnetic field.[166-169] For instance, SPIONs can serve as negative magnetic resonance imaging (MRI) contrast agents, as they can shorten the transverse relaxation time (T_2) of water protons, resulting in a hypointense signal in T_2-weighted MRI.[78] The magnetic movement of SPION-based nanocarriers can be used to guide the delivery of therapeutic agents specifically to diseased areas to achieve optimal therapy outcomes. However, small SPIONs inherently possess a relatively low magnetization per particle, making it difficult to readily manipulate their movement in relatively deep tissues.[170] Increasing the size of iron oxide nanoparticles

(NPs) (e.g., above ~ 26 nm) leads to a higher magnetic moment, but at the expense of inducing a superparamagnetic/ferromagnetic transition and hence possible colloidal instability of NPs.[171] One promising strategy of resolving this issue is to assemble SPIONs into larger ensembles and utilize the magnetic properties of a collection of NPs for medical imaging and targeted delivery.[32,36,37,99,172-174]

Nanosized vesicles (e.g., liposomes or polymersomes) are particularly attractive and have made the greatest clinical impact, because of their unique ability to encapsulate and deliver hydrophilic and/or hydrophobic compounds simultaneously.[175-178] Incorporating SPIONs into organic vesicular membranes can impart the system with magneto-responsiveness in order to develop highly selective and effective therapeutics and diagnostics.[179-182] One commonly used strategy for the fabrication of SPION-embedded nanovesicles is to coassemble hydrophobic small molecular ligand-covered SPIONs with amphiphilic lipids or block copolymers (BCPs).[183-186] During the assembly, SPIONs are inserted into the hydrophobic domains (e.g., center of lipid bilayers) of vesicular membranes through hydrophobic interaction between capping agents and hydrophobic segments of lipids or BCPs. Small NPs (<8 nm) are usually used in the fabrication, in order to avoid possible insertion-induced morphological change or hole formation of vesicles. More recently, the assembly of BCP-tethered NPs has provided an effective route to the fabrication of hybrid vesicles with high density and much broader size range of NPs in the membrane.[43,44,66] These hybrid vesicles have been demonstrated for enhancing MRI and photoacoustic imaging, as well as efficacy in photothermal/photodynamic therapy due to their collective properties of assembled NPs.[76,77] As the magnetization and MRI contrast are strongly

dependent on the content and organization of SPIONs in individual ensembles, it is expected that vesicles with thicker SPIONs-bearing membrane could demonstrate higher imaging contrast and magnetization for better *in vivo* imaging and drug delivery. Nevertheless, there remains challenging in the fabrication of hybrid vesicles with tunable layers of NPs in the membranes.

Here we report the design of magneto-vesicles (MVs) composed of tunable layers of densely packed SPIONs via cooperative assembly of polystyrene-b-poly(ethylene oxide) (PS-b-PEO)-tethered SPIONs and free poly(styrene)-block-poly(acrylic acid) (PS-b-PAA) (Figure 4.1a). The membrane thickness of MVs can be controlled from 9.8 to 93.2 nm by varying the weight ratio of PS-b-PAA to SPIONs, which is accompanied by the transition from monolayer MVs (MoMVs), to double-layered MVs (DoMVs) and to multilayered MVs (MuMVs). The formation of MVs with controlled layers of SPIONs is attributed to the modulation of the surface property of SPION building blocks through the binding interaction between carboxyl groups of PS-b-PAA and SPIONs. Compared with individual SPIONs, MVs with a thicker membrane exhibit a much higher magnetization for magnetic manipulation as a result of larger amounts of SPIONs in each vesicle. Moreover, as the membrane thickness of MVs increases, a higher magnetization leads to a drastically enhanced transverse relaxivity rate (r_2) value in MRI due to the higher density of SPIONs. Therapeutic agents such as doxorubicin (Dox) can be efficiently encapsulated in the hollow cavity of MVs during the assembly process and the release of payload can be tuned by varying the membrane thickness of the MVs. Upon intravenous injection into athymic nude mice implanted with U87MG human malignant glioblastoma cells, the RGD-conjugated Dox-loaded

MuMVs (RGD-Dox-MuMVs) exhibited significantly enhanced tumor accumulation via synergistic magnetic field-enhanced targeting and RGD-mediated active targeting of tumors (Figure 4.1b). As a result, RGD-Dox-MuMVs with a magnetic field showed over 10-fold increase in the delivery of Dox in tumors and drastically enhanced tumor inhibition, compared with control groups without RGD and magnetic field. We expect that the unique nanoplatform may find applications in effective disease control by delivering imaging and therapy to organs/tissues that are not readily accessible by conventional delivery vehicles.

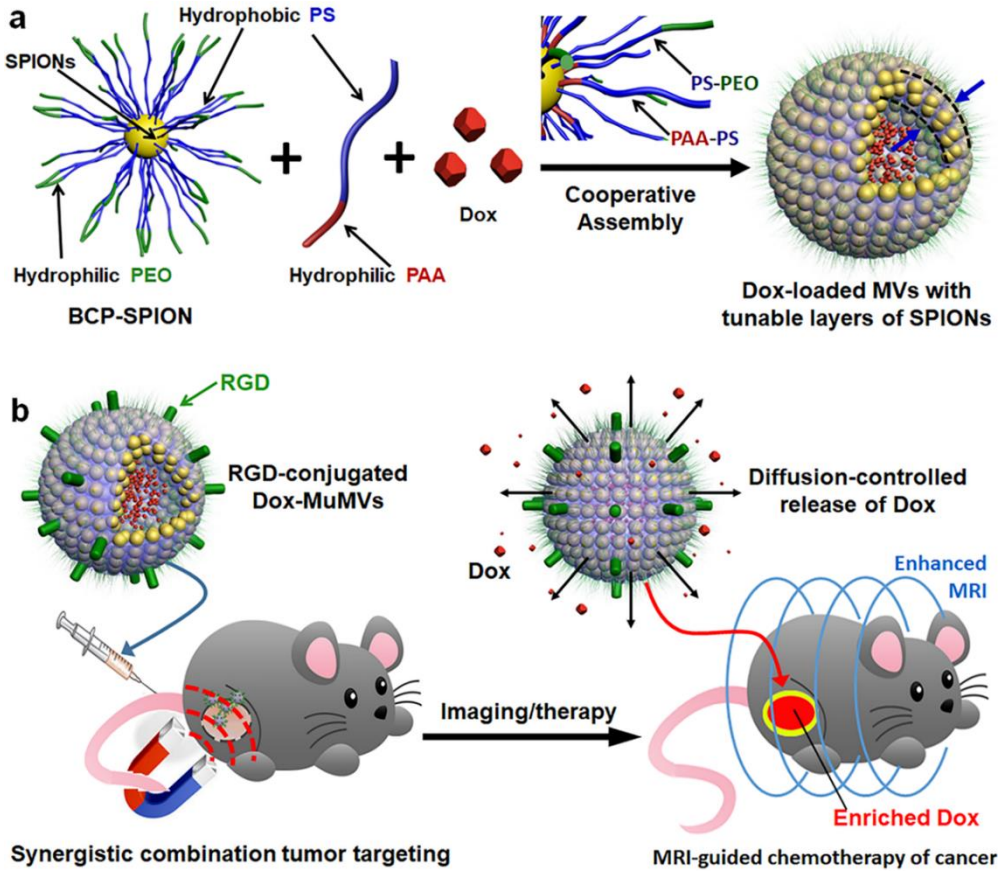

Figure 4.1 (a) Fabrication of MVs with tunable wall thickness via cooperative assembly of BCP-grafted SPIONs and free PS-b-PAA and (b) utilization of MVs for imaging-guided magnetic delivery of Dox into tumor-bearing mice.

4.2 Experiments

4.2.1 Materials

Dopamine hydrochloride, 6-maleimidohexanoic acid N-hydroxysuccinimide ester, triethylamine (≥ 99.5%, TEA), styrene, azobis(isobutyronitrile) (AIBN), 4-cyano-4-(phenylcarbonothioylthio) pentanoic acid (CPPA), dioxane, tetrahydrofuran (THF), N,N-dimethylformamide (DMF), n-butylamine, N-hydroxysuccinimide (98%, NHS), N-(3-(dimethylamino)propyl)-N'-ethyl-carbodiimide hydrochloride (98%, EDC), oleic acid (99%), 1-octadecene, doxorubicin hydrochloride (98.0 − 102.0%), Dulbecco's modified Eagle's medium (DMEM), 2-(4-Amidinophenyl)-6-indolecarbamidine dihydrochloride (DAPI dihydrochloride), and fluoresceinamine isomer I were purchased from Sigma-Aldrich. Polystyrene-*b*-poly(acrylic acid) (PS_{106}-*b*-PAA_4) was purchased from Polymer Source Inc. Fetal bovine serum (FBS), DPBS, trypsin-EDTA and penicillin/streptomycin (5000 U mL^{-1}) were purchased from Thermo Fisher Scientific.

4.2.2 Synthesis of SPIONs and Dopamine-Terminated BCPs

Hydrophobic SPIONs were prepared via thermal decomposition of iron-oleate complex by using oleic acid as the stabilizing agent.[153] Briefly, iron-oleate complex

(3.6 g, 4 mmol) and oleic acid (0.57 g, 2 mmol) were dissolved in 1-octadecene (20 g) at room temperature. The mixture was heated to 300 ° C with a constant heating rate and then kept at this temperature for 30 min. The resulting solution containing SPIONs was then cooled to room temperature and washed with ethanol three times. The precipitated SPIONs were dispersed in THF to form a stable colloidal solution with a concentration of 5 mg mL^{-1}.

Thiol-terminated BCPs of HS-PS_{260}-*b*-PEO_{45} were synthesized by the reversible addition-fragmentation chain transfer (RAFT) polymerization as reported previously.[44] Briefly, styrene, chain transfer agent (PEO-CTA), and AIBN were dissolved in dioxane with a molar ratio of 300:1:0.2. The solution was filled with nitrogen and then put into a preheated oil bath at 85 ° C for 20 h. The product was precipitated in hexane and dissolved in THF to remove unreacted monomers and impurities. Molecular weight of the BCPs characterized by ^{1}H NMR was 29.0 kg/mol, by comparing the integrals of the resonance peaks of aromatic ring of PS block (6.4-7.3 ppm) and the methylene groups of PEO-CTA (3.65 ppm) (Figure 4.2a).The CTA-PS 260 -b-PEO 45 was dissolved in THF with excess of n-butylamine under nitrogen for 4 h to convert CPPA into thiol groups. The resulting SH-PS_{260}-*b*-PEO_{45} was obtained by precipitation in hexane twice and dried under vacuum for 24 h.

Dopamine-terminated BCPs were synthesized by reacting maleimide-terminated dopamine with thiol-terminated BCPs through a Michael addition reaction. Briefly, maleimide-terminated dopamine was first synthesized by the carbodiimide reaction following a previously reported procedure.[187] Maleimide-terminated dopamine (346 mg, 1 mmol) and thiol-terminated BCPs (2.9 g, 0.1 mmol) were then dissolved in 10

mL DMF and the mixture was stirred under nitrogen for 120 h. The dopamine-terminated BCPs were obtained by precipitating in water/ethanol mixture (1/3, vol) three times and dried under vacuum for 24 h. The synthesized polymers were dissolved in $CDCl_3$ and characterized by ^1H NMR (Figure 4.2b)

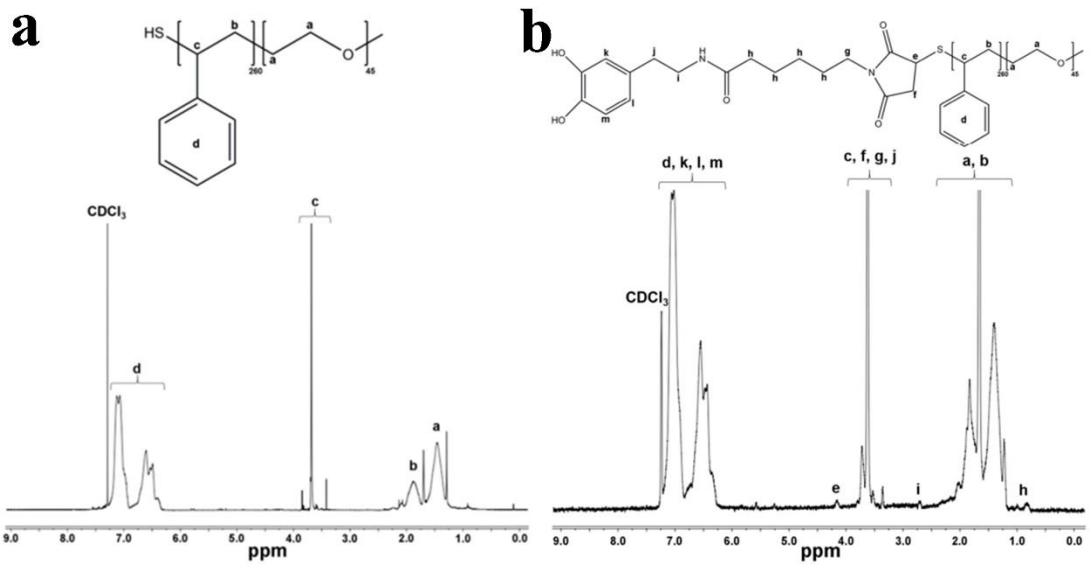

Figure 4.2 ^1H NMR spectrum of (a) PEO-*b*-PS and (b) dopamine-terminated PEO-*b*-PS

4.2.3 Surface modification and self-assembly of SPIONs into magneto-vesicles

Surface Modification of SPIONs. SPIONs were modified with amphiphilic BCPs via the chelation of dopamine with the surface of SPIONs. Briefly, SPIONs (5 mg) and dopamine-terminated BCPs (15 mg) were dispersed in THF (5 mL), and the mixture was incubated for 48 h. The solvent was evaporated and the SPIONs were washed with DMF for 5 times to remove excess BCPs. The purified BCP-tethered SPIONs were dispersed in THF with a concentration of 0.2 mg mL^{-1}. TGA was performed to estimate

grafting density of BCPs on SPIONs. Briefly, the sample (5 mg) was dried and loaded into a platinum pan which was heated to 720 °C at a constant heating rate of 25 °C min^{-1} under argon. The BCPs grafting density (σ) was calculated using the formula:

$$\sigma = \frac{f * N_A * \rho * d}{6 * M_n * (1 - f)}$$

Here *f* refers to the weight fraction of the organic ligands determined by TGA analysis; N_A is the Avogadro constant; ρ is the bulk density of SPIONs (5.15 g cm−3); *d* is the average diameter of SPIONs, and M_n is the number-average molecular weight of the PEO-*b*-PS. It is assumed that the density of the SPIONs is identical to the density of the bulk material and no free polymer is present.

Self-Assembly of SPIONs. BCP-tethered SPIONs were assembled into MVs by film rehydration method. Briefly, BCP-tethered SPIONs (100 μg) were mixed with predetermined amount of PS_{106}-*b*-PAA_4 in THF. The mixture was dried to form a thin film in a glass vial under N_2 stream, followed by rehydration in water or an aqueous solution of Dox under sonication for 30 s. The MVs with controlled wall thickness were collected by centrifugation at 2000 rpm for 15 min. By adjusting the amount of PS_{106}-*b*-PAA_4 (80 μg 160 μg, 240 μg and 320 μg), MuMVs with various membrane thickness were achieved. MoMVs were prepared in a similar way except that no PS_{106}-*b*-PAA_4 was added. For the modification of MuMVs, RGD peptides (or fluoresceinamine, FL), DCC, NHS, and PS 106 -b-PAA 4 were dissolved in DMF with a molar ratio of 1:1.5:1.5:1, followed by mechanical stirring for 24 h and precipitation in water/ethanol mixture (1/3, vol) to obtain functionalized BCPs for further self-assembly. Surface-functionalized MuMVs could be obtained by using the RGD and/or FL-conjugated PS-*b*-PAA to assemble with BCP-tethered SPIONs.

4.2.4 Characterizations

The assembled MVs were imaged using a Hitachi SU-70 Schottky field emission gun Scanning Electron Microscope (FEG-SEM) and a JEOL FEG Transmission Electron Microscope (FEG-TEM). Samples for SEM observations were prepared by dropping 5-10 μL of sample solution onto silicon wafers and dried at room temperature. TEM samples were prepared by dropping 5-10 μL of sample solution on 300 mesh copper grids covered with carbon film and dried at room temperature. To verify the vesicular structures of MuMVs, TEM images at different tilt angles (−60° to 60°) were recorded using electron microscopic tomography. The hydrodynamic diameter of MVs in solution was measured using a PHOTOCOR-FC light scattering instrument with a 5 mW laser of 633 nm at a scattering angle 90°. The zeta potential of MVs in solution was measured using a SZ-100 nanoparticle analyzer. To study the mechanism of MVs formation, PEO-*b*-PS-SPIONs were washed with THF for 3 times after addition of PS-*b*-PAA and used for TGA analysis and DLS evaluation.

4.2.5 Magnetic properties and magnetic relaxivity of MVs

Magnetic properties of MVs. Magnetic property measurements were performed using a Quantum Design MPMS 3 Superconducting Quantum Interference Device (SQUID). The magnetic moment *M* of both MVs and individual SPIONs was measured as function of applied magnetic field *H* at room temperature and low temperature. The magnetic moment of an individual grain (μ) can be determined by the Langevin paramagnetic function: $M(x)=N\mu(\coth x-(1/x))$, where $x=\mu H/k_BT$, N is the number of grains, H is the applied field, k_B is the Boltzmann's constant, and T is the absolute

temperature. In this experiment, T is 300K. We let $B=\mu/k_BT$ and $C=N\mu$ (B and C are constants to be determined). Fitting the data of $M(x)$ and H into the Langevin function, two constants B and C were determined. Finally the magnetic moment per grain can be simply calculated using $\mu=Bk_BT$ (μ_{SPIONs}=8.28E^{-17} emu; μ_{MoMVs}=8.24E^{-17} emu; μ_{DOMVs}=8.20E^{-17} emu; μ_{MuMVs}=7.87E^{-17} emu). The magnetic movement of an individual SPION is the magnetic moment of an individual grain as they are dispersed individually in an aqueous solution ($M_{SPIONs}=\mu_{SPIONs}$=8.28E^{-17} emu). However, the magnetic moment of a MV is the sum of the magnetic moment of all the subunits within the vesicle. The number of SPIONs per vesicle can be estimated according to the following:

$$N_{SPIONs} = \frac{V_{mb} * \sigma_{mb}^{SPIONs}}{V_{SPIONs}}$$

where V_{mb} is the volume of membrane calculated by $V_{mb}=\frac{4\pi(R^3-r^3)}{3}$ (R is the radius of vesicle and r is the radius of cavity), σ_{mb}^{SPIONs} is the volume fraction of SPIONs inside the polymer membrane calculated by their weight ratio of SPIONs relatively to the copolymers, and V_{SPIONs} is the volume of an individual SPION calculated by $V_{SPIONs} = \frac{\pi D^3}{6}$ (D is the average diameter of SPIONs). Here N_{SPIONs} was calculated to be 945, 2020 and 8872 for MoMVs, DoMVs and MuMVs, respectively; and the corresponding values are $M_{MoMVs}=N_{SPIONs}*\mu_{MoMVs}$=7.79E^{-14} emu; $M_{DoMVs}=N_{SPIONs}*\mu_{DoMVs}$=1.66E^{-13} emu; $M_{MuMVs}=N_{SPIONs}*\mu_{MuMVs}$=6.98E^{-13} emu.

Magnetic relaxivity measurements of MVs. The T_2 relaxivity times of individual SPIONs, MoMVs, DoMVs and MuMVs were measured at a series of different sample concentrations using a micro-MR scanner (7.0 T, Bruker, Pharmascan) with small animal-specific body coil. The Fe concentrations were determined using an Agilent 700

series inductively coupled plasma-optical emission spectrometer (ICP-OES). Briefly, a concentrated stock solution of different samples (200 µL) was added to scintillation vials. Then, 1 mL of aqua regia was added to each vial to dissolve all iron oxide nanoparticles. Finally, 9 mL of deionized water was added to the vials. The Fe concentrations of the prepared solutions were then measured using ICP-OES. The T_2 relaxivity times were plotted as a function of iron concentration to obtain the r_2 value of each sample.

4.2.6 Encapsulation and release of Dox from MVs

Dox-loaded MVs were prepared by rehydrating a film of BCP-tethered SPIONs in aqueous solutions of Dox, followed by centrifugation for six times to remove free drug molecules. The loading content of Dox in MuMVs (L_{Dox}) can be calculated by $L_{Dox} = \frac{Mass\ of\ Dox\ in\ MuMVs}{Mass\ of\ MuMVs} * 100\%$, where mass of MuMVs was measured using ICP-OES and mass of Dox in MuMVs was evaluated using a fluorescence spectrometer. Dox solutions with predetermined concentration of Dox (from 0.1 to 2.0 mg mL^{-1}) were used for the fabrication of Dox-loaded MuMVs (at constant MuMVs concentration of 0.2 mg mL^{-1}). For the drug release experiment, 1 mL solution of the Dox-loaded MVs was transferred to a dialysis tube with a molecular weight cutoff of 6000-8000 g/mol, which was incubated in a 50 mL PBS reservoir at 37 °C. One mL solution from the reservoir was taken at scheduled time intervals and its fluorescence emission at 590 nm was measured using a fluorescence spectrometer to monitor the release of Dox from

the vesicles. After each measurement, the 1 mL solution was put back into the reservoir to maintain the total volume of the buffer solution.

4.2.7 In vitro cellular uptake and cytotoxicity of MuMVs

Cellular uptake of MuMVs. The human malignant glioma cell line (U87MG) were grown in Dulbecco's modified Eagle's medium (DMEM) supplemented with 10% fetal bovine serum (FBS) and 1% penicillin/streptomycin at 37 °C in a humidified 5% CO_2 atmosphere. Cells were seeded into chambered glass cover slides and grown for 24 h. Then the culture medium was replaced with fresh medium containing saline, Dox-loaded fluoresceinamine-functionalized MuMVs (FL-MuMVs), and Dox-loaded fluoresceinamine and RGD functionalized MuMVs (FL-RGD-MuMVs), respectively (Fe concentration: 0.02 mg mL^{-1}). After incubation for 1 h, the cells were washed three times with PBS and fixed in a 4% paraformaldehyde/PBS solution for 10 min. The fixative was then removed, and cells were washed again with PBS for three times and incubated with DAPI for cellular nuclei staining. The slides were washed with PBS and then observed by a confocal microscope (Zeiss LSM 710) with appropriate band-pass filters for collection of DAPI, FL, and Dox emission signals.

For TEM observations of the vesicles after cellular internalization, the FL-RGD-MuMVs were loaded into U87MG cells as described previously, except that a monolayer of cells were grown on Thermanox@Plastic Coverslips placed inside 6-well cell-culture plates. After incubation with FL-RGD-MuMVs for 1 h, the culture medium was replaced by the fixation solution containing 2.5% paraformaldehyde and 2.0% glutaraldehyde in 0.1 M cacodylate buffer. After 1 h, the fixation solution was removed

and samples were then washed in 0.1 M sodium cacodylate buffer for three times. The samples were dehydrated and subsequently infiltrated with Epon-Aradite for 24 h, followed by polymerization at 60 ° C for 24 h. Ultrathin sections were cut on a Leica EM UC6 Ultramicrotome (Leica, Buffalo Grove, IL) and collected on copper slot grids for TEM observations.

Cytotoxicity of Dox, MuMVs, Dox-MuMVs, and RGD-Dox-MuMVs. Cytotoxicity of Dox, MuMVs, Dox-loaded MuMVs (Dox-MuMVs), and RGD-Dox-MuMVs on the U87MG cells were evaluated using the MTT assay.[188] Briefly, cells were plated at a density of 1×10^4 in 96-well plates and cultured at 37 °C for 24 h. Then the culture medium was replaced and the cells were incubated with different concentrations of Dox, MuMVs, Dox-MuMVs, and RGD-Dox-MuMVs for 1 h. The concentrations of Fe in MuMVs, Dox-MuMVs, and RGD-Dox-MuMVs as well as the concentrations of Dox in free drug, Dox-MuMVs, and RGD-Dox-MuMVs groups were kept constant for the purpose of comparison. Then the culture medium was replaced with fresh medium, and the cells were incubated for another 12 h, followed by the addition of 20 μL of the MTT solution (5 mg mL^{-1}). After incubation for 4 h, culture supernatants were carefully removed and 100 μL of DMSO was added into each well to dissolve the purple precipitate. The concentration of the reduced MTT in each well was determined spectrophotometrically by subtraction of the absorbance reading at 650 nm from that measured at 570 nm using a microplate reader (SpectraMax M5). Cell viabilities were presented as the percentage of the absorbance of Dox, MuMVs, Dox-MuMVs, and RGD-Dox-MuMVs treated cells to the absorbance of nontreated cells and plotted as Fe and Dox concentrations.

4.2.8 In vivo MRI though intravenous administration

All animal experiments were performed under a National Institutes of Health Animal Care and Use Committee (NIHACUC) approved protocol. Tumor-bearing mice were achieved by subcutaneously injecting ~ 2×10^6 U87MG cells into the right hind leg of athymic nude mice. After the tumor volume exceeded 100 mm^3, MR imaging of tumor tissues was recorded as background on a high magnetic field micro-MR scanner (7.0 T, Bruker, Pharmascan) with small animal-specific body coil. Thereafter, the mice were divided randomly into four groups (5 mice in each group) and the therapeutic agents (Dox-MuMVs or RGD-Dox-MuMVs) were intravenously injected into the tumor-bearing mice at a Dox-equivalent dose of 5 mg/kg and a Fe_3O_4-equivalent dose of 65 mg/kg. An external magnetic field was applied on the experiment groups for 1 h after injection while for the control groups no magnetic attraction was applied. Then MR images were taken to reveal the influence of magnetic attraction, RGD functionalization and synergistic magnetic and active targeting strategy on the imaging effect of the MuMVs.

4.2.9 In vivo magnetic-guided delivery of Dox though intravenous administration

The influence of magnetic attraction and RGD-mediated active tumor targeting on the delivery efficiency of therapeutic agents was investigated by fluorescence imaging. Briefly, Dox-MuMVs or RGD-Dox-MuMVs (5 mg Dox/kg corresponding to a 65 mg Fe_3O_4/kg) were intravenously injected into the tumor-bearing mice with or without the

application of magnetic fields (5 mice in each group). Whole-animal imaging was recorded 1 h later by using Maestro *in vivo* imaging system to monitor the fluorescence from Dox. Thereafter the mice were sacrificed and the tumors as well as major organs were harvested, washed, and imaged to investigate the *in vivo* biodistribution of Dox. The fluorescence intensities from Dox per unit mass in tumor tissues were also evaluated to reflect the effects of magnetic attraction and active tumor targeting on the delivery of Dox.

4.2.10 In vivo tumor suppression and mice survival of synergistic magnetic and active tumor-targeted delivery of Dox

The U87MG tumor-bearing mice were randomly divided into six groups with 5 mice in each group. The first group of mice received PBS, as control group; the second group was injected with Dox solution, as "Dox" group; the third group was injected with Dox-MuMVs without magnetic attraction, as "magnet- RGD-" group; the fourth group was injected with RGD-Dox-MuMVs without magnetic enrichment, as "magnet- RGD+" group; the fifth group was injected with Dox-MuMVs under magnetic attraction, as "magnet+ RGD−" group; the sixth group was injected with RGD-Dox-MuMVs under magnetic attraction, as "magnet+ RGD+" group. All the experimental groups (2-6 groups) are dispersed in 150 μL PBS before intravenous administration with a Dox-equivalent dose of 5 mg/kg. For the groups under magnetic attraction, the magnet was applied for 1 h along with injection of therapeutic agents. During half a month after the corresponding treatments, the volume of tumors was measured every other day and calculated by the following equation: $V = L \times W^2/2$. The body weight of

the mice was also evaluated during this period to reveal the systemic toxicity of the delivery platform.

All experiments with live animals were conducted in accordance with a protocol approved by the National Institutes of Health Animal Care and Use Committee (NIHACUC). In general, the mice must be euthanized when the tumor size reaches 2 cm, so the mice survival was evaluated based on the life span from the date when the mice received treatment to the date when the tumor size reached 2 cm. For each group subjected to the corresponding treatment, the survival rate was calculated by dividing the number of surviving mice at different days of post-treatment by the total number of mice before treatment.

4.3 Results and discussion

4.3.1 Self-assembly of MVs

Hydrophobic SPIONs with a diameter of 9.2 ± 0.6 nm were synthesized by a thermal decomposition method reported previously (Figures 4.3). Dopamine terminated PS_{260}-*b*-PEO_{45} (29.0 kg/mol) was synthesized and grafted onto the surface of SPIONs to obtain amphiphilic building blocks (Figure 4.4a). The average grafting density (σ) of BCPs is estimated to be 0.07 chains/nm^2 based on thermogravimetric analysis (Figure 4.4b).

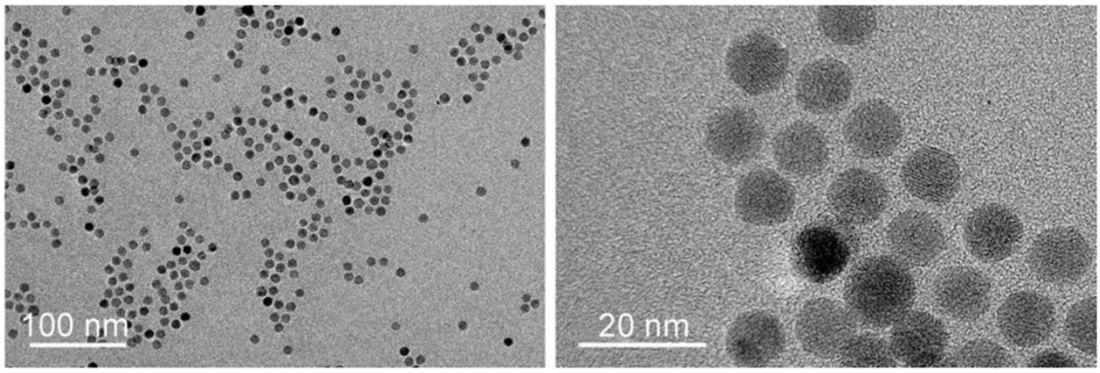

Figure 4.3 TEM images of SPIONs before the self-assembly

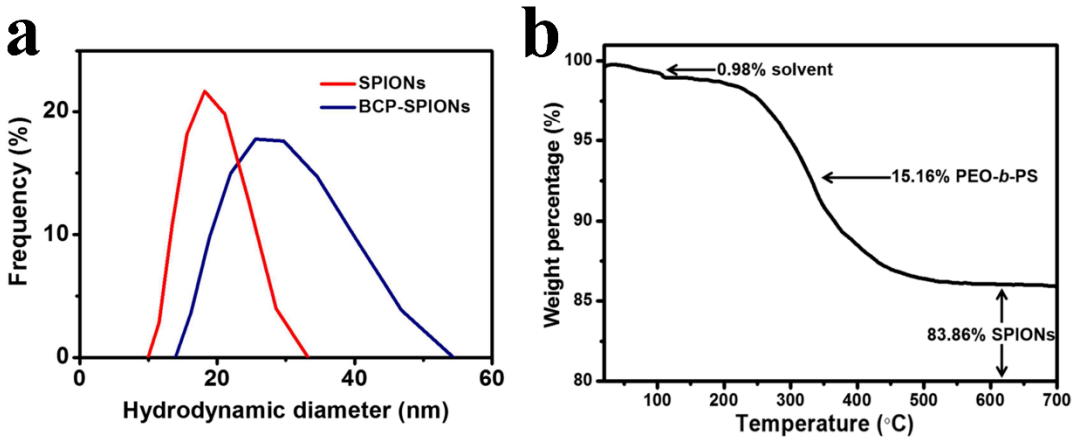

Figure 4.4 (a) Dynamic light scattering analysis of the hydrodynamic diameter of SPIONs in THF before (red) and after (blue) the grafting of amphiphilic PEO-*b*-PS on the surface and (b) TGA results of PEO-*b*-PS-tethered SPIONs

The MVs were fabricated by rehydrating a film containing both BCP-tethered SPIONs and varying amounts of PS_{106}-*b*-PAA_4 in ultrapure water. The formation of vesicular structures can be attributed to the conformation change of BCP tethers on NP surface, as we reported previously.[44,66] Scanning and transmission electron microscope (SEM/TEM) images in Figure 4.5 show that the resulting MuMVs were composed of

multilayers of highly densely packed SPIONs in the vesicular membranes.[189] The hollow interior and multilayers of SPIONs in the membrane can be clearly seen from vesicles with the occasionally broken membrane (inset in Figure 4.5a). These were confirmed by TEM observations of MuMVs at different tilt angles (Figure 4.5c). Moreover, the two peaks of Fe intensity corresponding to the edge of MVs were observed in the energy dispersive X-ray spectroscopy (EDS) line scan of MVs, which further supports the formation of vesicles (Figure 4.5d, e). The different width of peaks in the two systems also indicates the significant difference in the wall thickness of vesicular membranes. The average diameter of the MuMVs was estimated to be 263.3 ± 36.9 nm by TEM analysis. The surface of MuMVs is highly negatively charged (with a zeta potential of -75.2 mV), indicating the successful integration of PS-*b*-PAA chains in the vesicular membranes. We found that the MuMVs are stable for days under the physiological environment, such as in phosphate-buffered saline (PBS) and PBS supplemented with 10% fetal bovine serum (Figure 4.6).

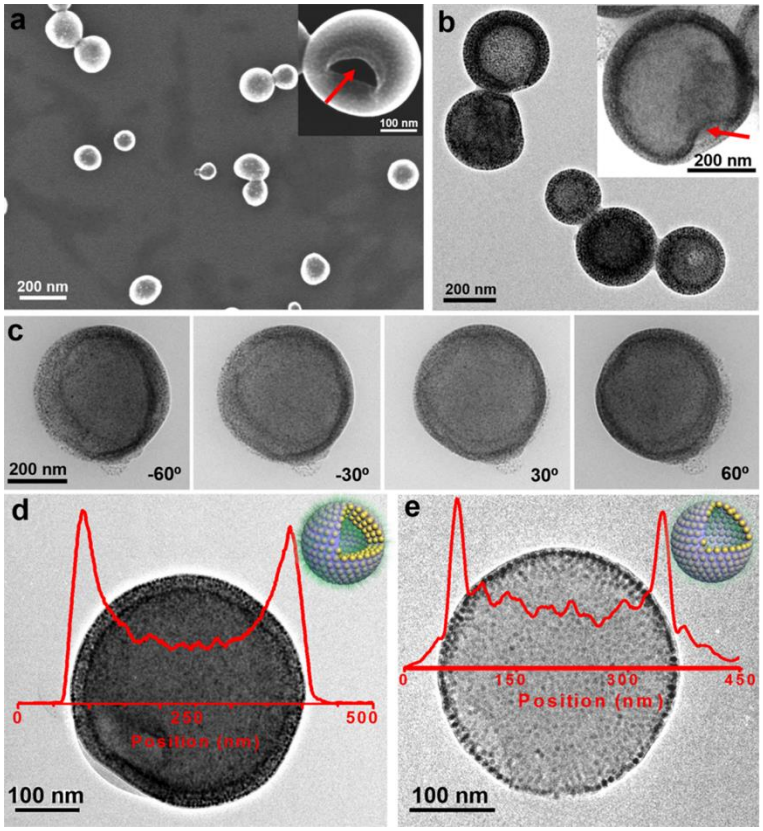

Figure 4.5 (a) Representative SEM and (b, c) TEM images of MuMVs self-assembled from BCP-SPIONs. (d, e) STEM image and Fe intensity line scan for (d) MuMVs and (e) MoMVs showing the vesicular structure of the self-assemblies

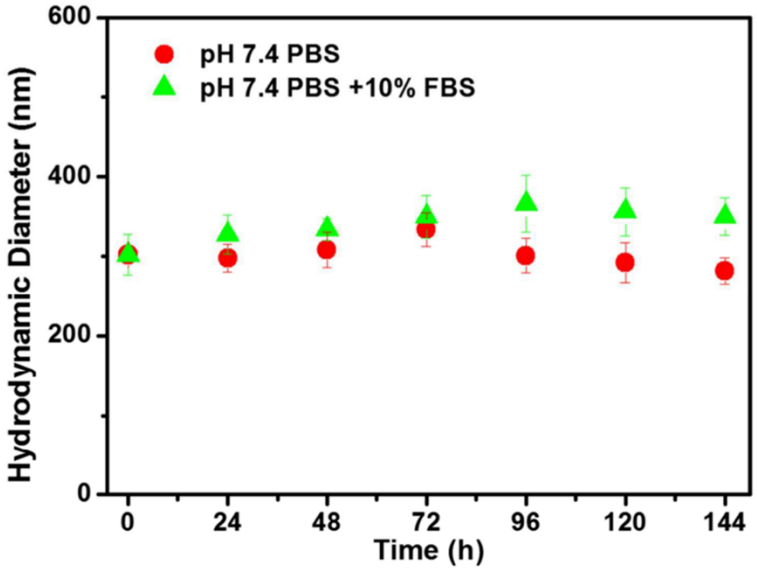

Figure 4.6 Hydrodynamic size distribution of MuMVs in PBS and PBS supplemented with 10% FBS

4.3.2 Tunable morphology and membrane thickness of MVs

The formation of MVs with tunable morphology and membrane thickness was determined by the relative weight content of PS-b-PAA to SPIONs (W_{BCP}/W_{SPION}) in the assembly process. TEM images in Figure 4.7 show the MVs with different membrane thickness obtained by varying W_{BCP}/W_{SPION} (at fixed W_{SPION} of 100 μg) for assembly. Without the addition of PS-*b*-PAA, pristine PS-*b*-PEO-tethered SPIONs assembled into MoMVs with a monolayer of SPIONs (Figure 4.7a). This is supported by the analysis of membrane thickness: the average wall thickness (T_{MV}) of the MoMVs was measured to be 9.8 ± 1.5 nm, which is close to the size of SPIONs (9.2 ± 0.6 nm) (Figure 4.7e). When $W_{BCP}/W_{SPION} \approx 0.8$, DoMVs were obtained with two layers of SPIONs embedded in the polymer wall (Figure 4.7b). In this case, the measured T_{MV}

of 24.1 ± 3.8 nm was slightly larger than two times of T MV (19.6 nm) of the monolayer membrane, because of the presence of additional PS-*b*-PAA (Figure 4.7e). Further increasing W_{BCP}/W_{SPION} to the range of ~ 1.6 − 3.2 resulted in the formation of MuMVs with more layers of SPIONs (Figure 4.7c, d). Meanwhile, T_{MV} of the MVs increased up to 93.2 ± 12.9 nm for MuMVs with the thickest membrane (Figure 4.7e). However, at $W_{BCP}/W_{SPION} > 3.2$, aggregates rather than vesicles were obtained. The coassembly of different structures was summarized in a product diagram in Figure 4.7f. With increasing amount of PS-*b*-PAA, the morphology of assemblies underwent a transition from MoMVs, DoMVs, to MuMVs, and eventually to random aggregates. At a fixed W_{BCP}, a morphological transition from aggregates to MuMVs or from MuMVs to DoMVs was observed with increasing W_{SPION}, depending on the value of W_{BCP}.

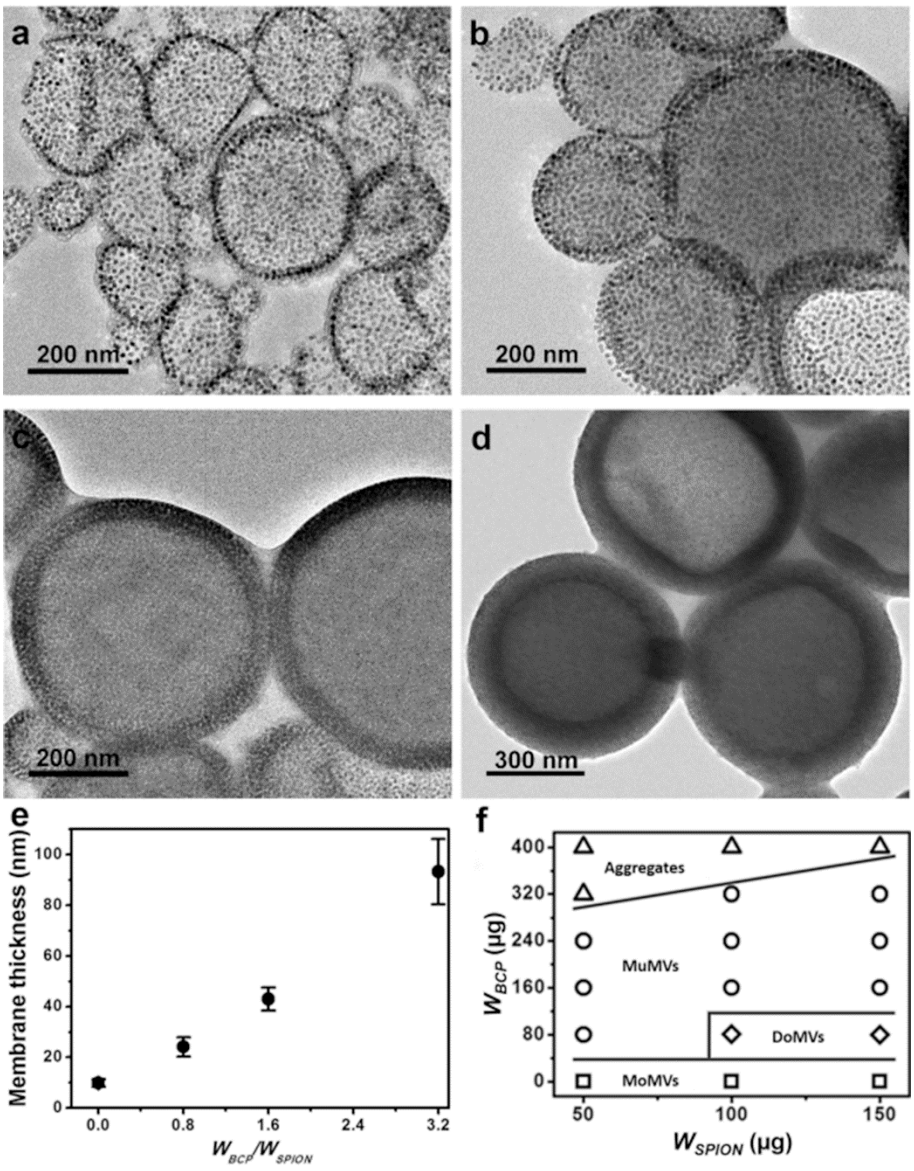

Figure 4.7 (a-d) TEM images of MVs with various membrane thicknesses: (a) MoMVs, (b) DoMVs, and (c,d) MuMVs. (e) Membrane thickness of MVs as a function of weight ratio of PS-b-PAA to BCP-SPIONs (W_{BCP}/W_{SPION}). (f) The product diagram for the self-assembly of BCP-SPIONs with varying amounts of SPIONs and additional BCP of PS-*b*-PAA

We presume that the assembly of MVs with controlled membrane thickness is attributed to the modulation of the physical property of colloidal building blocks via the cooperative interactions between PS-*b*-PEO grafted SPIONs and free PS-*b*-PAA. Figure 4.8a-c illustrates the hypothetic mechanism of morphological control in the assembly. In the absence of free PS-*b*-PAA, the long, flexible PS-*b*-PEO chains grafted on the NPs undergo conformation change in response to polar solvent water. Hydrophilic PEO blocks are preferentially exposed to water while hydrophobic PS blocks tend to be shielded from water to minimize the interfacial free energy, thus leading to the formation of MVs composed of a monolayer of SPIONs (Figure 4.8a).[190-192] The detailed assembly mechanism has been discussed in our previous work on the fabrication of plasmonic vesicles comprising a monolayer of BCP-tethered gold NPs. When PS-*b*-PAA is added in the dispersion of PS-*b*-PEO grafted SPIONs in THF, the free BCPs could bind to the NPs with hydrophobic PS ends extending to the solvent media, due to the strong affinity of carboxyl groups to SPIONs. The relatively low σ of PS-*b*-PEO on SPIONs (vs σ = ~ 0.10 chains/nm^2 for thiol-terminated BCPs on GNPs of similar size) may also contribute to the insertion of PS-b-PAA in-between PS-*b*-PEO brushes on the surface of SPIONs. Upon the rehydration of dried thin films of such mixture in water, the hydrophobic PS ends of inserted PS-*b*-PAA chains tend to segregate away from the nonsolvent, while maximizing the exposure of hydrophilic PEO segments of PS-*b*-PEO brushes. At optimal ratio of W_{BCP}/W_{SPION}, DoMVs with bilayer of SPIONs are formed after assembly. Further increasing the amount of PS-*b*-PAA leads to an even higher σ of PS blocks on NP surface and the further increase in the hydrophobicity of the NP building blocks. As a result, more SPIONs grafted with

both PS-*b*-PAA and PS-b-PEO segregated in the center of the vesicular membrane, leading to the formation of MuMVs with more layers of SPIONs.

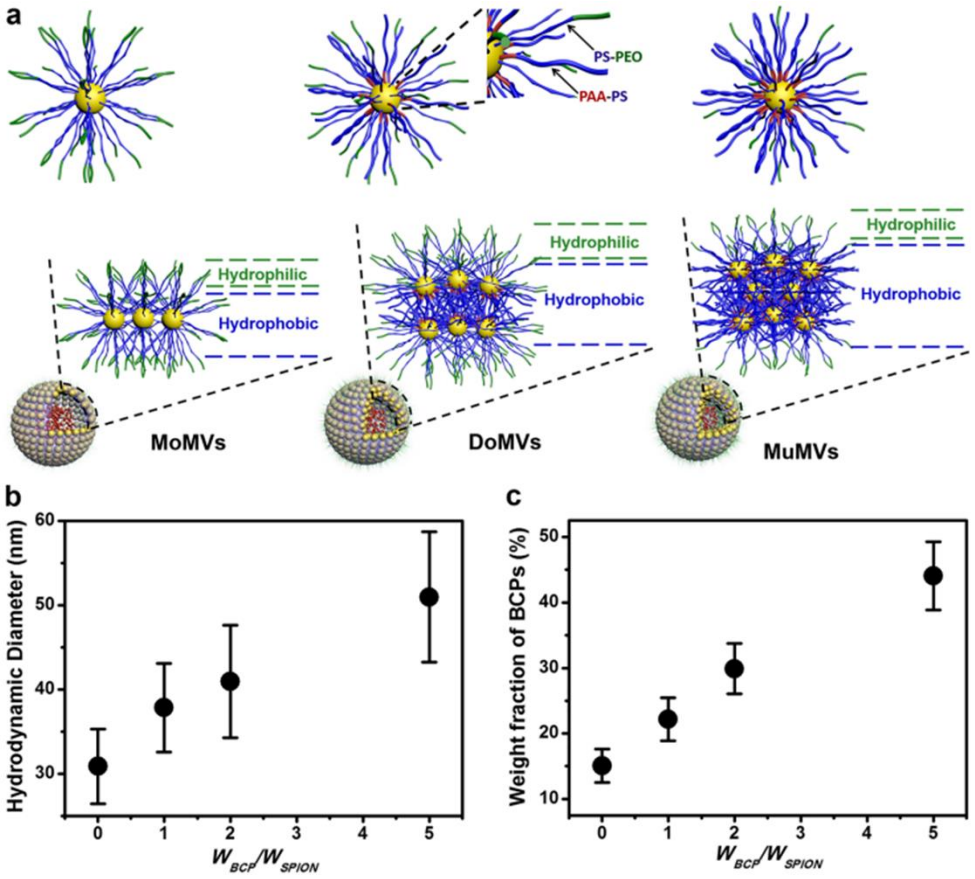

Figure 4.8 (a) Mechanism for the formation of MoMVs, DoMVs and MuMVs at different W_{BCP}/W_{SPION} due to the cooperative interaction between BCP-grafted SPIONs and free PS-*b*-PAA. (b) Hydrodynamic diameter of SPIONs and (c) weight fraction of total BCPs in hybrid BCP-SPIONs with increasing W_{BCP}/W_{SPION}

The mechanism we proposed is supported by our control experiment with free PS-*b*-PEO and our evidence on the attachment of PS-b-PAA on the PS-b-PEO grafted SPIONs. First, when free PS-b-PEO instead of PS-b-PAA was added, the assembly of

BCP-SPIONs led to the formation of irregular aggregates rather than MVs with controlled layers of SPIONs in membranes (Figure 4.9). Second, the hydrodynamic diameter of BCP-SPIONs was found to increase significantly from 30.87 ± 4.44 nm to 50.97 ± 7.75 nm with increasing feeding ratio of PS-*b*-PAA, as shown in Figure 4.8b (BCP-SPIONs were dispersed in THF for DLS analysis and untethered BCPs were removed by careful centrifugation). This could be attributed to a denser polymer layer around SPIONs formed by anchoring PS-*b*-PAA onto NP surface. The same trend was also observed in the thermogravimetric analysis (TGA) of the amount of ligands on SPIONs with the addition of PS-*b*-PAA (unattached PS-*b*-PAA was removed by centrifugation). The weight fraction of polymers increased from 15.1% for pristine PS-*b*-PEO-tethered SPIONs to 44.0% for BCP-SPIONs when excess PS-*b*-PAA was added (W_{BCP}/W_{SPION} = 5) (Figure 4.8c).

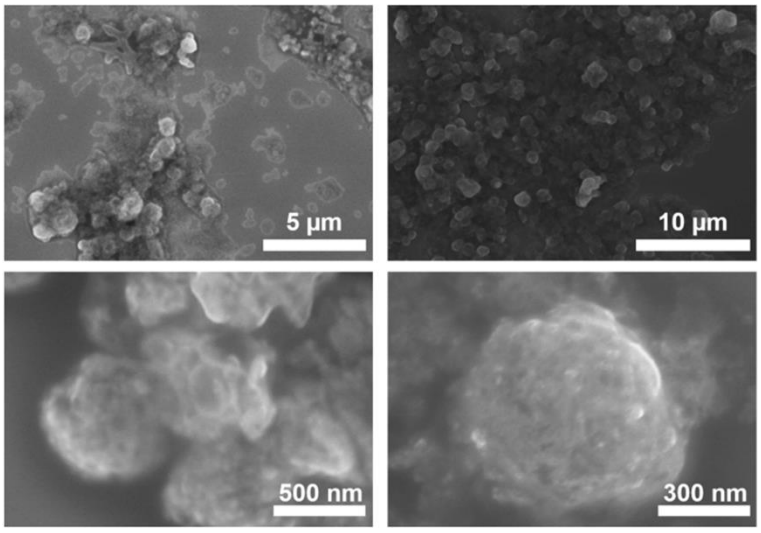

Figure 4.9 Representative SEM images of irregular aggregates assembled from a mixture of PS-*b*-PEO grafted SPIONs and free PS-*b*-PEO. When PS-*b*-PAA was

replaced by PS-*b*-PEO without affinity to the surface of SPIONs, the assembly did not produce MVs with tunable layers of SPIONs in the membranes

4.3.3 Magnetic properties of MVs

The MVs exhibited superparamagnetic properties at room temperature, although their overall diameter was well above the threshold size for the superparamagnetic/ferromagnetic transition of iron oxide NPs. As shown in the SQUID measurement (Figures 4.10a-d), the hysteresis loop of MVs showed no remanence at 300K, indicating their superparamagnetic behavior similar to that of individual SPIONs. By fitting the data from SQUID tests with the Langevin paramagnetic function, the magnetic moments for individual SPIONs, MoMVs, DoMVs and MuMVs were estimated to be 8.28×10^{-17} emu/particle, 7.79×10^{-14} emu/vesicle, 1.66×10^{-13} emu/vesicle, and 6.98×10^{-13} emu/vesicle, respectively (Figures 4.10e-i).[193] This suggests that individual MuMVs can respond more strongly to magnetic field than individual SPIONs and other assemblies. When a magnet ($3.8 \times 3.8 \times 2.5$ cm^3, 0.43 T) was applied, MuMVs were completely moved from solution toward the magnet within 2 min, while SPIONs remained homogeneous in the solution without any visible movement for hours (Figure 4.11). The strong magnetic movement of MuMVs makes them more suitable for magnetic field-assisted targeting and drug delivery.

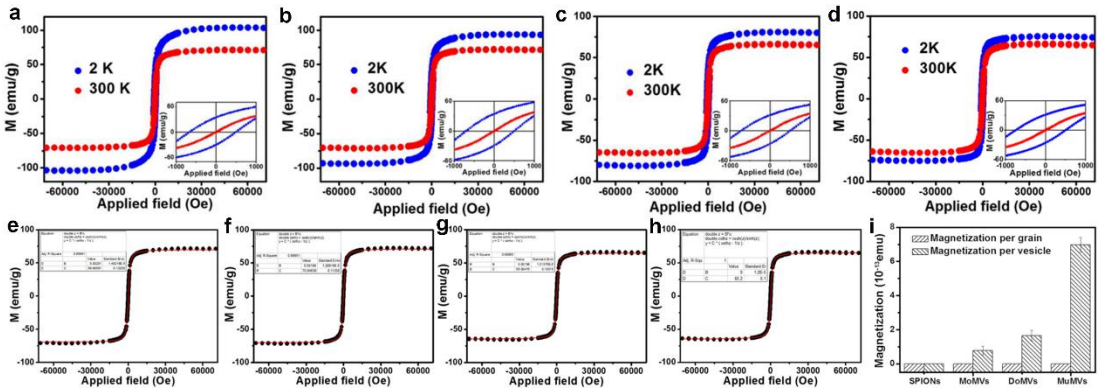

Figure 4.10 Hysteresis curves of (a) SPIONs (b) MoMVs (c) DoMVs and (d) MuMVs measured at 300 and 2 K. The magnetization of (e) individual SPIONs, (f) SPIONs in MoMVs, (g) SPIONs in DoMVs and (h) SPIONs in MuMVs was obtained by fitting the data into the Langevin paramagnetic function. Magnetization of each grain in individual SPIONs and MVs and the corresponding net magnetization of SPIONs and MVs are summarized in (i)

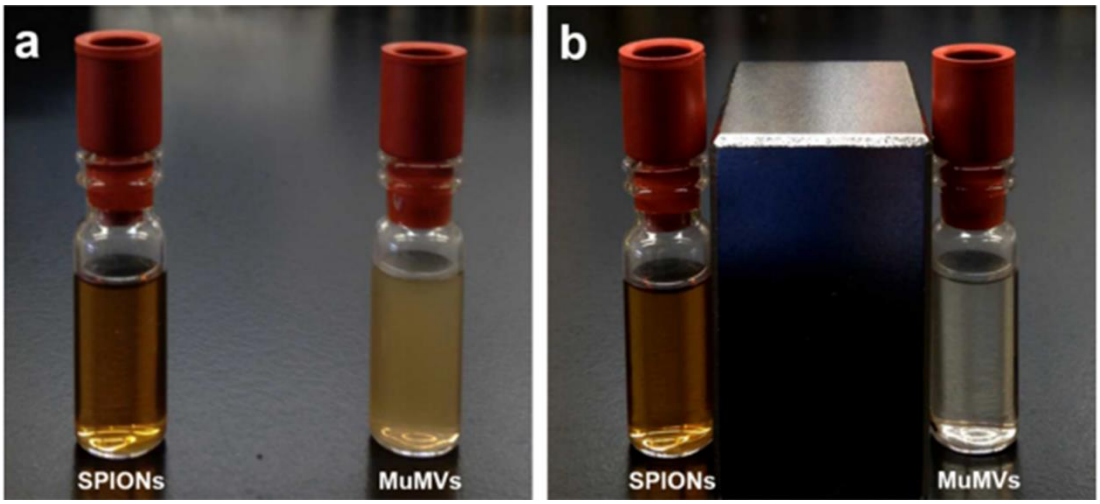

Figure 4.11 Photographs of equal concentrations of aqueous SPIONs and MuMVs dispersions (a) without magnetic field and (b) with the application of magnetic field for 2 min

To evaluate the potential use of MVs in MRI, we quantitatively compared the r_2 values of individual SPIONs, MoMVs, DoMVs, and MuMVs by plotting the inverse relaxation times ($1/T_2$) as a function of iron concentration [Fe] (Figure 4.12a). The r_2 value determined by the slope of the plot was 293.6 mM^{-1} s^{-1} for MuMVs, which was 1.8, 2.0, and 2.7 times higher than that for DoMVs (167.1 mM^{-1} s^{-1}), MoMVs (149.9 mM^{-1} s^{-1}), and individual SPIONs (108.7 mM^{-1} s^{-1}). We presume that the high density of SPIONs in the vesicular membranes increased r_2 of MuMVs due to enhanced overall magnetic moment and magnetization.[194-196] The measurements were consistent with the trend of the darkness in our T_2-weighted MR images with different iron concentrations in aqueous dispersion: MuMVs > DoMVs > MoMVs > individual SPIONs (Figure 4.12b). Thus, we chose MuMVs, which exhibit the highest magnetization and r_2 value, for our subsequent *in vitro* and *in vivo* studies.

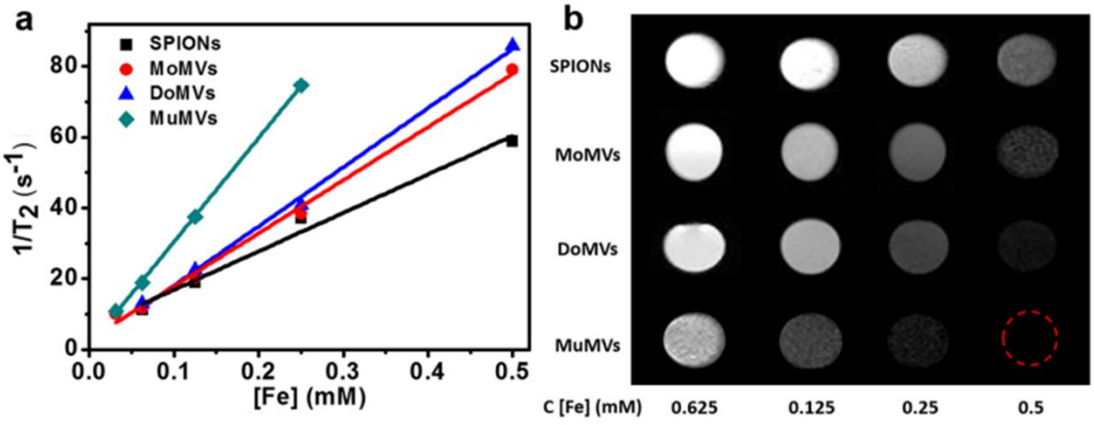

Figure 4.12 (a) Spin-spin $1/T_2$ relaxation rates of different nanostructures as a function of iron concentration. (b) T_2-weighted MRI images of different morphologies with various iron concentrations

4.3.4 In vitro cellular uptake and cytotoxicity of MuMVs

We evaluated the performance of MuMVs for *in vitro* targeting and drug delivery to tumor cells using Dox as a model drug. The use of film rehydration method enables more efficient encapsulation of therapeutic agents than postencapsulation using dialysis approach. The loading capacity of Dox in MuMVs could be tuned from 7.8% to 27.8% by controlling the concentration of Dox in solutions for rehydration. The maximum loading content of 27.8% was achieved with an initial concentration of Dox at 1 mg mL^{-1}, while further increase in the initial concentration of Dox in solutions to ~ 1.5 mg mL^{-1} led to a drastic drop in the loading content of Dox in MuMVs. We presume that this was attributed to the formation of broken vesicles due to the significantly increased viscosity of Dox solution. The release of Dox from the MVs was found to be strongly dependent on the composition of the vesicular membrane (Figure 4.13a). The release rate of Dox from MVs increased with the increasing W_{BCP}/W_{SPION}, while a negligible amount of Dox release (<7%) was observed from MoMVs after 48 h. We presume that this can be explained by the impermeability of SPIONs to Dox and high mobility of low molecular weight PS_{106}-*b*-PAA_4. When more PS-*b*-PAA are added, the less dense packing of impermeable SPIONs increases the transport of Dox molecules through the membranes. Moreover, untethered PS-*b*-PAA chains with high mobility may present in the vesicular membranes, leading to the increase in the permeability of membranes for small molecular drugs.

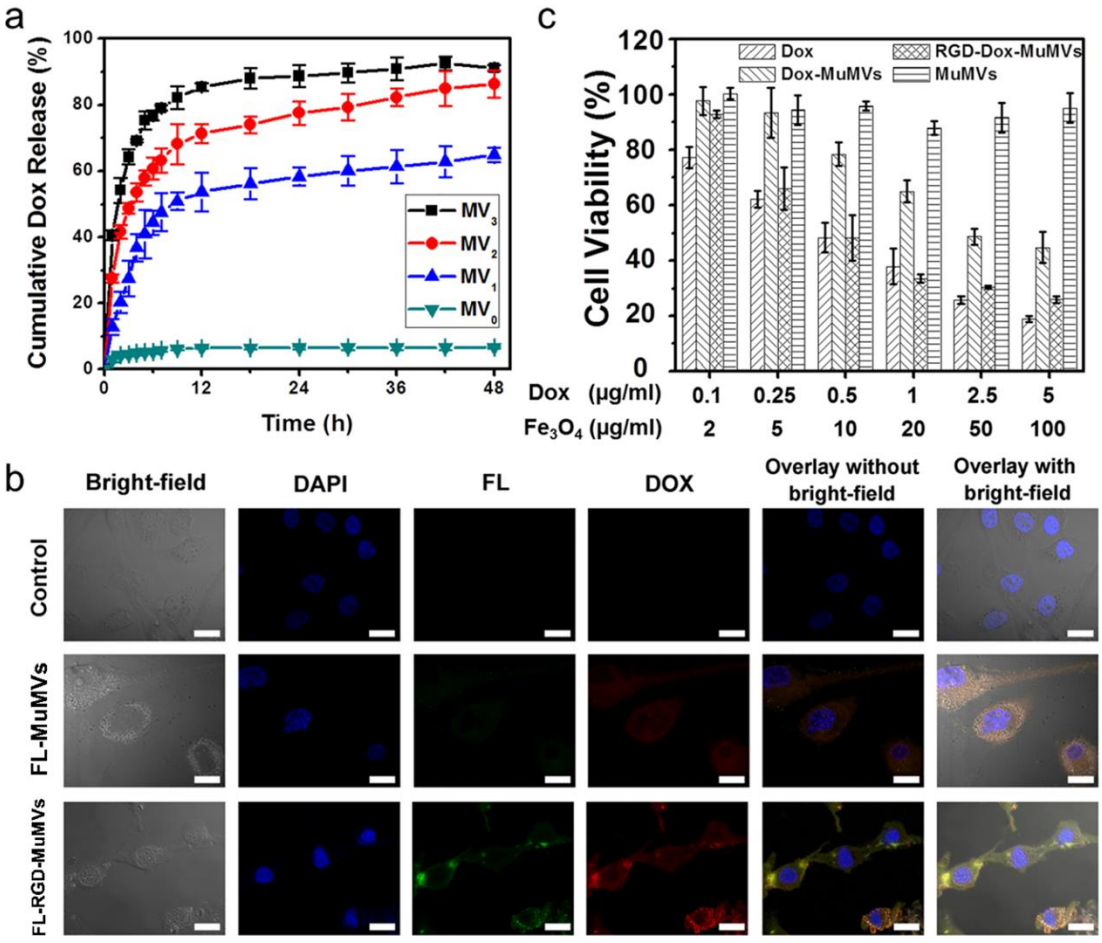

Figure 4.13 (a) *In vitro* release of Dox from MVs with different contents of PS-*b*-PAA added in the assembly: MV_0 (MoMVs, $W_{BCP}/W_{SPION} = 0$), MV_1 (DoMVs, $W_{BCP}/W_{SPION} = 0.8$), MV_2 (MuMVs, $W_{BCP}/W_{SPION} = 1.6$), MV_3 (MuMVs, $W_{BCP}/W_{SPION} = 3.2$). (b) Confocal microscope images showing enhanced targeting and Dox delivery from Dox-loaded FL-RGD-MuMVs to U87MG cells. The nuclei were stained by DAPI and the vesicular membranes were labeled with fluoresceinamine. Cells treated with PBS and Dox-loaded FL-MuMVs were used as control groups. (Scale bar: 20 μm) (c) *In vitro* cytotoxicity of Dox, Dox-MuMVs, RGD-Dox-MuMVs, and blank MuMVs to U87MG cells after incubation for 12 h.

Fluoresceinamine (FL) for labeling and RGD peptides for targeting were conjugated onto the carboxyl groups of PS-*b*-PAA via a carbodiimide reaction.[197] The resultant PS-*b*-PAA was used to coassemble with BCP-tethered SPIONs to form surface-functionalized MuMVs. Subsequently, the FL and RGD conjugated Dox-MuMVs (FL-RGD-MuMVs) were incubated with U87MG human malignant glioma cells for 1 h, followed by confocal laser scanning microscopy (CLSM) imaging. Cells treated with saline or FL-labeled Dox-MuMVs without RGD modification (FL-MuMVs) were used as control groups. Figure 4.13b shows that considerable amount of FL-RGD-MuMVs were internalized and distributed in the cytoplasm of U87MG cells with the overexpression of $\alpha_v\beta_3$ integrin that specifically binds to RGD sequence. In contrast, the internalization of FL-MuMVs was much lower, as evidenced by a weaker green and red fluorescence inside the tumor cells. Minimal green fluorescence was observed inside the nucleus as the MuMVs are too large to penetrate nuclear pores. However, large amount of Dox could be released from the vesicles and further diffuse into the nucleus to inhibit tumor growth after cellular internalization, as evidenced by fairly strong red fluorescence throughout the cells.

The *in vitro* cytotoxicity of free Dox, MuMVs, Dox-MuMVs, and RGD-Dox-MuMVs against U87MG cells was evaluated by using the 3-(4,5-dimethylthiazol-2-yl)-2,5-diphenyltetrazolium bromide (MTT) assay (Figure 4.13c). No significant toxicity was found for cells treated with MuMVs at all studied concentrations. In contrast, free Dox, Dox-MuMVs, and RGD-Dox-MuMVs all exhibited a dose-dependent cytotoxicity on the tumor cells with IC 50 values of 470, 2381, and 474 ng mL^{-1} (Dox concentration), respectively. This suggests a comparable tumor inhibition

efficacy of RGD-Dox-MuMVs to free Dox molecules, both of which could be efficiently internalized into tumor cells. Conversely, a much lower tumor inhibition by Dox-MuMVs could be attributed to the limited diffusion of Dox from noninternalized vesicles into tumor cells, since they were not able to effectively enter tumor cells within the incubation period.

4.3.5 In vivo Dox delivery and tumor inhibition of MuMVs

We assessed the synergistic magnetic field-driven targeting and RGD-based active targeting of tumors in athymic nude mice bearing U87MG tumors. The mice were intravenously injected with one of the groups: Dox-MuMVs (magnet ±) or RGD-Dox-MuMVs (magnet ±) at equivalent Dox dose (5 mg Dox/kg corresponding to a 65 mg Fe_3O_4/kg). Subsequently, a magnetic field (0.43 T) was applied for 1 h for the positive (+) groups. Compared with mice injected with Dox-MuMVs (magnet −), the enhancement in the negative MRI contrast (darkening) in tumors was found to be 20.1%, 54.6%, and 87.6% from the baseline for the groups of RGD-Dox-MuMVs (magnet −), Dox-MuMVs (magnet +), and RGD-Dox-MuMVs (magnet +), respectively (Figure 4.14a). The result confirms that intravenously injected MuMVs can be effectively enriched in tumors due to the synergistic effect of magnetic and active tumor targeting. The magnetic-field enhanced accumulation of MuMVs is more significant than individual SPIONs and even micelles or clusters composed of SPIONs.[198] We expect that a further enhancement in tumor accumulation of MuMVs could be achieved if a stronger magnetic field and/or a longer attraction time is applied.

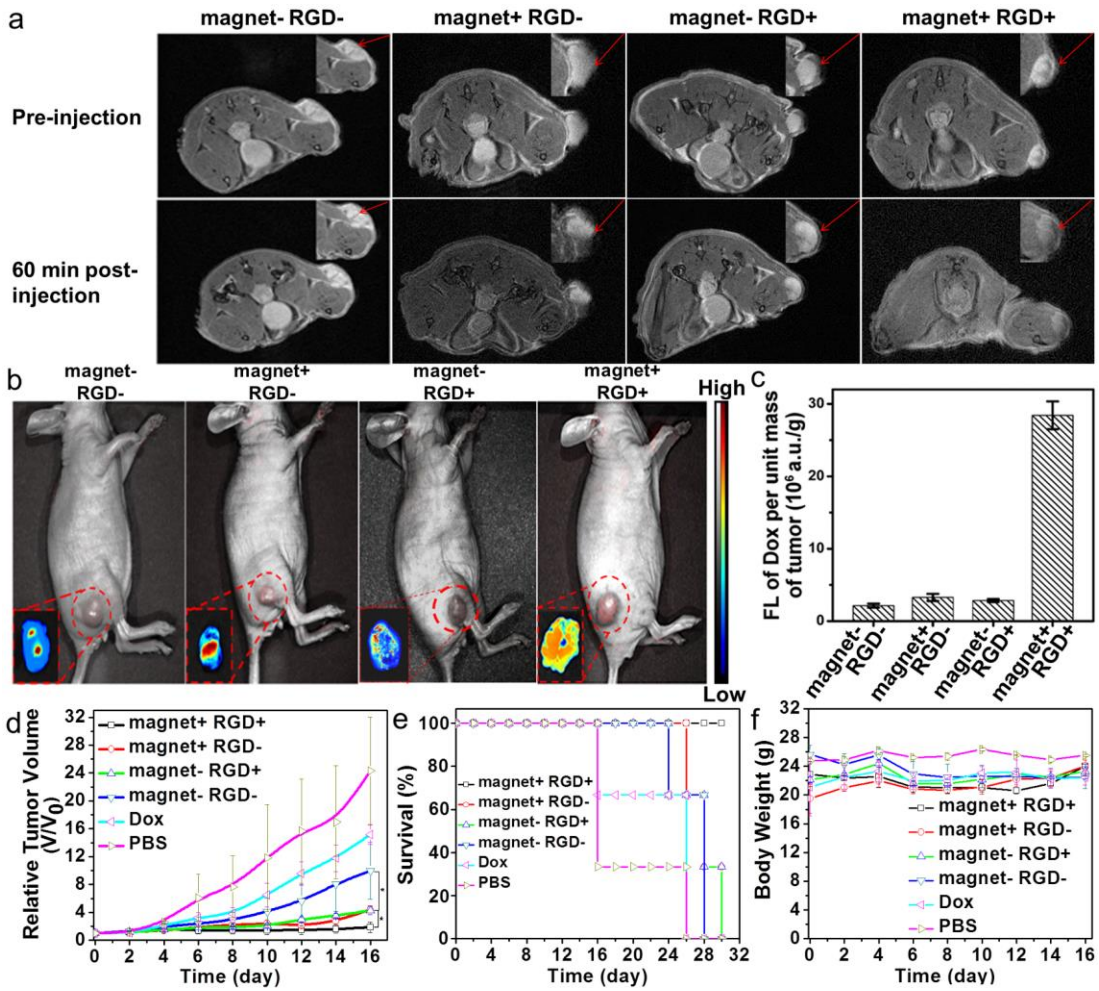

Figure 4.14 (a) *In vivo* T_2-weighted MRI of tumor areas (insets) in U87MG tumor-bearing mice 1 h after the intravenous injection of different sample groups: Dox-MuMVs (magnet ±) and RGD-Dox-MuMVs (magnet ±). Red arrows indicate the darkened areas in the tumor. (b) *In vivo* fluorescence imaging of Dox in tumors (insets) 1 h after the intravenous injection of different sample groups: Dox-MuMVs (magnet ±) and RGD-Dox-MuMVs (magnet ±). (c) Quantitative analysis of fluorescence intensity in corresponding tumor regions in (b). (d) Tumor growth curve, (e) survival curve and (f) body weight variation of U87MG tumor-bearing mice after different treatments: PBS, free Dox (Dox), Dox-MuMVs (magnet ±), and RGD-Dox-MuMVs (magnet ±).

Error bars from (c) to (f) represent the standard deviations of 5 mice per group. *, $p<0.01$.

We evaluated the delivery of Dox in tumors for the aforementioned groups by tracing the red fluorescence of Dox. Only a weak fluorescence signal in tumors was observed for mice treated with Dox-MuMVs (magnet −) and RGD-Dox-MuMVs (magnet −) (Figure 4.14b). The fluorescence was slightly higher for mice treated with Dox-MuMVs (magnet +). In contrast, the group of RGD-Dox-MuMVs (magnet +) exhibited the strongest fluorescence of Dox in tumors among all the groups. After *in vivo* imaging, the mice were sacrificed and tumor tissues were harvested for quantitative *ex vivo* imaging. Compared with the mice injected with Dox-MuMVs (magnet −), the fluorescence in tumor tissues exhibited a 1.6-, 1.3-, and 11.8-fold increase for the groups of Dox-MuMVs (magnet +), RGD-Dox-MuMVs (magnet −), and RGD-Dox-MuMVs (magnet +), respectively, indicating the enhanced delivery efficacy thanks to a synergetic magnetic and active targeting strategy (Figure 4.14c). Major organs of mice were also collected for *ex vivo* quantitative analysis of Dox biodistribution with and without targeting strategies (Figure 4.15). In the control groups (magnet −, RGD −), only 0.70% of injected Dox was observed at the tumor site while 7.0% and 1.4% of Dox was found in liver and spleen, respectively. However, the accumulation of Dox in tumor significantly increased to ~ 6.0% with combined magnetic and active targeting, comparable to those in liver (7.4%) and spleen (1.1%).

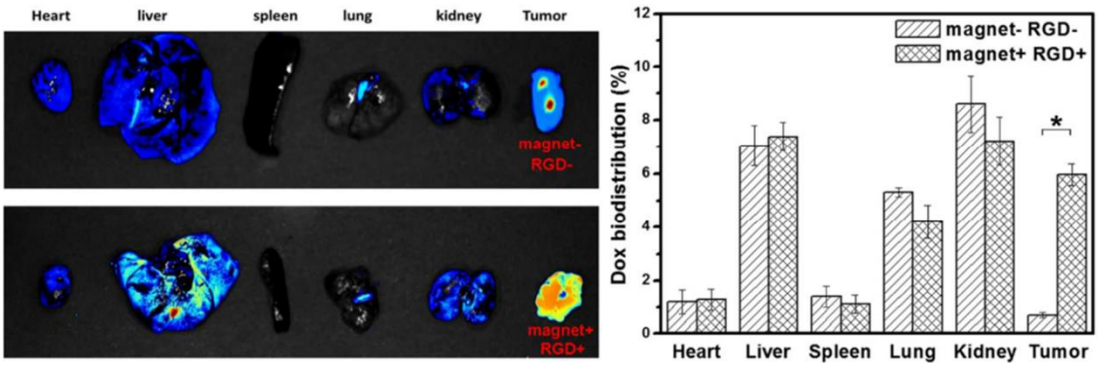

Figure 4.15 Biodistribution of Dox after intravenous injection of Dox-MuMVs (magnet-) and RGD-Dox-MuMVs (magnet+) into subcutaneous U87MG tumor-bearing mice. *, $p<0.01$.

The rapid clearance of relatively large particles by the reticuloendothelial system (RES) is known to reduce the accumulation of particles in diseased sites.[13,199] It is interesting that the fast accumulation of MuMVs in tumors via combination targeting strategies ensures less RES capture and enhanced delivery efficiency, although their size is larger than 200 nm. We presume that this can be attributed to the following two aspects. First, the MuMVs are composed of highly elastic vesicular membrane (in contrast to rigid solid NPs), which enables them to deform their shape and to penetrate into tumor tissues under an external magnetic field. This is partially confirmed by the fact that the MuMVs with a diameter of ~ 260 nm can readily pass through channels with a diameter of 200 nm (Figure 4.16). Second, the magnetic force exerted on a single MuMV is directly proportional to the cumulative SPIONs in a vesicle. With the increase of vesicle size, more SPIONs can be loaded in the vesicle membrane and a stronger net magnetic force could be exerted to drive MuMVs to accumulate in tumors. The result is in agreement with previous reports that SPIONs-loaded magnetic capsules

larger than 200 nm performed better in magnetic targeting than small-sized SPIONs *in vivo*.[198]

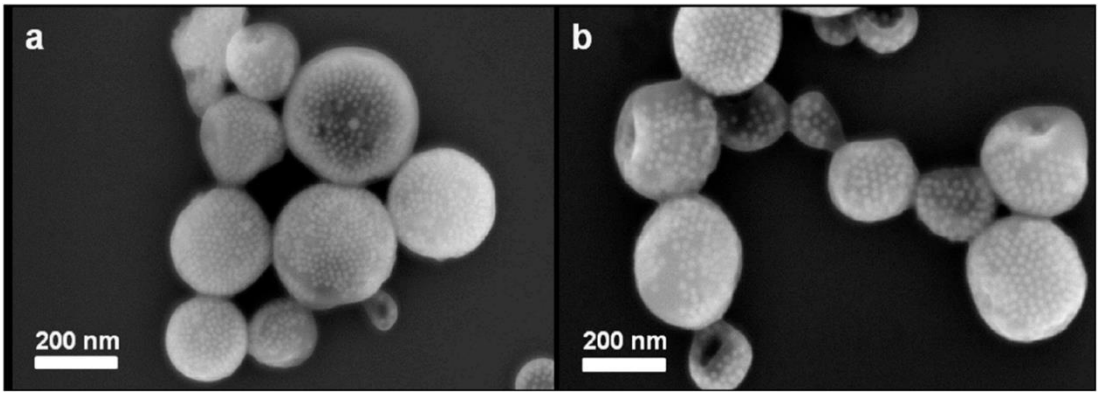

Figure 4.16 SEM images of MuMVs (a) before and (b) after filtration through a 200 nm filter

We further investigated the therapeutic efficacy by monitoring the tumor volume change every 2 days over 16 days (Figure 4.14d). It was found that the mice treated with PBS buffer exhibited a rapid increase in the size of the tumors. Minor delay in tumor growth was observed in the mice treated with Dox or Dox-MuMVs (magnet −) due to the low delivery efficiency. Thanks to the active or magnetic targeting capacity, both RGD-Dox-MuMVs (magnet −) and Dox-MuMVs (magnet +) treated mice exhibited improved efficacy of tumor growth inhibition. In contrast, the tumor was nearly completely eradicated for the mice treated with RGD-Dox-MuMVs (magnet +). Moreover, the mice treated with RGD-Dox-MuMVs (magnet +) exhibited a much longer survival life without a single death or tumor reccurrence (over 30 days) as compared to all the other groups (Figure 4.14e). Meanwhile, negligible loss of body

weight was observed for all the groups of mice during the therapeutic period (Figure 4.14f), indicating minimal systemic toxicity of drug carriers.

4.4 Conclusions

In summary, we have developed a new class of MVs with tunable layers of densely packed SPIONs in the polymeric membrane for tumor-targeted imaging and delivery. The morphology of the vesicles could be controlled from monolayer, double layer to multilayer vesicles, and the membrane thickness increased significantly with increasing feeding ratio of PS-b-PAA to SPIONs. The MuMVs with a thicker membrane and higher SPIONs density were found to possess unique features such as enhanced contrast in MRI, high magnetization per vesicle, and tunable release profile of therapeutic agents. Upon intravenous administration, the MuMVs conjugated with RGD targeting moieties can be efficiently enriched at the tumor site *in vivo* with the assistance of an external magnetic field, thanks to the synergistic magnetic and active tumor targeting effect. The enhanced tumor accumulation of MuMVs enables the efficient imaging of tumors by MRI, tumor targeted delivery of payload and a resultant enhanced tumor inhibition. We envision that such MuMVs may find applications for imaging-guided delivery of therapeutic agents to patients with inoperable but shallow tumors, such as advanced head and neck cancers.

Chapter 5: Conclusions and Future work

5.1 Conclusions

The objective of this dissertation was to design and fabricate hybrid polymer-inorganic nanoassemblies for biomedical applications. The HPINs naturally combine the complementary properties of inorganic NPs and polymers for improved performance in cancer imaging and therapy.

In chapter 2, we demonstrate an enzyme-free signal amplification technique, based on plasmonic vesicles assembled from BCP-tethered GNPs as the membrane. The vesicles encapsulated Pd-Ir nanoparticles as peroxidase mimics for colorimetric assay of disease biomarkers with significantly enhanced sensitivity. Using human prostate surface antigen as a model biomarker, we demonstrated that the enzyme-free assay could reach a limit of detection at the femtogram/mL level, which is over 10^3-fold lower than that of conventional enzyme-based assay when the same antibodies and similar procedures were used. The enzyme-free technique we developed can be potentially extended to a variety of other enzymes-based diagnostic technologies beyond ELISA such as immunohistochemistry, Western blot, and point-of-care tests. Importantly, this technique is compatible with equipment and procedures of existing sensing technologies, making it practically useful for clinical diagnostics

In chapter 3, we developed a universal approach for the grafting of BCPs onto hydrophobic inorganic NPs to trigger the assembly of NPs into hollow vesicles. This method relies on the attachment of BCPs onto OA/OAm capped NPs via a one-step ultraviolet-induced thiol–ene reaction, where the double bond in OA (or OAm) and

thiols in BCPs are coupled into thioether linkage through radical addition, followed by the self-assembly of the BCP-tethered NPs into NVs. We demonstrated the assembly of various sized IONPs into magnetic vesicles with potentially enhanced magnetization due to the coupling between adjacent subunits. We also assembled Cu_9S_5, MnO and upconversion NPs into NVs after attachment of amphiphilic BCPs using the same procedures. Accordingly, this study provides a universal strategy for assembling OA or OAm-capped inorganic NPs into hollow NVs which may find a variety of applications in biological fields.

In Chapter 4, we describe the fabrication of nanosized MVs comprising tunable layers of densely packed SPIONs in membranes via cooperative assembly of polymer-tethered SPIONs and free PS-*b*-PAA. The membrane thickness of MVs could be well controlled from 9.8 to 93.2 nm by varying the weight ratio of PS-*b*-PAA to SPIONs. The increase in membrane thickness was accompanied by the enhanced magnetization and transverse relaxivity rate (r_2) in MRI as a result of higher density of SPIONs in the polymeric membrane. Therapeutic agents such as Dox can be efficiently encapsulated in the hollow cavity of MVs and the release of payload can be tuned by varying the membrane thickness of nanovesicles. Upon intravenous injection, Dox-loaded MuMVs conjugated with RGD peptides could be effectively enriched at tumor sites due to synergetic effect of magnetic and active targeting. As a result, they exhibited drastically enhanced signal in MRI, improved tumor delivery efficiency of drugs as well as enhanced antitumor efficacy, compared with groups with only magnetic or active targeting strategy. The unique nanoplatform may find applications in effective disease

control by delivering imaging and therapy to organs/tissues that are not readily accessible by conventional delivery vehicles.

5.2 Future work

Although a variety of NP-based diagnostic and therapeutic agents are in clinical trials and many more are close to the goal, very few of them are hybrid assemblies. It is clear that a myriad of obstacles must be overcome before clinical translation can happen. There exist several barriers for the clinic translation of assembled nanohybrids in cancer theranostics. The relative sophisticated process of fabrication makes it difficult to ensure uniform formulation of nanohybrids from batch to batch in terms of the size, shape, drug loading, and surface of the materials. This can pose a significant obstacle to meet the food and drug administration (FDA) and/or european medicines agency (EMA) regulations to NP-based products. Furthermore, the development and manufacturing cost increases significantly with increasing the level of sophistication of the platform. As for economic consideration, a much lower return on investment becomes a big barrier to technology transfer and commercialization.

As mentioned above, it is crucial to manufacture the hybrid assemblies in a controllable, scalable and economic way with enhanced performance in both imaging and therapy. From the diagnosis point of view, more effort should be made to further increase the sensitivity, reproducibility, and specificity of cancer diagnosis. This stems from current urgent needs for early diagnosis of cancer, better evaluation of the cancer stages, as well as real-time assessment of therapeutic outcome. For example, in our enzyme-free signal amplification project, further optimization of the Pd-Ir NPs@GVs

system could be realized by tuning the size of GV, loading amount of Pd-Ir NPs, particle release time and catalytic efficiency. For the next step, detection of clinical samples are the subjects of our future research. For effective cancer therapy, real time monitoring of the dosage of drugs delivered to target sites at specific times will provide guidance to optimize and tailor the formula for personalized medicine and maximize the therapeutic outcomes, considering the complexity of tumors and difference between individual patients. From this point of view, new imaging methods together with materials design that can enable drug monitoring *in vivo* in a simple and reliable manner are in urgent need. In our magneto-nanovesicles system, isotope labelling of delivery vehicles could be applied to quantify the stability, biodistribution profile, release kinetics and body clearance of the HPINs, which can help us predict treatment outcome for better tailoring the medication for individual patient.

List of my publications

1) Kuikun Yang, Marcus Carter, Qilong Ren, Hongyu Guo, Qian Zhang and Zhihong Nie* A Universal Approach to Assemble Inorganic Nanoparticles into Hollow Vesicles. *In preparation*.

2) Kuikun Yang, Yijing Liu, Qilong Ren, Hongyu Guo, Guangyu Wu, Chenglin Yi, Qian Zhang and Zhihong Nie* Enzyme-induced Aggregation of Gold Nanoparticles for Imaging Guided Combined Photothermal-chemotherapy. *In preparation*.

3) Qilong Ren, Kuikun Yang (equal contribution), Yijing Liu, Marcus Carter, Kyle Thomas Webb and Zhihong Nie* Interfacial Synthesis of Densely Spiky Gold Nanoparticles with Full-spectrum Absorption. *Submitted*.

4) Kuikun Yang, Yijing Liu, Yi Liu, Qian Zhang, Chuncai Kong, Chenglin Yi, Zijian Zhou, Zhantong Wang, Guofeng Zhang, Yang Zhang, Niveen M. Khashab,* Xiaoyuan Chen* and Zhihong Nie* Cooperative Assembly of Magneto-Nanovesicles with Tunable Wall Thickness and Permeability for MRI-Guided Drug Delivery. *J. Am. Chem. Soc* **2018**, 140, 4666.

5) Haihang Ye, Kuikun Yang (equal contribution), Jing Tao, Yijing Liu, Qian Zhang, Sanaz Habibi, Zhihong Nie* and Xiaohu Xia* An Enzyme-Free Signal Amplification Technique for Ultrasensitive Colorimetric Assay of Disease Biomarkers. *ACS Nano* **2017**, 11, 2052.

6) Yijing Liu, Jie He, Kuikun Yang, Chenglin Yi, Yi Liu, Liming Nie, Niveen M. Khashab, Xiaoyuan Chen* and Zhihong Nie* Folding Up of Gold Nanoparticle Strings into Plasmonic Vesicles for Enhanced Photoacoustic Imaging. *Angew. Chem. Int. Ed.* **2015**, 54, 15809.

7) Kuikun Yang, Tingting Gao, Zixian Bao, Jing Su and Xiguang Chen* Preparation and Characterization of a Novel Thermosensitive Nanoparticle for Drug Delivery in Combined Hyperthermia and Chemotherapy. *Journal of Materials Chemistry B* **2013**, 1, 6442.

8) Kuikun Yang, Ming Kong, Yanan Wei, Ya Liu, Xiaojie Cheng, Jing Li, Hyun Jin Park and Xiguang Chen* Folate-modified–chitosan-coated Liposomes for Tumor-targeted Drug delivery. *J Mater Sci* **2013**, 48, 1717.

9) Ya Liu, Ming Kong, Chao Feng, Kuikun Yang, Yang Li, Jing Su, Xiaojie Cheng, Hyun Jin Park* and Xiguang Chen* Biocompatibility, Cellular Uptake and Biodistribution of the Polymeric Amphiphilic Nanoparticles as Oral Drug Carriers. *Colloids and Surfaces B: Biointerfaces* **2013**, 103, 345.

10) Yanan Wei, Qianqian Wang, Tingting Gao, Ming Kong, Kuikun Yang, Yi An, Shaoyan Jiang, Jian Li, Xiaojie Cheng and Xiguang Chen* 3-D Culture of Human Umbilical Vein Endothelial Cells with Reversible Thermosensitive Hydroxybutyl Chitosan Hydrogel. *J Mater Sci: Mater Med* **2013**, 24, 1781.

References

(1) Whitesides, G. M.; Grzybowski, B. *Science* **2002**, *295*, 2418.

(2) Mai, Y.; Eisenberg, A. *Chemical Society Reviews* **2012**, *41*, 5969.

(3) M., A.; S., F. *Advanced Materials* **2003**, *15*, 1323.

(4) Bozzuto, G.; Molinari, A. *International Journal of Nanomedicine* **2015**, *10*, 975.

(5) Hocine, S.; Li, M.-H. *Soft Matter* **2013**, *9*, 5839.

(6) Adam, B.; P., A. S.; J., R. A. *Macromolecular Rapid Communications* **2009**, *30*, 267.

(7) J., S. M.; Ji-Ho, P. *Advanced Materials* **2012**, *24*, 3779.

(8) Albanese, A.; Tang, P. S.; Chan, W. C. W. *Annual Review of Biomedical Engineering* **2012**, *14*, 1.

(9) Hoshyar, N.; Gray, S.; Han, H.; Bao, G. *Nanomedicine* **2016**, *11*, 673.

(10) Blanco, E.; Shen, H.; Ferrari, M. *Nature biotechnology* **2015**, *33*, 941.

(11) Gratton, S. E. A.; Ropp, P. A.; Pohlhaus, P. D.; Luft, J. C.; Madden, V. J.; Napier, M. E.; DeSimone, J. M. *Proceedings of the National Academy of Sciences* **2008**, *105*, 11613.

(12) Jo, D. H.; Kim, J. H.; Lee, T. G.; Kim, J. H. *Nanomedicine: Nanotechnology, Biology and Medicine* **2015**, *11*, 1603.

(13) Petros, R. A.; DeSimone, J. M. *Nature Reviews Drug Discovery* **2010**, *9*, 615.

(14) Kim, B.-S.; Park, S. W.; Hammond, P. T. *ACS Nano* **2008**, *2*, 386.

(15) Yan, Y.; Björnmalm, M.; Caruso, F. *Chemistry of Materials* **2014**, *26*, 452.

(16) Schneider, G. F.; Subr, V.; Ulbrich, K.; Decher, G. *Nano Letters* **2009**, *9*, 636.

(17) Fernandes, N. J.; Koerner, H.; Giannelis, E. P.; Vaia, R. A. *MRS Communications* **2013**, *3*, 13.

(18) Hui, C. M.; Pietrasik, J.; Schmitt, M.; Mahoney, C.; Choi, J.; Bockstaller, M. R.; Matyjaszewski, K. *Chemistry of Materials* **2014**, *26*, 745.

(19) Edmondson, S.; Osborne, V. L.; Huck, W. T. S. *Chemical Society Reviews* **2004**, *33*, 14.

(20) Rao, J. P.; Geckeler, K. E. *Progress in Polymer Science* **2011**, *36*, 887.

(21) Yang, J.; Park, S. B.; Yoon, H.-G.; Huh, Y. M.; Haam, S. *International Journal*

of Pharmaceutics **2006**, *324*, 185.

(22) Jaemoon, Y.; Choong-Hwan, L.; Hyun-Ju, K.; Jin-Suck, S.; Ho-Geun, Y.; Kwangyeol, L.; Yong-Min, H.; Seungjoo, H. *Angewandte Chemie International Edition* **2007**, *46*, 8836.

(23) Kaewsaneha, C.; Tangboriboonrat, P.; Polpanich, D.; Elaissari, A. *ACS Applied Materials & Interfaces* **2015**, *7*, 23373.

(24) Gianella, A.; Jarzyna, P. A.; Mani, V.; Ramachandran, S.; Calcagno, C.; Tang, J.; Kann, B.; Dijk, W. J. R.; Thijssen, V. L.; Griffioen, A. W.; Storm, G.; Fayad, Z. A.; Mulder, W. J. M. *ACS Nano* **2011**, *5*, 4422.

(25) Yang, J.; Lee, C.-H.; Park, J.; Seo, S.; Lim, E.-K.; Song, Y. J.; Suh, J.-S.; Yoon, H.-G.; Huh, Y.-M.; Haam, S. *Journal of Materials Chemistry* **2007**, *17*, 2695.

(26) Solans, C.; Izquierdo, P.; Nolla, J.; Azemar, N.; Garcia-Celma, M. J. *Current Opinion in Colloid & Interface Science* **2005**, *10*, 102.

(27) Ulbrich, K.; Holá, K.; Šubr, V.; Bakandritsos, A.; Tuček, J.; Zbořil, R. *Chemical Reviews* **2016**, *116*, 5338.

(28) Wang, J.; Li, W.; Zhu, J. *Polymer* **2014**, *55*, 1079.

(29) Chen, T.; Yang, M.; Wang, X.; Tan, L. H.; Chen, H. *Journal of the American Chemical Society* **2008**, *130*, 11858.

(30) Weikun, L.; Shanqin, L.; Renhua, D.; Jintao, Z. *Angewandte Chemie International Edition* **2011**, *50*, 5865.

(31) Kang, Y.; Taton, T. A. *Macromolecules* **2005**, *38*, 6115.

(32) Hickey, R. J.; Haynes, A. S.; Kikkawa, J. M.; Park, S.-J. *Journal of the American Chemical Society* **2011**, *133*, 1517.

(33) Mai, Y.; Eisenberg, A. *Accounts of Chemical Research* **2012**, *45*, 1657.

(34) Cui, J.; van Koeverden, M. P.; Müllner, M.; Kempe, K.; Caruso, F. *Advances in colloid and interface science* **2014**, *207*, 14.

(35) Lecommandoux, S.; Sandre, O.; Chécot, F.; Perzynski, R. *Progress in Solid State Chemistry* **2006**, *34*, 171.

(36) Sanson, C.; Diou, O.; Thévenot, J.; Ibarboure, E.; Soum, A.; Brûlet, A.; Miraux, S.; Thiaudière, E.; Tan, S.; Brisson, A.; Dupuis, V.; Sandre, O.; Lecommandoux, S. *ACS Nano* **2011**, *5*, 1122.

(37) Schulz, M.; Olubummo, A.; Binder, W. H. *Soft Matter* **2012**, *8*, 4849.

(38) Krack, M.; Hohenberg, H.; Kornowski, A.; Lindner, P.; Weller, H.; Förster, S. *Journal of the American Chemical Society* **2008**, *130*, 7315.

(39) Hickey, R. J.; Koski, J.; Meng, X.; Riggleman, R. A.; Zhang, P.; Park, S.-J. *ACS Nano* **2014**, *8*, 495.

(40) Yi, C.; Zhang, S.; Webb, K. T.; Nie, Z. *Accounts of Chemical Research* **2017**, *50*, 12.

(41) Bollhorst, T.; Rezwan, K.; Maas, M. *Chemical Society Reviews* **2017**, *46*, 2091.

(42) He, J.; Wang, L.; Wei, Z.; Yang, Y.; Wang, C.; Han, X.; Nie, Z. *ACS Applied Materials & Interfaces* **2013**, *5*, 9746.

(43) Jie, H.; Zengjiang, W.; Lei, W.; Zuleykhan, T.; Taarika, B.; Chaoyang, W.; Xiaojun, H.; T., F. J.; Zhihong, N. *Angewandte Chemie International Edition* **2013**, *52*, 2463.

(44) He, J.; Liu, Y.; Babu, T.; Wei, Z.; Nie, Z. *Journal of the American Chemical Society* **2012**, *134*, 11342.

(45) He, J.; Zhang, P.; Babu, T.; Liu, Y.; Gong, J.; Nie, Z. *Chemical Communications* **2013**, *49*, 576.

(46) Song, J.; Cheng, L.; Liu, A.; Yin, J.; Kuang, M.; Duan, H. *Journal of the American Chemical Society* **2011**, *133*, 10760.

(47) Yijing, L.; Jie, H.; Kuikun, Y.; Chenglin, Y.; Yi, L.; Liming, N.; M., K. N.; Xiaoyuan, C.; Zhihong, N. *Angewandte Chemie International Edition* **2015**, *54*, 15809.

(48) Liu, Y.; Li, Y.; He, J.; Duelge, K. J.; Lu, Z.; Nie, Z. *Journal of the American Chemical Society* **2014**, *136*, 2602.

(49) Lei, W.; Yijing, L.; Jie, H.; J., H. M.; Yunlong, Y.; T., F. J.; Xiaojun, H.; Zhihong, N. *Small* **2015**, *11*, 3762.

(50) Yijing, L.; Xiangyu, Y.; Zhiqi, H.; Peng, H.; Yang, Z.; Lin, D.; Zhantong, W.; Zijian, Z.; Yi, L.; Heather, K.; M., K. N.; Xiaoyuan, C.; Zhihong, N. *Angewandte Chemie* **2016**, *128*, 15523.

(51) Michalet, X.; Pinaud, F. F.; Bentolila, L. A.; Tsay, J. M.; Doose, S.; Li, J. J.; Sundaresan, G.; Wu, A. M.; Gambhir, S. S.; Weiss, S. *Science* **2005**, *307*, 538.

(52) Li, J.; Zhu, J.-J. *Analyst* **2013**, *138*, 2506.

(53) Lu, Z. S.; Li, C. M. *Current Medicinal Chemistry* **2011**, *18*, 3516.

(54) Yong, K.-T.; Law, W.-C.; Hu, R.; Ye, L.; Liu, L.; Swihart, M. T.; Prasad, P. N. *Chemical Society Reviews* **2013**, *42*, 1236.

(55) Gao, X.; Cui, Y.; Levenson, R. M.; Chung, L. W. K.; Nie, S. *Nature Biotechnology* **2004**, *22*, 969.

(56) Zrazhevskiy, P.; Sena, M.; Gao, X. *Chemical Society Reviews* **2010**, *39*, 4326.

(57) Y., Y.; Y., G. M. *Advanced Materials* **2005**, *17*, 2354.

(58) Chen, P.-J.; Hu, S.-H.; Hung, W.-T.; Chen, S.-Y.; Liu, D.-M. *Journal of Materials Chemistry* **2012**, *22*, 9568.

(59) Yang, J.; Dave, S. R.; Gao, X. *Journal of the American Chemical Society* **2008**, *130*, 5286.

(60) Larson, D. R.; Zipfel, W. R.; Williams, R. M.; Clark, S. W.; Bruchez, M. P.; Wise, F. W.; Webb, W. W. *Science* **2003**, *300*, 1434.

(61) Wang, H.; Huff, T. B.; Zweifel, D. A.; He, W.; Low, P. S.; Wei, A.; Cheng, J.-X. *Proceedings of the National Academy of Sciences of the United States of America* **2005**, *102*, 15752.

(62) Durr, N. J.; Larson, T.; Smith, D. K.; Korgel, B. A.; Sokolov, K.; Ben-Yakar, A. *Nano Letters* **2007**, *7*, 941.

(63) Ni, W.; Kou, X.; Yang, Z.; Wang, J. *ACS Nano* **2008**, *2*, 677.

(64) Nah, S.; Li, L.; Fourkas, J. T. *The Journal of Physical Chemistry A* **2009**, *113*, 4416.

(65) Dowling, M. B.; Li, L.; Park, J.; Kumi, G.; Nan, A.; Ghandehari, H.; Fourkas, J. T.; DeShong, P. *Bioconjugate Chemistry* **2010**, *21*, 1968.

(66) He, J.; Huang, X.; Li, Y.-C.; Liu, Y.; Babu, T.; Aronova, M. A.; Wang, S.; Lu, Z.; Chen, X.; Nie, Z. *Journal of the American Chemical Society* **2013**, *135*, 7974.

(67) Chou, L. Y. T.; Zagorovsky, K.; Chan, W. C. W. *Nature Nanotechnology* **2014**, *9*, 148.

(68) Tam, J. M.; Tam, J. O.; Murthy, A.; Ingram, D. R.; Ma, L. L.; Travis, K.; Johnston, K. P.; Sokolov, K. V. *ACS nano* **2010**, *4*, 2178.

(69) Yang, W.; Guo, W.; Le, W.; Lv, G.; Zhang, F.; Shi, L.; Wang, X.; Wang, J.; Wang, S.; Chang, J.; Zhang, B. *ACS Nano* **2016**, *10*, 10245.

(70) Cui, J.; Jiang, R.; Guo, C.; Bai, X.; Xu, S.; Wang, L. *Journal of the American Chemical Society* **2018**, *140*, 5890.

(71) Chen, H.; Song, M.; Tang, J.; Hu, G.; Xu, S.; Guo, Z.; Li, N.; Cui, J.; Zhang, X.; Chen, X.; Wang, L. *ACS Nano* **2016**, *10*, 1355.

(72) Pu, K.; Chattopadhyay, N.; Rao, J. *Journal of Controlled Release* **2016**, *240*, 312.

(73) Xuejiao, S.; Chao, L.; Hua, G.; Qian, C.; Chao, W.; Zhuang, L. *Small* **2015**, *11*, 3932.

(74) C., K. L.; R., B. L.; A., L. N.; J., C. A.; Ying, H.; S., D. E.; L., W. J.; A., D. R. *Small* **2011**, *7*, 169.

(75) Hu, M.; Chen, J.; Li, Z.-Y.; Au, L.; Hartland, G. V.; Li, X.; Marquez, M.; Xia, Y. *Chemical Society Reviews* **2006**, *35*, 1084.

(76) Lin, J.; Wang, S.; Huang, P.; Wang, Z.; Chen, S.; Niu, G.; Li, W.; He, J.; Cui, D.; Lu, G.; Chen, X.; Nie, Z. *ACS Nano* **2013**, *7*, 5320.

(77) Peng, H.; Jing, L.; Wanwan, L.; Pengfei, R.; Zhe, W.; Shouju, W.; Xiaoping, W.; Xiaolian, S.; Maria, A.; Gang, N.; D., L. R.; Zhihong, N.; Xiaoyuan, C. *Angewandte Chemie International Edition* **2013**, *52*, 13958.

(78) Bin, N. H.; Chan, S. I.; Taeghwan, H. *Advanced Materials* **2009**, *21*, 2133.

(79) Sun, C.; Lee, J. S. H.; Zhang, M. *Advanced Drug Delivery Reviews* **2008**, *60*, 1252.

(80) Shubayev, V. I.; Pisanic, T. R.; Jin, S. *Advanced Drug Delivery Reviews* **2009**, *61*, 467.

(81) Adarsh, S.; Hiroshi, H.; Masanori, A. *Nanotechnology* **2010**, *21*, 442001.

(82) Lee, N.; Hyeon, T. *Chemical Society Reviews* **2012**, *41*, 2575.

(83) Hickey, R. J.; Meng, X.; Zhang, P.; Park, S.-J. *ACS Nano* **2013**, *7*, 5824.

(84) Liu, Q.; Song, L.; Chen, S.; Gao, J.; Zhao, P.; Du, J. *Biomaterials* **2017**, *114*, 23.

(85) Song, J.; Huang, P.; Duan, H.; Chen, X. *Accounts of chemical research* **2015**, *48*, 2506.

(86) Song, J.; Pu, L.; Zhou, J.; Duan, B.; Duan, H. *ACS Nano* **2013**, *7*, 9947.

(87) Yu, J.; Chu, X.; Hou, Y. *Chemical Communications* **2014**, *50*, 11614.

(88) Guo, L.; Yan, D. D.; Yang, D.; Li, Y.; Wang, X.; Zalewski, O.; Yan, B.; Lu, W.

ACS Nano **2014**, *8*, 5670.

(89) Rosensweig, R. E. *Journal of Magnetism and Magnetic Materials* **2002**, *252*, 370.

(90) Liu, T.-Y.; Hu, S.-H.; Liu, D.-M.; Chen, S.-Y.; Chen, I. W. *Nano Today* **2009**, *4*, 52.

(91) Khemtong, C.; Kessinger, C. W.; Gao, J. *Chemical Communications* **2009**, 3497.

(92) Laurent, S.; Forge, D.; Port, M.; Roch, A.; Robic, C.; Vander Elst, L.; Muller, R. N. *Chemical Reviews* **2008**, *108*, 2064.

(93) Patil, R. M.; Shete, P. B.; Thorat, N. D.; Otari, S. V.; Barick, K. C.; Prasad, A.; Ningthoujam, R. S.; Tiwale, B. M.; Pawar, S. H. *Journal of Magnetism and Magnetic Materials* **2014**, *355*, 22.

(94) Bae, K. H.; Park, M.; Do, M. J.; Lee, N.; Ryu, J. H.; Kim, G. W.; Kim, C.; Park, T. G.; Hyeon, T. *ACS Nano* **2012**, *6*, 5266.

(95) Hwang, S.; Nam, J.; Jung, S.; Song, J.; Doh, H.; Kim, S. *Nanomedicine* **2014**, *9*, 2003.

(96) Hengte, K.; Jinrui, W.; Zhifei, D.; Yushen, J.; Enze, Q.; Zhanwen, X.; Caixin, G.; Xiuli, Y.; Jibin, L. *Angewandte Chemie International Edition* **2011**, *50*, 3017.

(97) Ke, H.; Wang, J.; Dai, Z.; Jin, Y.; Qu, E.; Xing, Z.; Guo, C.; Liu, J.; Yue, X. *Journal of Materials Chemistry* **2011**, *21*, 5561.

(98) Huang, H.-C.; Barua, S.; Kay, D. B.; Rege, K. *ACS Nano* **2009**, *3*, 2941.

(99) Shutao, W.; Kuan-Ju, C.; Ting-Hsiang, W.; Hao, W.; Wei-Yu, L.; Minori, O.; Pei-Yu, C.; Hsian-Rong, T. *Angewandte Chemie International Edition* **2010**, *49*, 3777.

(100) Hao, W.; Shutao, W.; Helen, S.; Kuan-Ju, C.; Lee, A. A.; Wei-Yu, L.; Yanju, W.; Jing, S.; Ken-ichiro, K.; Johannes, C.; G., R. C.; Hsian-Rong, T. *Angewandte Chemie International Edition* **2009**, *48*, 4344.

(101) Nel, A. E.; Mädler, L.; Velegol, D.; Xia, T.; Hoek, E. M. V.; Somasundaran, P.; Klaessig, F.; Castranova, V.; Thompson, M. *Nature Materials* **2009**, *8*, 543.

(102) Nam, J.; Won, N.; Jin, H.; Chung, H.; Kim, S. *Journal of the American Chemical Society* **2009**, *131*, 13639.

(103) Kumar, A.; Kumar, S.; Rhim, W.-K.; Kim, G.-H.; Nam, J.-M. *Journal of the American Chemical Society* **2014**, *136*, 16317.

(104) Devarakonda, S.; Morgensztern, D.; Govindan, R. *Clinical Lung Cancer* **2013**, *14*, 467.

(105) Govindan, R.; Bogart, J.; Vokes, E. E. *Journal of Thoracic Oncology* **2008**, *3*, 917.

(106) Song, J.; Zhou, J.; Duan, H. *Journal of the American Chemical Society* **2012**, *134*, 13458.

(107) Weiwei, W.; Du, C.; Faming, G.; Xiangmin, M.; Xintao, S. *Advanced Materials* **2012**, *24*, 115.

(108) Zhu, H.; Fang, Y.; Miao, Q.; Qi, X.; Ding, D.; Chen, P.; Pu, K. *ACS Nano* **2017**, *11*, 8998.

(109) Eustis, S.; El-Sayed, M. A. *Chemical Society Reviews* **2006**, *35*, 209.

(110) Lequin, R. M. *Clinical Chemistry* **2005**, *51*, 2415.

(111) Wick, M. R. *Annals of Diagnostic Pathology* **2012**, *16*, 71.

(112) Chao-Min, C.; W., M. A.; Jinlong, G.; R., M. C.; T., P. S.; Emanuel, C.; A., M. K.; M., W. G. *Angewandte Chemie International Edition* **2010**, *49*, 4771.

(113) Chinen, A. B.; Guan, C. M.; Ferrer, J. R.; Barnaby, S. N.; Merkel, T. J.; Mirkin, C. A. *Chemical Reviews* **2015**, *115*, 10530.

(114) Tabakman, S. M.; Lau, L.; Robinson, J. T.; Price, J.; Sherlock, S. P.; Wang, H.; Zhang, B.; Chen, Z.; Tangsombatvisit, S.; Jarrell, J. A.; Utz, P. J.; Dai, H. *Nature Communications* **2011**, *2*, 466.

(115) Soukka, T.; Paukkunen, J.; Härmä, H.; Lönnberg, S.; Lindroos, H.; Lövgren, T. *Clinical Chemistry* **2001**, *47*, 1269.

(116) Kendall, C.; Ionescu-Matiu, I.; Dreesman, G. R. *Journal of Immunological Methods* **1983**, *56*, 329.

(117) Leith, A. G.; Griffiths, G. D.; Green, M. A. *Journal of the Forensic Science Society* **1988**, *28*, 227.

(118) Gao, Z.; Xu, M.; Hou, L.; Chen, G.; Tang, D. *Analytical Chemistry* **2013**, *85*, 6945.

(119) Zhang, Q.; Zhao, B.; Yan, J.; Song, S.; Min, R.; Fan, C. *Analytical Chemistry* **2011**, *83*, 9191.

(120) Ambrosi, A.; Airò, F.; Merkoçi, A. *Analytical Chemistry* **2010**, *82*, 1151.

(121) Lin, H.; Liu, Y.; Huo, J.; Zhang, A.; Pan, Y.; Bai, H.; Jiao, Z.; Fang, T.; Wang, X.; Cai, Y.; Wang, Q.; Zhang, Y.; Qian, X. *Analytical Chemistry* **2013**, *85*, 6228.

(122) Dingbin, L.; Zhantong, W.; Albert, J.; Xinglu, H.; Xiaolian, S.; Fu, W.; Qiang, Y.; Shengxiang, G.; Ningshao, X.; Gang, N.; Gang, L.; R., H. W. A.; Xiaoyuan, C. *Angewandte Chemie International Edition* **2013**, *52*, 14065.

(123) Xia, X.; Zhang, J.; Lu, N.; Kim, M. J.; Ghale, K.; Xu, Y.; McKenzie, E.; Liu, J.; Ye, H. *ACS Nano* **2015**, *9*, 9994.

(124) Yang, T.; Ling, H.; Lamonier, J.-F.; Jaroniec, M.; Huang, J.; Monteiro, M. J.; Liu, J. *Npg Asia Materials* **2016**, *8*, e240.

(125) Liu, J.; Wang, B.; Budi Hartono, S.; Liu, T.; Kantharidis, P.; Middelberg, A. P. J.; Lu, G. Q.; He, L.; Qiao, S. Z. *Biomaterials* **2012**, *33*, 970.

(126) Qian, J.; Zhang, C.; Cao, X.; Liu, S. *Analytical Chemistry* **2010**, *82*, 6422.

(127) Frens, G. *Nature Physical Science* **1973**, *241*, 20.

(128) Qian, X.; Peng, X.-H.; Ansari, D. O.; Yin-Goen, Q.; Chen, G. Z.; Shin, D. M.; Yang, L.; Young, A. N.; Wang, M. D.; Nie, S. *Nature Biotechnology* **2007**, *26*, 83.

(129) Xia, X.; Figueroa-Cosme, L.; Tao, J.; Peng, H.-C.; Niu, G.; Zhu, Y.; Xia, Y. *Journal of the American Chemical Society* **2014**, *136*, 10878.

(130) Gao, L.; Zhuang, J.; Nie, L.; Zhang, J.; Zhang, Y.; Gu, N.; Wang, T.; Feng, J.; Yang, D.; Perrett, S.; Yan, X. *Nature Nanotechnology* **2007**, *2*, 577.

(131) Hynninen, P. H.; Kaartinen, V.; Kolehmainen, E. *Biochimica et Biophysica Acta (BBA) - Bioenergetics* **2010**, *1797*, 531.

(132) Frey, A.; Meckelein, B.; Externest, D.; Schmidt, M. A. *Journal of Immunological Methods* **2000**, *233*, 47.

(133) Anajafi, T.; Mallik, S. *Therapeutic delivery* **2015**, *6*, 521.

(134) Bhatt, N.; Huang, P.-J. J.; Dave, N.; Liu, J. *Langmuir* **2011**, *27*, 6132.

(135) Li, F.; Zhang, H.; Dever, B.; Li, X.-F.; Le, X. C. *Bioconjugate Chemistry* **2013**, *24*, 1790.

(136) Rissin, D. M.; Kan, C. W.; Campbell, T. G.; Howes, S. C.; Fournier, D. R.; Song, L.; Piech, T.; Patel, P. P.; Chang, L.; Rivnak, A. J.; Ferrell, E. P.; Randall, J. D.; Provuncher, G. K.; Walt, D. R.; Duffy, D. C. *Nature Biotechnology* **2010**, *28*, 595.

(137) Laxman, B.; Morris, D. S.; Yu, J.; Siddiqui, J.; Cao, J.; Mehra, R.; Lonigro, R.

J.; Tsodikov, A.; Wei, J. T.; Tomlins, S. A.; Chinnaiyan, A. M. *Cancer research* **2008**, *68*, 645.

(138) de la Rica, R.; Stevens, M. M. *Nature Nanotechnology* **2012**, *7*, 821.

(139) Stefan, L.; Denat, F.; Monchaud, D. *Nucleic Acids Research* **2012**, *40*, 8759.

(140) Armbruster, D. A.; Tillman, M. D.; Hubbs, L. M. *Clinical Chemistry* **1994**, *40*, 1233.

(141) Armbruster, D. A.; Pry, T. *The Clinical Biochemist Reviews* **2008**, *29*, S49.

(142) Shao, P.; Tian, J.; Shi, W.; Yang, Y.; Yang, X.; Gao, S.; Cui, F. *Journal of Materials Chemistry A* **2017**, *5*, 124.

(143) Mahmoud, M. A.; O'Neil, D.; El-Sayed, M. A. *Chemistry of Materials* **2014**, *26*, 44.

(144) Fei-Xiang, M.; Han, H.; Bin, W. H.; Cheng-Yan, X.; Zhichuan, X.; Liang, Z.; Wen, L. X. *Advanced Materials* **2015**, *27*, 4097.

(145) Wen, L. X.; A., A. L.; Zichao, Y. *Advanced Materials* **2008**, *20*, 3987.

(146) Caruso, F.; Caruso, R. A.; Möhwald, H. *Science* **1998**, *282*, 1111.

(147) Kim, S.-W.; Kim, M.; Lee, W. Y.; Hyeon, T. *Journal of the American Chemical Society* **2002**, *124*, 7642.

(148) Zhenzhong, Y.; Zhongwei, N.; Yunfeng, L.; Zhibing, H.; C., H. C. *Angewandte Chemie International Edition* **2003**, *42*, 1943.

(149) Jibin, S.; Binghui, W.; Zijian, Z.; Guizhi, Z.; Yijing, L.; Zhen, Y.; Lisen, L.; Guocan, Y.; Fuwu, Z.; Guofeng, Z.; Hongwei, D.; D., S. G.; Xiaoyuan, C. *Angewandte Chemie International Edition* **2017**, *56*, 8110.

(150) Yang, K.; Liu, Y.; Liu, Y.; Zhang, Q.; Kong, C.; Yi, C.; Zhou, Z.; Wang, Z.; Zhang, G.; Zhang, Y.; Khashab, N. M.; Chen, X.; Nie, Z. *Journal of the American Chemical Society* **2018**, *140*, 4666.

(151) Bin, L.; Xiaoran, D.; Zhongxi, X.; Ziyong, C.; Piaoping, Y.; Jun, L. *Advanced Materials* **2017**, *29*, 1604878.

(152) E., H. C.; N., B. C. *Angewandte Chemie International Edition* **2010**, *49*, 1540.

(153) Park, J.; An, K.; Hwang, Y.; Park, J.-G.; Noh, H.-J.; Kim, J.-Y.; Park, J.-H.; Hwang, N.-M.; Hyeon, T. *Nature Materials* **2004**, *3*, 891.

(154) Tian, Q.; Jiang, F.; Zou, R.; Liu, Q.; Chen, Z.; Zhu, M.; Yang, S.; Wang, J.;

Wang, J.; Hu, J. *ACS Nano* **2011**, *5*, 9761.

(155) Schladt, T. D.; Graf, T.; Tremel, W. *Chemistry of Materials* **2009**, *21*, 3183.

(156) Jing, Z.; Dapeng, S.; Langping, T.; Yanni, W.; Yinghui, C.; Bin, X.; Youlin, Z.; Yulei, C.; Xiaomin, L.; Xianggui, K.; Jan, B. W.; Jan, M. E.; Hong, Z. *Angewandte Chemie International Edition* **2018**, *57*, 3054.

(157) Ye, X.; Zhu, C.; Ercius, P.; Raja, S. N.; He, B.; Jones, M. R.; Hauwiller, M. R.; Liu, Y.; Xu, T.; Alivisatos, A. P. *Nature Communications* **2015**, *6*, 10052.

(158) Kim, Y.-T.; Kim, K.-H.; Kang, E. S.; Jo, G.; Ahn, S. Y.; Park, S. H.; Kim, S. I.; Mun, S.; Baek, K.; Kim, B.; Lee, K.; Yun, W. S.; Kim, Y. H. *Bioconjugate Chemistry* **2016**, *27*, 59.

(159) Liu, B.; Li, Q.; Zhang, B.; Cui, Y.; Chen, H.; Chen, G.; Tang, D. *Nanoscale* **2011**, *3*, 2220.

(160) Durgadas, C. V.; Sharma, C. P.; Sreenivasan, K. *Nanoscale* **2011**, *3*, 4780.

(161) Kim, H.-C.; Kim, E.; Jeong, S. W.; Ha, T.-L.; Park, S.-I.; Lee, S. G.; Lee, S. J.; Lee, S. W. *Nanoscale* **2015**, *7*, 16470.

(162) Cervadoro, A.; Cho, M.; Key, J.; Cooper, C.; Stigliano, C.; Aryal, S.; Brazdeikis, A.; Leary, J. F.; Decuzzi, P. *ACS Applied Materials & Interfaces* **2014**, *6*, 12939.

(163) Liong, M.; Lu, J.; Kovochich, M.; Xia, T.; Ruehm, S. G.; Nel, A. E.; Tamanoi, F.; Zink, J. I. *ACS Nano* **2008**, *2*, 889.

(164) Thomas, C. R.; Ferris, D. P.; Lee, J.-H.; Choi, E.; Cho, M. H.; Kim, E. S.; Stoddart, J. F.; Shin, J.-S.; Cheon, J.; Zink, J. I. *Journal of the American Chemical Society* **2010**, *132*, 10623.

(165) Chao, W.; Xiaoqi, S.; Liang, C.; Shengnan, Y.; Guangbao, Y.; Yonggang, L.; Zhuang, L. *Advanced Materials* **2014**, *26*, 4794.

(166) Xie, J.; Liu, G.; Eden, H. S.; Ai, H.; Chen, X. *Accounts of Chemical Research* **2011**, *44*, 883.

(167) Sharifi, S.; Behzadi, S.; Laurent, S.; Laird Forrest, M.; Stroeve, P.; Mahmoudi, M. *Chemical Society Reviews* **2012**, *41*, 2323.

(168) Latham, A. H.; Williams, M. E. *Accounts of Chemical Research* **2008**, *41*, 411.

(169) Demortière, A.; Panissod, P.; Pichon, B. P.; Pourroy, G.; Guillon, D.; Donnio, B.; Bégin-Colin, S. *Nanoscale* **2011**, *3*, 225.

(170) Qiu, P.; Jensen, C.; Charity, N.; Towner, R.; Mao, C. *Journal of the American Chemical Society* **2010**, *132*, 17724.

(171) Jun, Y.-w.; Seo, J.-w.; Cheon, J. *Accounts of Chemical Research* **2008**, *41*, 179.

(172) Lu, Z.; Yin, Y. *Chemical Society Reviews* **2012**, *41*, 6874.

(173) Ling, D.; Hackett, M. J.; Hyeon, T. *Nano Today* **2014**, *9*, 457.

(174) Liu, Y.; Yang, X.; Huang, Z.; Huang, P.; Zhang, Y.; Deng, L.; Wang, Z.; Zhou, Z.; Liu, Y.; Kalish, H.; Khachab, N. M.; Chen, X.; Nie, Z. *Angewandte Chemie International Edition* **2016**, *55*, 15297.

(175) Allen, T. M.; Cullis, P. R. *Advanced Drug Delivery Reviews* **2013**, *65*, 36.

(176) Al-Jamal, W. T.; Kostarelos, K. *Accounts of Chemical Research* **2011**, *44*, 1094.

(177) Yingchoncharoen, P.; Kalinowski, D. S.; Richardson, D. R. *Pharmacological Reviews* **2016**, *68*, 701.

(178) Marguet, M.; Bonduelle, C.; Lecommandoux, S. *Chemical Society Reviews* **2013**, *42*, 512.

(179) Jen-Hung, F.; Yen-Ho, L.; Tsung-Lang, C.; You-Yin, C.; Shang-Hsiu, H.; San-Yuan, C. *Advanced Healthcare Materials* **2014**, *3*, 1250.

(180) Amstad, E.; Kohlbrecher, J.; Müller, E.; Schweizer, T.; Textor, M.; Reimhult, E. *Nano Letters* **2011**, *11*, 1664.

(181) Geilich, B. M.; Gelfat, I.; Sridhar, S.; van de Ven, A. L.; Webster, T. J. *Biomaterials* **2017**, *119*, 78.

(182) Kania, G.; Kwolek, U.; Nakai, K.; Yusa, S.-i.; Bednar, J.; Wójcik, T.; Chłopicki, S.; Skórka, T.; Szuwarzyński, M.; Szczubiałka, K.; Kepczynski, M.; Nowakowska, M. *Journal of Materials Chemistry B* **2015**, *3*, 5523.

(183) Bixner, O.; Reimhult, E. *Journal of Colloid and Interface Science* **2016**, *466*, 62.

(184) Martínez-González, R.; Estelrich, J.; Busquets, M. *International Journal of Molecular Sciences* **2016**, *17*, 1209.

(185) Bonnaud, C.; Monnier, C. A.; Demurtas, D.; Jud, C.; Vanhecke, D.; Montet, X.; Hovius, R.; Lattuada, M.; Rothen-Rutishauser, B.; Petri-Fink, A. *ACS Nano* **2014**, *8*, 3451.

(186) Geilich, B. M.; van de Ven, A. L.; Singleton, G. L.; Sepúlveda, L. J.; Sridhar,

S.; Webster, T. J. *Nanoscale* **2015**, *7*, 3511.

(187) Mazur, M.; Barras, A.; Kuncser, V.; Galatanu, A.; Zaitzev, V.; Turcheniuk, K. V.; Woisel, P.; Lyskawa, J.; Laure, W.; Siriwardena, A.; Boukherroub, R.; Szunerits, S. *Nanoscale* **2013**, *5*, 2692.

(188) Mosmann, T. *Journal of Immunological Methods* **1983**, *65*, 55.

(189) Qi, H.; Liu, C.; Long, L.; Ren, Y.; Zhang, S.; Chang, X.; Qian, X.; Jia, H.; Zhao, J.; Sun, J.; Hou, X.; Yuan, X.; Kang, C. *ACS Nano* **2016**, *10*, 3323.

(190) Mai, Y.; Eisenberg, A. *Journal of the American Chemical Society* **2010**, *132*, 10078.

(191) Luo, Q.; Hickey, R. J.; Park, S.-J. *ACS Macro Letters* **2013**, *2*, 107.

(192) Sanchez-Gaytan, B. L.; Li, S.; Kamps, A. C.; Hickey, R. J.; Clarke, N.; Fryd, M.; Wayland, B. B.; Park, S.-J. *The Journal of Physical Chemistry C* **2011**, *115*, 7836.

(193) Jianping, G.; Yongxing, H.; Maurizio, B.; P., B. W.; Yadong, Y. *Angewandte Chemie International Edition* **2007**, *46*, 4342.

(194) Arosio, P.; Thévenot, J.; Orlando, T.; Orsini, F.; Corti, M.; Mariani, M.; Bordonali, L.; Innocenti, C.; Sangregorio, C.; Oliveira, H.; Lecommandoux, S.; Lascialfari, A.; Sandre, O. *Journal of Materials Chemistry B* **2013**, *1*, 5317.

(195) Matsumoto, Y.; Jasanoff, A. *Magnetic Resonance Imaging* **2008**, *26*, 994.

(196) Lee, N.; Yoo, D.; Ling, D.; Cho, M. H.; Hyeon, T.; Cheon, J. *Chemical Reviews* **2015**, *115*, 10637.

(197) Wang, C.; Yan, Q.; Liu, H.-B.; Zhou, X.-H.; Xiao, S.-J. *Langmuir* **2011**, *27*, 12058.

(198) Al-Jamal, K. T.; Bai, J.; Wang, J. T.-W.; Protti, A.; Southern, P.; Bogart, L.; Heidari, H.; Li, X.; Cakebread, A.; Asker, D.; Al-Jamal, W. T.; Shah, A.; Bals, S.; Sosabowski, J.; Pankhurst, Q. A. *Nano Letters* **2016**, *16*, 5652.

(199) Tsoi, K. M.; MacParland, S. A.; Ma, X.-Z.; Spetzler, V. N.; Echeverri, J.; Ouyang, B.; Fadel, S. M.; Sykes, E. A.; Goldaracena, N.; Kaths, J. M.; Conneely, J. B.; Alman, B. A.; Selzner, M.; Ostrowski, M. A.; Adeyi, O. A.; Zilman, A.; McGilvray, I. D.; Chan, W. C. W. *Nature Materials* **2016**, *15*, 1212.